Stony Brook University

Intrinsic hydrated defects in $CaCO_3$: a solid state NMR spectroscopic study

A Dissertation Presented

by

Jian Feng

to

The Graduate School

in Partial Fulfillment of the Requirements

for the Degree of

Doctor of Philosopy

in

Chemistry

Stony Brook University

May 2009

Stony Brook University

The Graduate School

Jian Feng

We, the dissertation committee for the above candidate for the **Doctor of Philosophy** degree, hereby recommend acceptance of the dissertation.

Brian L. Phillips – Dissertation Advisor
Professor, Department of Geosciences

Clare P. Grey – Chairperson of Defense
Professor, Department of Chemistry

Roy A. Lacey – Co-advisor and Third Member
Professor, Department of Chemistry

Karl T. Mueller – Outside Member
Professor, Department of Chemistry, Pennsylvania State University

This dissertation is accepted by the Graduate School

Lawrence Martin
Dean of the Graduate School

Abstract of the Dissertation

Intrinsic hydrated defects in $CaCO_3$: a Solid State NMR Spectroscopic Study

by

Jian Feng

Doctor of Philosophy

in

Chemistry

Stony Brook University

2009

Common biogenic materials constructed with calcium carbonate mineral phases and an organic matrix exhibit delicate structure with unusual mechanical properties, and have inspired ideas for the design and synthesis of biomimetic functional materials. The organic templates play an important role in directing assembly of the mineral/organic composites, and in controlling the nucleation and subsequent crystallization. Consequently, knowledge about the molecular interactions at mineral/organic interfaces is essential for understanding the principles of the organic-matrix-mediated biomineralization process. Double resonance NMR techniques based on nuclear spin dipole-dipole interactions can provide local structural information about the mineral/organic interface. NMR studies of natural biogenic materials have relied on the assumption that H occurs principally in the organic matrix. However, even abiogenic

nominally anhydrous calcium carbonate phases can contain significant amounts of H-containing defects, which could interfere with interpretation of spectroscopic results. Therefore, the occurrence of intrinsic hydrated defects in $CaCO_3$ must be considered in studies of biomineralized and biomimetic materials. The purpose of this work is to determine the nature of the H environments in $CaCO_3$ phases.

The research reported in this thesis focuses primarily on synthetic, additive-free calcium carbonate materials, including calcite, aragonite, and an amorphous phase which is now thought to be a common precursor to crystallization in inorganic and biotic systems. The single pulse and double resonance (mostly CP and HETCOR) ^{13}C and ^{1}H NMR spectra were obtained systematically for these phases, giving qualitative information about the H-bearing species involved in the intrinsic defects. These NMR studies provide a baseline for further NMR analysis of biogenic materials or synthesized mineral/organic composites. A correlation based on $^{13}C\{^{1}H\}$ cross-polarization kinetics was also established, from which more quantitative geometrical information can be obtained at low $^{13}C/^{1}H$ abundance. This method was applied to a synthetic calcite/citrate composite, providing evidence for the close association of citrate with carbonate ions in the calcite host.

Table of Contents

Acknowledgement

I would like to extend the utmost gratitude to my advisor, Prof. Brian L. Phillips, for his instruction, thoughtful discussion, patience and generosity. He is such a great scientist, full of inspirations, which helped me out every time I was frustrated in research. I would also like to thank Prof. Phillips for the freedom he gave me to think and explore whatever I am interested in the science field, which makes the research a really pleasant work for me, and is the most important reason that I could enjoy the life in Stony Brook for the past six years. Also, I am grateful to his family, Prof. Katherine Sugg and their children. I will never forget those parties in holidays and special days!

I would also like to thank my committee members, Prof. Clare P. Grey, Roy A. Lacey, and Karl T. Mueller. I must thank Prof. Grey for all her help during my Ph. D study, for her guidance to my academic meetings and for her recommendation when I applied for a postdoctoral position. I also benefited greatly from the joint group meetings she organized. Prof. Lacey and Prof. Mueller are thanked for spending time reading this dissertation and serving on my academic committee.

I am also like to extend my gratitude to my wonderful collaborators. First, I would like to thank Prof. Richard J. Reeder, Dr. Young J. Lee and Dr. Yuanzhi Tang in Reeder's group, for the preparation of calcium carbonate samples. I also need to give my thanks to Dr. F. Marc Michel and Jason MacDonald, for the help and collaboration on the ACC project. Prof. James D. Kubicki at Pennsylvania State University is acknowledged for his computational work on citrate samples. I would also like to thank Prof. John B.

Parise and Wenqian Xu for the structural refinement of $GaAl_{12}$ cluster and quality discussion.

I am also grateful to my group members, Harris Mason, Stacey Cochiara and Wei Li, for their help, support, and sharing experience. Thanks are given to Wei Li for the help and discussion during the collaboration on the project of phosphate adsorption on boehmite. It is our common effort which makes our lab more like a family! Additional thanks are extended to all my friends in Stony Brook.

Finally I thank my parents, Lanhua Xing and Chunxi Feng, for their encouragement, support and being role models in life. Without their endless love, I could never accomplish this degree.

List of Publications

1. Feng J., Tang Y., Lee Y. J., Reeder R. J., Phillips B. L., Amorphous calcium carbonate and hydrated defects in synthetic aragonite detected by solid-state NMR. To be submitted. — Chapter 5

2. Li W., Feng J., Mason H. E., Kediot K., Kubicki J. D., Phillips B. L., Phosphate adsorption on boehmite (gamma-AlOOH): bidentate evidence from NMR. Submitted to Langmuir.

3. Michel F. M., MacDonald J., Feng J., Phillips B. L., Ehm L., Tarabrella C., Parise J. B., Reeder R. J., Structural characteristics of synthetic amorphous calcium carbonate. *Chem. Mater.*, **2008**, *20*, 4720-4728. — Part of Chapter 4

4. Feng J., Lee Y. J., Kubicki J. D., Reeder R. J., Phillips B. L., NMR spectroscopy of citrate in solids: cross-polarization kinetics in weakly coupled systems. *Magn. Reson. Chem.*, **2008**, *46*, 408-417. — Chapter 3

5. Feng J., Lee Y. J., Reeder R. J., Phillips B. L., Observation of bicarbonate in calcite by NMR spectroscopy. *Am. Mineral.*, **2006**, *91*, 957-960. — Chapter 2

6. Phillips B. L., Houston J. R., Feng J., Casey W. H., Observation of solid-state Rh-103 NMR by cross-polarization. *J. Am. Chem. Soc.*, **2006**, *128*, 3912-3913.

Chapter 1

Introduction

1.1 Motivation

Calcium carbonate is of great scientific and technological importance in geosciences, biomineralization and industry. In natural water and ocean systems, calcium carbonate is ubiquitous, forming huge amounts of scale and ocean sediment. As a consequence, the interactions between calcium carbonate minerals and other inorganic ions play an important role in determining the mobility and fate of these species, and in modulating natural water chemistry. Enormous amounts of carbon dioxide are also retained as carbonate ions, and the release and dissolution of CO_2 can affect Earth's atmosphere and climate [1]. For fundamental crystallography, calcium carbonate is used as a model system for investigating the nucleation and crystallization of minerals [2,3], and has been studied for more than a century. Calcium carbonate is also widely used in industry, particularly as a building material in construction and as a filler. Scale formation affects the efficiency of heating and cooling devices, and is one of the basic considerations in engineering design.

Much attention has also been focused on the interactions between calcium carbonate and organic molecules. First of all, organic matter is a common component in natural water systems, and can affect the precipitation and dissolution of calcium carbonate, eventually modulating the water chemistry. Furthermore, crystalline phases of calcium

carbonate, typically calcite and aragonite, are common biogenic minerals formed in the skeletal parts of invertebrate organisms. These mineral/organic composites possess delicate structure with unique properties and exhibit hierarchical order over several length scales [4], which has inspired ideas for the development of materials science and technology. The organic templates play an important role in directing the assembly, and controlling the nucleation and subsequent crystallization, which is thought to eventually determine the morphology of the mineral phase and the property of the mineral/organic composite. Some proposed nucleation mechanisms are illustrated in Fig. 1.1, where clusters could form through different pathways. The oriented nucleation depends on the structural and geometrical match between the organic matrix and crystal faces, as well as on the interactions at the mineral/organic interface. Consequently, knowledge about the nature of interactions at mineral/organic interfaces is fundamental and crucial for understanding the principles of the organic-matrix-mediated biomineralization [4-6].

Characterization of biogenic materials has largely relied on electron microscopy, which provides information about the construct and assembly of the mineral/organic composites, and about the morphology of the mineral formed in organisms. Combined with the knowledge of the biological system, the interactions at mineral/organic interface can be inferred. However, electron microscopy cannot provide direct information at the molecular level about the interface structure, which is needed to understand the biomineralization process and eventually for application of its principles to the design of functional materials. NMR spectroscopy has the advantage of being sensitive to relevant light elements, such as ^{1}H and ^{13}C, and the selective spin manipulation achieved by external oscillating pulses can provide local structural information about the

mineral/organic interface at the molecular level. Therefore, it is potentially a complementary technique to microscopic methods. Some double resonance NMR techniques based on nuclear spin dipole-dipole interactions has been applied to natural biogenic materials [7-9].

These studies have relied primarily on the occurrence of H principally in the organic matrix. However, even abiogenic nominally anhydrous calcium carbonate phases can contain significant amounts of H-containing defects, which could interfere with interpretation of NMR data to obtain structural information about the organic/mineral interface. The hypothesis guiding this thesis is that the intrinsic hydrated defects in $CaCO_3$ must be considered as well. The purpose of this work is to characterize these H environments in $CaCO_3$ phases. The research reported in this thesis is primarily focused on synthetic, additive-free materials of calcium carbonate phases, including calcite, aragonite, and an amorphous phase. For these inorganically prepared samples, we applied solid state NMR spectroscopy to qualitatively study the species and structure of defects associated with H. The obtained ^{13}C and ^{1}H NMR spectra provide a baseline for further NMR spectroscopic analysis of biogenic materials and of synthesized composites assembled by organic templates. We also investigated the cross-polarization (CP) kinetics for weakly heteronuclear dipolar coupled systems, and established a correlation between the CP NMR parameters and the heteronuclear distances of a multi-spin system, which has proven to be useful for obtaining more quantitative geometrical information about multi-spin systems at low concentration.

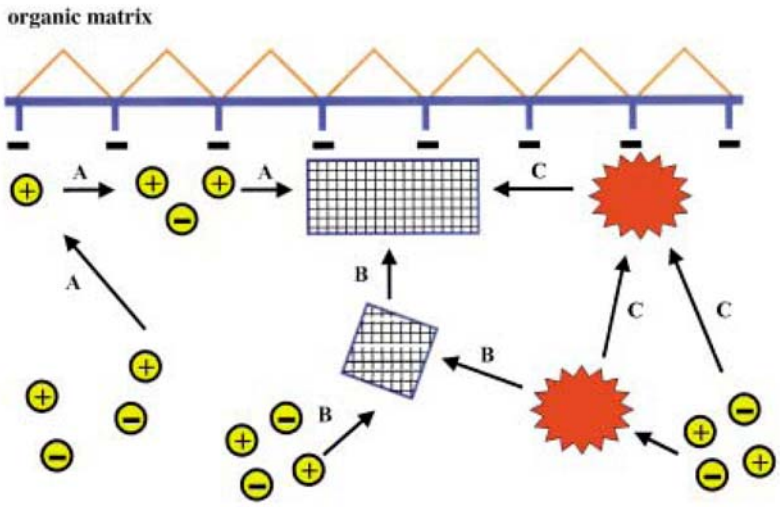

Figure 1.1 Models of organic-matrix-mediated nucleation on biomineralization. Three proposed pathways representing different nucleation mechanisms are illustrated. Pathway *A* indicates that the inorganic ions first bind to the functional groups associated with an organic matrix, then followed by the formation of crystal nuclei. Pathway *B* indicates the cluster could form first in solustion and then bind to the organic matrix. Pathway *C* is through an amorphous phase and the crystallization occurs upon the transformation of the amorphous phase. This figure is from ref. [10]

1.2 Forms of Calcium Carbonate

Calcium carbonate can form naturally or synthetically several crystalline phases, including calcite, aragonite, vaterite, monohydrocalcite and calcium carbonate hexahydrate (the mineral ikaite). Calcite is the thermodynamically stable phase at ambient condition, but the other metastable phases of calcium carbonate can be precipitated from aqueous solution by increasing the rate of precipitation or by adding some additives, such as magnesium ions or sodium polymetaphosphates [11]. For example, a phase diagram [11] for calcium carbonate at 20°C and 1 bar pressure in the presence of Calgon (a glassy form of sodium phosphate) is shown in Fig. 1.2.

Calcite and aragonite are the two typical mineral phases of calcium carbonate formed in organisms, both of which are nominally anhydrous. Calcite has a rhombohedral crystal lattice with the space group of R-3c (illustrated in Fig. 1.3a), and aragonite has an orthorhombic structure with the space group of Pmcn (illustrated in Fig. 1.3b). In the calcite structure, the Ca ions are coordinated by six oxygens from adjacent carbonate groups, and the binding between carbonate and Ca is monodentate. In contrast, the Ca ions in aragonite are coordinated by nine carbonate oxygens, and bidentate coordinations exist between carbonates and Ca ions (shown in Fig. 1.3b). As a result, aragonite is about 9 percent more dense than calcite and is more stable at elevated pressure (above about 2500 atm.).

Amorphous calcium carbonate (ACC) has been recognized as the precursor in the formation of crystalline calcium carbonate phases, and in the bio- or biomimetic mineralization of calcium carbonate. However, little is known about the local structure and long-range order of ACC. Some studies have suggested that different varieties of

ACC with specific short-range order exist, which yield upon crystallization different crystalline phases with specific long-range order [12-14].

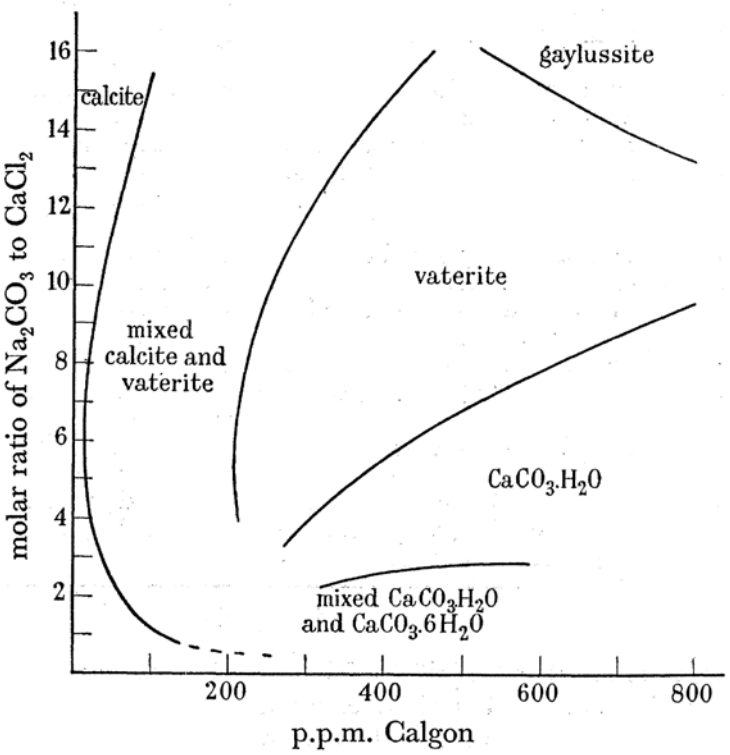

Figure 1.2 Phase diagram for calcium carbonate at 20°C and 1 bar pressure in the presence of Calgon (a form of sodium polymetaphosphate). This figure is from ref. [11].

(a)

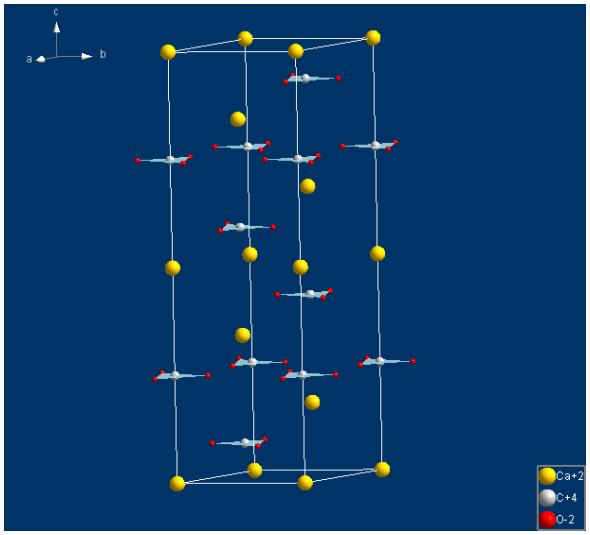

(b)

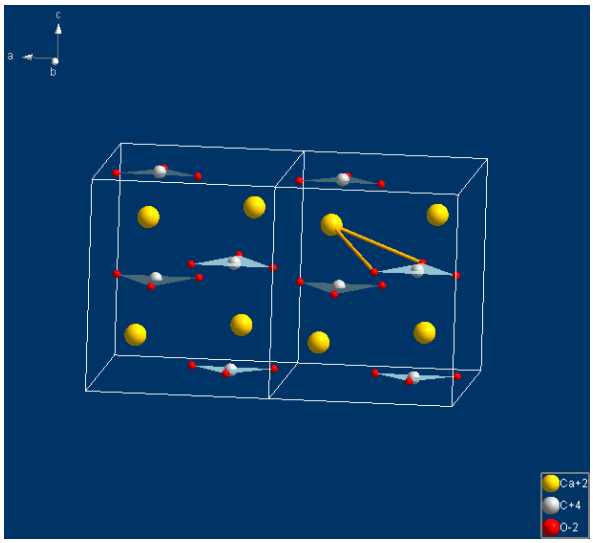

Figure 1.3 Ball-and-Stick models of the crystal structures of calcite (a) and aragonite (b). Yellow balls represent Ca, gray balls represent C and red balls are O. A bidentate coordination between CO_3^{2-} and Ca^{2+} is shown in (b) for aragonite.

1.3 Nuclear Spin Interactions

According to classical electricity and magnetism, charged particles with non-zero angular momentum possess magnetic moments. Therefore, the rotation of protons and electrons can generate magnetic fields, resulting in couplings between these subatomic particles. For example, electrons in atomic orbits with non-vanishing orbital angular momentum yield a huge magnetic moment, which can be observed in atomic beam experiments. On the other hand, electrons and some nuclei also possess magnetic moments in addition to those resulting from orbital motion. Such magnetic moments are intrinsic properties of the basic particles, and called spin magnetic moments. In solid state materials or molecules, the enormous couplings resulting from the orbital magnetic moment quench due to the surrounding coordinated ions or the formation of molecular orbitals [15], so that the much weaker spin interactions are detectable in magnetic resonance experiments. Since all the relevant substances in this thesis are diamagnetic, the description of the spin interactions in subsequent sections focuses on nuclear spins. The couplings between the nucleus and electrons, which dominate the interactions in systems with unpaired electrons, will not be dicussed.

In quantum mechanics, the Hamiltonian of the nuclear spin magnetic interactions can be written in a general form as

$$\mathscr{H}_\lambda = C_\lambda \mathbf{I} \cdot \mathbf{R}_\lambda \cdot \mathbf{A}_\lambda \tag{1.1}$$

where C is a constant, $\mathbf{I}$ and $\mathbf{A}$ are two quantum mechanical operators representing the magnetic quantities involved in the interaction, $\mathbf{R}$ is a second-rank tensor describing the anisotropy and the subscript λ indicates the type of the interaction. The interactions of

interest in this thesis are primarily those between spin I = 1/2 particles (e.g. ^{13}C and ^{1}H), so the quadrupolar interaction will not be described in detail.

1.3.1 Zeeman interaction

The direct magnetic interaction between a nuclear spin and an external static magnetic field is called the nuclear Zeeman interaction. The Hamiltonian of the Zeeman interaction can be expressed as

$$\mathscr{H}_Z = -\gamma \mathbf{I} \cdot \mathbf{B}_0 \tag{1.2}$$

where γ is the magnetogyric ratio, **I** is the spin angular momentum operator and $\mathbf{B}_0$ is the external field vector. The term $\gamma\mathbf{I}$ represents the magnetic moment of a nuclear spin, so the dot product of a spin magnetic moment and the external field results in the magnetic coupling energy. If $\mathbf{B}_0$ is defined as the z-direction of lab frame, the Hamiltonian can be further expressed as

$$\mathscr{H}_Z = -\gamma B_0 \hat{I}_z \tag{1.3}$$

where $\hat{I}_z$ is the z-component of the nuclear spin angular momentum operator.

For a nucleus with spin quantum number l, the projection angular momentum operator $\hat{I}_z$ has $2l+1$ eigenvalues, specified by projection quantum number m = $-l$, $-l+1$, $-l+2$, … , l. For example, there are two eigenstates for $\hat{I}_z$ for a spin-1/2 system, namely $|\alpha\rangle$ (m = 1/2) state and $|\beta\rangle$ state (m = -1/2). Without the external field B_0, these two engenstates are degenerate. However, the energy levels split upon the occurrence of the large external field. The transition energy between $|\alpha\rangle$ and $|\beta\rangle$ is

$$\Delta E = \gamma \hbar B_0 = \hbar \omega_0 \tag{1.4}$$

where $\hbar$ is the Planck constant over 2π (i.e., $\hbar = h/2\pi$) and ω_0 (in angular frequency) is called the Larmor frequency for the nuclear spin. According to the principles of quantum mechanics, electromagnetic radiation with the frequency ω_0 can excite spin transitions between the energy levels with $\Delta \boldsymbol{m} = \pm 1$ (depending on the sign of γ).

At thermal equilibrium, the spin populations in the energy states obey the Boltzmann distribution,

$$\frac{N_{-1/2} - N_{+1/2}}{N_{total}} = \frac{\exp\left(\frac{\hbar\omega_0}{2k_BT}\right) - \exp\left(-\frac{\hbar\omega_0}{2k_BT}\right)}{\exp\left(\frac{\hbar\omega_0}{2k_BT}\right) + \exp\left(-\frac{\hbar\omega_0}{2k_BT}\right)} \tag{1.5}$$

At room temperature, $\hbar\omega_0 / k_BT \sim 0$, the equation can be further approximated as

$$\Delta N = N_{total} \cdot \frac{\hbar\gamma B_0}{2kT} \tag{1.6}$$

as is the so-called "high-temperature" approximation. At thermal equilibrium the population difference for the two quantum states is very small, only around one part per 10^5 under a normal external magnetic field. This contributes to the much weaker sensitivity of NMR compared with most other spectroscopes. The spontaneous magnetization for a spin ensemble observed in a conventional NMR experiment is

$$M = N_{total} \cdot \frac{\hbar^2\gamma^2 B_0}{4kT} \tag{1.7}$$

1.3.2 Oscillating Transverse Magnetic Field

Instead of applying continuous wave radiation (CW) to sweep the absorption of resonant signals, modern NMR spectra are obtained as the Fourier transformation (FT) of the free induction decay (FID) acquired after a short pulse. Due to the weak nature of

magnetic spin interactions, the strength of the applied electromagnetic irradiation can be comparable or even larger than the width of the NMR spectra. Therefore, uniform excitations of nuclear spin resonance signals within the range of spectra can be achieved by a short transverse pulse. The interactions between nuclear spins and the oscillating transverse field are also treated as magnetic couplings.

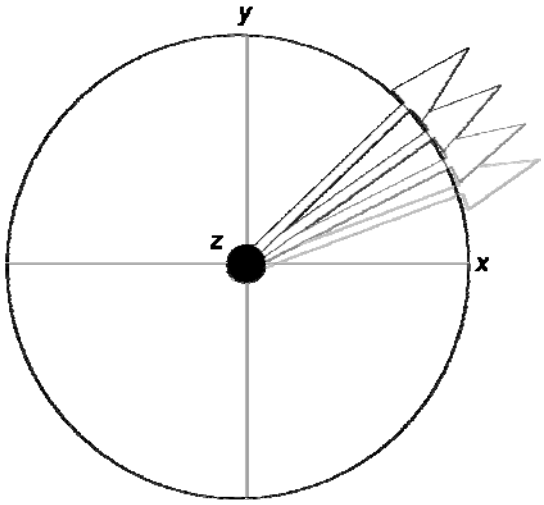

Figure 1.4 An illustration of the transverse magnetic field.

The transverse field (illustrated in Fig. 1.4) is expressed in the lab frame as

$$\mathbf{B}_{rf} = B_{rf}(\cos(\omega_{rf}t+\varphi),\sin(\omega_{rf}t+\varphi),0) \tag{1.8}$$

where B_{rf}, ω_{rf} and φ are the amplitude, frequency and phase of the oscillating r.f. pulse, respectively. The nuclear spin Hamiltonian corresponding to the interaction between spin and this r.f. pulse is written as

$$\begin{aligned}\mathscr{H}_{rf} &= -\gamma \mathbf{I}\cdot\mathbf{B}_{rf} \\ &= -\omega_{nut}\left(\hat{I}_x\cos(\omega_{rf}t+\varphi)+\hat{I}_y\sin(\omega_{rf}t+\varphi)\right)\end{aligned} \tag{1.9}$$

where $\omega_{nut} = \gamma B_{rf}$, is called the nutation frequency. Thus the total external spin Hamiltonian during an r.f. pulse is given by

$$\mathscr{H}_{ext} = -\omega_0 \hat{I}_z - \omega_{nut}\left(\hat{I}_x \cos(\omega_{rf} t + \varphi) + \hat{I}_y \sin(\omega_{rf} t + \varphi)\right) \tag{1.10}$$

Since the excitation pulses and data acquisition in FT/NMR are implemented in a reference frame rotating with frequency ω_{rf}, it is convenient to simplify the Hamiltonian by transforming to the rotating frame:

$$\tilde{\mathscr{H}}_{ext} = (\omega_0 - \omega_{rf})\hat{I}_z + \omega_{nut}\left(\hat{I}_x \cos\varphi + \hat{I}_y \sin\varphi\right) \tag{1.11}$$

where $(\omega_0 - \omega_{rf})$ is called the resonance offset. It should be noted that the time-dependent terms have vanished in the expression with respect to the rotating frame. If ω_{nut} is much larger than $\omega_0 - \omega_{rf}$, the transverse components of spin angular momentum operators $\hat{I}_x$ and $\hat{I}_y$ dominate the Hamiltonian. In this condition, the spontaneous magnetization established along B_0 will rotate around the B_{rf} axis in the rotating frame with the nutation frequency ω_{nut}. The flip angle for the pulse of radiation is defined as

$$\theta_p = \omega_{nut}\tau_p \tag{1.12}$$

where τ_p is the duration of the pulse.

1.3.3 Chemical Shielding Interaction

For diamagnetic materials, the coupling between nuclear spins and the surrounding electron (including both orbital and spin magnetic moments) averages to zero in the absence of an external field B_0. However, the application of B_0 polarizes the electron system and induces a weak electric current in solids or molecules. The nuclei experience an indirect magnetic field due to the effect of external field on electron motion. The

nuclear spin coupling with this indirect local field is called the chemical shielding interaction, and the magnitude is generally of the order of parts per million (ppm) of the Zeeman interaction.

The Hamiltonian of the chemical shielding interaction is expressed as

$$\mathscr{H}_{cs} = \gamma \mathbf{I} \cdot \boldsymbol{\sigma}_{cs} \cdot \mathbf{B} = \gamma \begin{pmatrix} \hat{I}_x & \hat{I}_y & \hat{I}_z \end{pmatrix} \begin{pmatrix} \sigma_{xx} & \sigma_{xy} & \sigma_{xz} \\ \sigma_{yx} & \sigma_{yy} & \sigma_{yz} \\ \sigma_{zx} & \sigma_{zy} & \sigma_{zz} \end{pmatrix} \begin{pmatrix} 0 \\ 0 \\ B_0 \end{pmatrix} \tag{1.13}$$

where $\boldsymbol{\sigma}_{cs}$ is a second-rank tensor, reflecting the anisotropic effect of $\mathbf{B}_0$ upon the induced field. Under a large external field, only the secular part plays a role on spin procession, given as

$$\mathscr{H}_{cs} = \sigma_{zz} \gamma B_0 \hat{I}_z = \sigma_{zz} \omega_0 \hat{I}_z \tag{1.14}$$

The chemical shielding depends on the relative orientation of the molecule or crystallite with respective to the external field. So the static NMR spectra for polycrystalline solids show a broad line shape for nuclei with electronic structure of low symmetry. An example is shown in Fig. 1.5. However, the principal axis frame (PAF) is fixed with respect to the molecular frame. In the PAF, only diagonal components of the tensor have non-zero values and they do not vary with the orientation of the molecule or crystallite. The CS tensor in the lab frame can be obtained by transformation of the tensor from principal frame to lab frame through a set of Euler angles (α, β, γ):

$$\boldsymbol{\sigma}_{cs} = \begin{pmatrix} \sigma_{xx} & \sigma_{xy} & \sigma_{xz} \\ \sigma_{yx} & \sigma_{yy} & \sigma_{yz} \\ \sigma_{zx} & \sigma_{zy} & \sigma_{zz} \end{pmatrix} \xleftarrow[(\alpha,\beta,\gamma)]{Lab \leftarrow PAF} \begin{pmatrix} \sigma_{11} & & \\ & \sigma_{22} & \\ & & \sigma_{33} \end{pmatrix} \tag{1.15}$$

The principal tensor values reflect the symmetry of the local electronic structure, hence the nature of the materials chemical and magnetic structure. For instance, for an atomic

site with axial symmetry, the CS tensor has two equal principal components, i.e. $\sigma_{11} = \sigma_{22}$ or $\sigma_{22} = \sigma_{33}$.

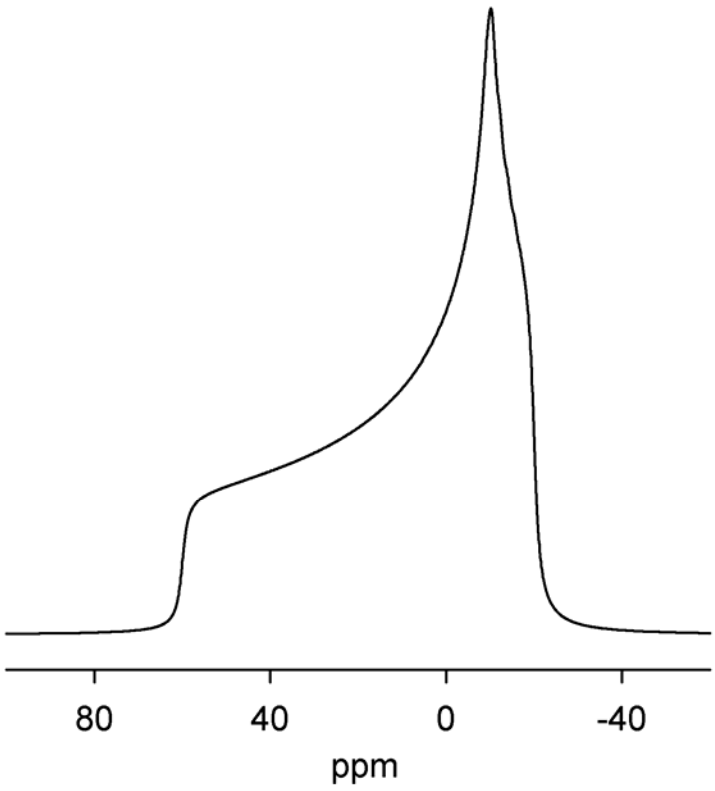

Figure 1.5 ^{13}C static-powder NMR spectrum simulated with SIMPSON program [16]. The broad pattern arises from the ^{13}C chemical shift anisotropy. The parameters used for the simulation are $\delta_{iso} = 10$ ppm, $\delta_{aniso} = 75$ ppm and $\eta = 0.2$, according to the Haeberlen-Mehring-Spiess convention [17,18].

Since we do not measure the Larmor frequency for a bare nucleus, the chemical shielding interaction in practice is measured by comparing with a reference compound. The resulted signal position in NMR spectra is the called chemical shift, defined as

$$\delta_{sample} = \sigma_{ref} - \sigma_{sample} = \frac{\nu_{sample} - \nu_{ref}}{\nu_{ref}} \cdot 10^6 \qquad (1.16)$$

1.3.4 Direct Dipole-Dipole Interaction

Magnetic couplings between nuclear spins can also be observed in NMR spectroscopy. This direct magnetic interaction between nuclear spins is analogous to the interaction between two bar magnets in the macroscopic world.

The dipolar Hamiltonian for a spin pair **I** and **S** is

$$\mathscr{H}_d = \mathbf{I} \cdot \mathbf{D} \cdot \mathbf{S} \tag{1.17}$$

where **D** is an axially symmetric and traceless tensor in Cartesian coordinates, called the dipolar coupling tensor. More directly, the Hamiltonian can be derived using the equation from classical magnetism:

$$\mathscr{H}_d = b_{IS}\left(3(\mathbf{I} \cdot \mathbf{r_{IS}})(\mathbf{S} \cdot \mathbf{r_{IS}}) / r_{IS}^2 - \mathbf{I} \cdot \mathbf{S}\right) \tag{1.18}$$

where $\mathbf{r_{IS}}$ is the internuclear vector of the I-S spin pair and b_{IS} is the dipolar coupling constant, defined in angular frequency as

$$b_{IS} = -\frac{\mu_0}{4\pi}\frac{\gamma_I \gamma_S \hbar}{r_{IS}^3} \tag{1.19}$$

where r_{IS} is I-S spin distance and μ_0 is the vacuum permeability constant. The dipolar coupling is related to the interatomic distance and contains structural information.

The direct dipolar Hamiltonian (1.18) can be further expanded as

$$\mathscr{H}_d = b_{IS}(A + B + C + D + E + F) \tag{1.20}$$

where

$$A = \hat{I}_z \hat{S}_z \left(3\cos^2 \beta - 1\right)$$

$$B = -\frac{1}{4}\left[\hat{I}_+ \hat{S}_- + \hat{I}_- \hat{S}_+\right]\left(3\cos^2 \beta - 1\right)$$

$$C = \frac{3}{2}\left[\hat{I}_z\hat{S}_+ + \hat{I}_+\hat{S}_z\right]\sin\beta\cos\beta e^{-i\alpha}$$

$$D = \frac{3}{2}\left[\hat{I}_z\hat{S}_- + \hat{I}_-\hat{S}_z\right]\sin\beta\cos\beta e^{+i\alpha}$$

$$E = \frac{3}{4}\left[\hat{I}_+\hat{S}_+\right]\sin^2\beta e^{-2i\alpha}$$

$$F = \frac{3}{4}\left[\hat{I}_-\hat{S}_-\right]\sin^2\beta e^{+2i\alpha}$$

where α and β are Euler angles. The raising (+) and lowering (–) operators are defined as

$$\hat{I}_\pm = \hat{I}_x \pm i\hat{I}_y \quad and \quad \hat{S}_\pm = \hat{S}_x \pm i\hat{S}_y \tag{1.21}$$

The secular approximations are different for heteronuclear and homonuclear spin systems. For heteronuclear dipolar coupling, only the term A commutes with the Zeeman interaction. For a homonuclear spin system, however, the Zeeman eigenstates $|\alpha\beta\rangle$ and $|\beta\alpha\rangle$ are degenerate. So the term B, whose matrix representation in Zeeman eigenbasis is block diagonal, is also a secular term. The off-diagonal components join the degenerate states $|\alpha\beta\rangle$ and $|\beta\alpha\rangle$, resulting in the energy conservative spin flip-flop process. This is the physical basis for homonuclear spin diffusion.

The nuclear spin dipolar coupling is dependent on the relative orientation of an internuclear vector with respect to the external field. The powder pattern for a hetero- or homo-nuclear spin pair is called a Pake doublet, as illustrated in Fig. 1.6.

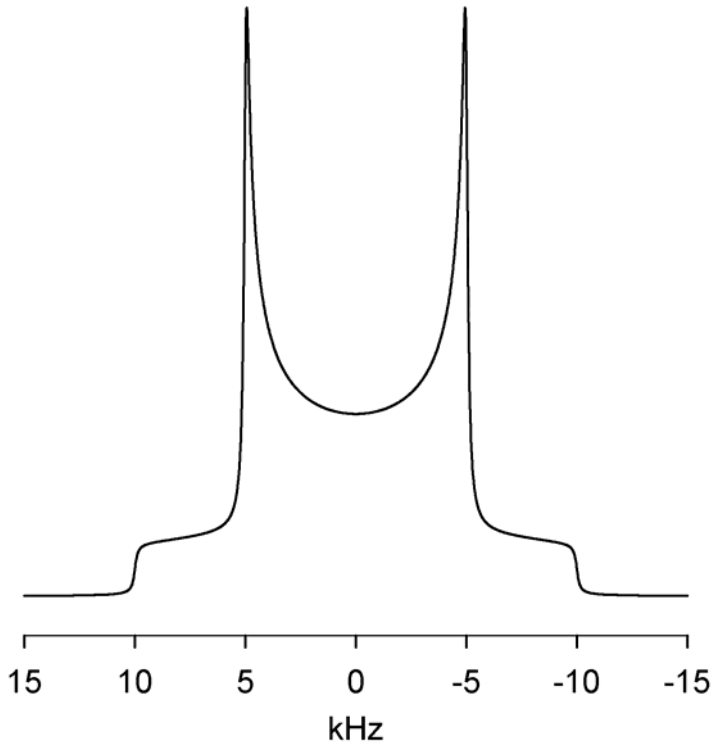

Figure 1.6 ^{13}C static-powder NMR spectrum simulated with SIMPSON program [16]. The Pake doublet pattern arises from the orientation dependence of ^{13}C-^{1}H dipolar coupling interactions (b_{IS} = 10 kHz for this simulation).

1.4 NMR Techniques for Solids

Modern NMR spectroscopy is more than a spectroscopic technique which measures the absorption of photons in the radio frequency (RF) range. With the manipulation of spins by strong transverse pulses, as stated in section 1.2, the nuclear spin interactions can be selectively removed or recovered in an NMR experiment. A large variety of NMR sequences has been developed for different purposes useful in structural or dynamical studies. In the following sections, some routine NMR techniques or methods relevant to the contents in this thesis will be introduced.

1.4.1 Magic Angle Spinning (MAS)

The Hamiltonians for nuclear spin interactions, including chemical shielding, dipolar coupling and quadruapolar interactions are anisotropic, i.e., these magnetic couplings depend on the relative orientation of the molecule or crystallite with respect to the external field B_0. In solution NMR, the anisotropies are averaged to zero by fast and random molecular tumbling. For solid materials, however, these orientation dependences remain in the Hamiltonian, generally leading to a broad pattern for powder samples in static NMR experiments. In the late 1950s, Andrew et al. [19] and Lowe [20] independently realized that if the sample rotates around an axis, which is tilted at the so-called 'magic angle' (54.74°) with respect to B_0, some anisotropic nuclear spin interactions can be removed.

Mechanical rotation introduces an arbitrary periodic time-dependency to the Hamiltonian, with frequency of the spinning rate. For the chemical shielding interaction, heteronuclear dipolar coupling and 1st order quadrupolar coupling, those time-dependent

terms can be averaged out by the sample spinning. The time-independent terms for these interactions all contain a factor of $(3\cos^2\theta_{axis}-1)$. When the rotating axis is aligned at 54.74° with respect to B_0, $(3\cos^2\theta_{axis}-1)$ is equal to zero. So the anisotropies of these nuclear spin interactions vanish upon sample spinning around the magic angle. When the spinning rate is much larger than the size of the anisotropic interactions, only the isotropic resonance remains in the NMR spectra. At lower spinning rate, a series of spinning side bands separated by the spinning frequency occur.

For homonuclear dipolar coupling, the Hamiltonian does not commute during spinning due to the presence of the flip-flop term (i.e., term *B* in eqn. (1.20)). So the anisotropy resulting from homonuclear dipolar coupling can not be efficiently removed by MAS. Particularly when homonuclear spins are abundant in the structure and form a dipolar-coupled network, the sample needs to be spun much faster than the value of homonuclear dipolar coupling frequency to obtain a narrow line width.

A special case is the homonuclear spin pair. For systems approximating an isolated spin pair, the homonuclear dipolar coupling can be averaged out by MAS if the spinning speed is higher than the CSA. However, if the difference in isotropic chemical shift for the two spins is equal to a multiple of the spinning rate, an anisotropic homonuclear dipolar coupling term remains in the Hamiltonian, which is the so-called rotational resonance.

To conclude, magic angle spinning is one of the most important NMR techniques for improvement of spectral resolution for solids. Since its discovery in the late 1950's, NMR became a more powerful tool for characterization in the field of solid state materials, especially with the development of technology that allows high stable spinning rates.

MAS has been a routine technique for solid state NMR experiments, and most of the NMR pulse sequences are designed to be utilized in combination with magic angle sample spinning.

1.4.2 Cross Polarization (CP)

In a strong external magnetic field, the very different energy splitting of hetero-nuclear spin species caused by the Zeeman interaction prevents mutual spin flips from occurring. However, Hartmann and Hahn [21] demonstrated in 1962 that, in the rotating frame, the transition energy for heteronuclear spins can be equalized by applying r.f. irradiation with different magnitudes. Under the Hartmann-Hahn condition $\omega_{1I} = \omega_{1S}$, where $\omega_{1I} = \gamma_I B_{1I}$ and $\omega_{1S} = \gamma_S B_{1S}$, a flip-flop term remains in the Hamiltonian and heteronuclear spins can exchange energy through the dipolar coupling. NMR techniques based on this principle are called cross polarization (CP).

CP has been developed as a routine solid state NMR technique for improving the sensitivity of nuclear spins with dipolar contact to nuclei with higher magnetogyric ratio. Since the spontaneous magnetization of a spin ensemble is proportional to the NMR active spin density N_{total} and the square of magnetogyric ratio γ^2, as shown in eqn. (1.7), a rare spin system (S) with low γ has a much smaller magnetization than spin (I) with larger γ. In general, CP can enhance the NMR sensitivity for spin S system by a factor of the order γ_I/γ_S, compared with single pulse excitation. In addition, the rare spin system usually has a long spin lattice relaxation time (T_1) due to the lack of homonuclear dipolar coupling. The indirect excitation through CP can reduce the delay time between experimental acquisitions to the order of the relaxation time of the abundant spin system,

which can be several orders of magnitude shorter than that of rare spin system. So the NMR sensitivity can be improved by more acquisitions per length of time.

CP kinetics describes the variation of CP intensity with contact time. In principle, the CP kinetics depends on the strength of the heteronuclear dipolar coupling interactions. Larger dipolar coupling leads to faster CP intensity build-up. So geometrical and structural information can be obtained from study of the CP kinetics. Quantitatively, the mathematical equations describing CP kinetics depend on the detailed configurations of the spin system. In the following sections, a brief introduction to CP kinetics for some typical models will be given.

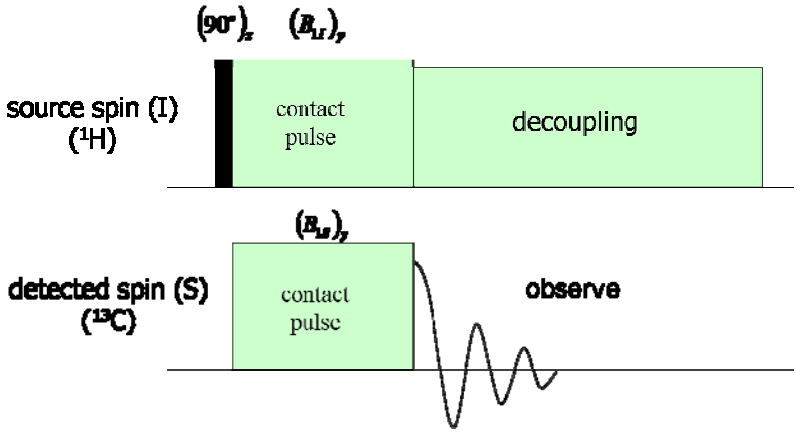

Figure 1.7 Pulse sequence of cross-polarization.

1.4.2.1 Classical Thermodynamic Model

The classical model refers to a multiple spin system with weak heteronuclear dipolar coupling interactions. During the CP process, systems *I* (abundant) and *S* (rare) have

uniform spin temperatures respectively. For the abundant spin *I*, the homonuclear dipolar coupling should be much larger than the I–S heteronuclear dipolar coupling, so that the spin diffusion is fast enough to hold a uniform spin temperature. Under such conditions, each spin system can be treated as a thermodynamic reservoir, with spin energy exchange between *I* and *S* through dipolar coupling. When the spin *I* is excited (i.e. 90° pulse in Fig. 1.7) and then spin-locked by the transverse field $(B_{1I})_y$, the *I* spin system is cooled down in the sense that a small field B_{1I} holds a large magnetization, while the spin temperature for *S* spin system is infinitely high in the rotating frame. The system tends to reach thermal equilibrium, so the spin temperature varies according to the differential equation:

$$\begin{aligned} \frac{d\beta_S}{dt} &= -\frac{\beta_S - \beta_I}{T_{IS}} - \frac{\beta_S}{T_{1\rho}^S} \\ \frac{d\beta_I}{dt} &= -\varepsilon\alpha^2 \cdot \frac{\beta_I - \beta_S}{T_{IS}} - \frac{\beta_I}{T_{1\rho}^I} \end{aligned} \tag{1.22}$$

where β_I and β_I are spin temperatures for *I* and *S* respectively, T_{IS} is the cross polarization time constant, $T_{1\rho}$ is the spin lattice relaxation time in the rotating frame, $\varepsilon = N_S / N_I$, and $\alpha = \gamma_S B_{1S} / \gamma_I B_{1I}$.

Under the conditions of $\varepsilon \approx 0$ and $T_{1\rho}^S >> T_{IS}$, an approximate solution can be expressed in the form of a biexponential equation

$$\begin{aligned} M_S^{CP}(\tau_{CP}) &= M_S^0 \cdot \frac{\gamma_I}{\gamma_S} \cdot \left(1 - \frac{T_{IS}}{T_{1\rho}^I}\right)^{-1} \cdot \left[\exp\left(-\frac{\tau_{CP}}{T_{1\rho}^I}\right) - \exp\left(-\frac{\tau_{CP}}{T_{IS}}\right)\right] \\ &= I_{0,CP} \cdot \left(1 - \frac{T_{IS}}{T_{1\rho}^I}\right)^{-1} \cdot \left[\exp\left(-\frac{\tau_{CP}}{T_{1\rho}^I}\right) - \exp\left(-\frac{\tau_{CP}}{T_{IS}}\right)\right] \end{aligned} \tag{1.23}$$

Demco et al. [22] derived a quantitative equation for T_{IS},

$$T_{IS}^{-1} = A \cdot M_2^{IS} \cdot C_x\left(\omega_{1I}, \omega_{1S}, \tau_c\right) \tag{1.24}$$

where A is a constant related to experimental settings, such as ω_{1I}, ω_{1S} and the resonance offsets, and τ_c is the homonuclear correlation time, related to the homonuclear dipolar interactions. M_2^{IS} is the van Vleck second moment of the heteronuclear dipolar coupling which is related to the *I*-*S* distances (r_i) and expressed as:

$$M_2^{IS} = \frac{4}{15}\gamma_I^{\,2}\gamma_S^{\,2}\left[\frac{\mu_0}{4\pi}\right]^2\left[\frac{\hbar}{2\pi}\right]^2 I_I(I_I+1)\sum_i r_i^{-6} \tag{1.25}$$

where I_I refers to the spin quantum number for spin I, and the r_i is the internuclear distance between S and the i^{th} I spin nearby.

Qualitatively, the effect of homonuclear dipolar coupling on T_{IS} depends on the I-S distance. Thus the I spins in the 1st dipolar contact shell to spin S primarily determine the effective homonuclear second moment, or τ_c.

1.4.2.2 CP Kinetics for Spin Pair

If the strength of heteronuclear dipolar coupling is comparable or even larger than that of the homonuclear spins, the classical model is no longer applicable for describing the cross polarization kinetics. For such cases, the assumption of uniform spin temperature for each spin reservoir is not realistic. In contrast to the thermodynamic model, these systems are generally referred to as I-I*-S models, where I* indicates those I spins strongly coupled to S. The I*-S part, or in other words the SI_n spin cluster, is more or less isolated, and the polarization transfer between I* and S are calculated analytically. Other I spins are generally treated as a thermodynamic reservoir and communicate with I* through spin diffusion.

A special case is the single isolated S-I spin pair model, i.e. n = 1, for which the CP kinetics can be derived unambiguously. For a static single crystal sample, Muller et al. [23] gave the equation for CP kinetics as

$$M(\tau_{CP}) = M_0 \left\{ 1 - \frac{1}{2}\exp(-k_1\tau_{CP})\cos\left[\frac{1}{4}D\left(1-3\cos^2\theta\right)\tau_{CP}\right] - \frac{1}{2}\exp\left(-k_2\tau_{CP}\right)\right\} \quad (1.26)$$

where k_1 and k_2 are the 1st order rate constants which characterize the decay of the transient oscillation and the long term build-up of the magnetization, D is the dipolar coupling constant and θ is the polar angle of the I–S vector with respective to B_0. Hediger [24] further derived the equation for a static powder and included the relaxation parameters ($T_{1\rho}$) for I:

$$M(\tau_{CP}) = M_0 \left\{ \begin{array}{l} \frac{1}{2}\left[\exp\left(-\frac{\tau_{CP}}{T_{1\rho}} \right) - \exp(-k_1\tau_{CP}) g_0(\tau_{CP}) \right] \\ + \left[\frac{\langle S_z \rangle_{qe}}{\omega_{0I}} - 0.5 \right] \left[\exp\left(-\frac{\tau_{CP}}{T_{1\rho}} \right) - \exp\left(-k_2\tau_{CP}\right) \right] \end{array} \right\} \quad (1.27)$$

where $g_0\left(\tau_{CP}\right)$ is a function representing the average of the dipolar coupling for a powder sample and the dipolar coupling constant D is contained in this function. $\langle S_z \rangle_{qe}$ is the equilibrium magnetization at long contact time. When combined with magic angle spinning, similar kinetics equations can be obtained in the high spinning speed limit (i.e. $\nu_R >> D$) for each side band match conditions. For MAS experiment, the $g_0(\tau_{CP})$ needs to be replaced by $g_f(\tau_{CP})$, where subscript f denotes the side band number in the CP match profile [24].

In summary, the study of CP kinetics for an isolated I-S spin pair can be an effective method for measuring the heteronuclear interatomic distance, whether the NMR experimental setup is for single crystal, static powder or MAS.

1.4.2.3 Two-stage Curve

Another typical CP kinetics curve which can often be observed in NMR experiments is the two-stage curve [25-28]. It also falls in the regime of I-I*-S models. When the oscillation damps rapidly, e.g. the k_1 in eqn. (1.26) and (1.27) is large, the CP curve will be characterized by a fast initial increase followed by a much slower polarization build-up. For such cases, the CP kinetics equation can be approximated as [28]

$$M(\tau_{CP}) = M_0 \cdot \exp\left(-\frac{\tau_{CP}}{T_{1\rho}}\right)\left\{\begin{array}{l}\left[1-\lambda\exp\left(-\frac{\tau_{CP}}{T_{df}}\right)\right] \\ -(1-\lambda)\exp\left(-\frac{3}{2}\cdot\frac{\tau_{CP}}{T_{df}}\right)\exp\left(-\frac{1}{2}\cdot\frac{\tau_{CP}^2}{T_2^2}\right)\end{array}\right\} \qquad (1.28)$$

where T_{df} is the time constant for I-I* spin diffusion, and for spin pair case, $T_{df}^{-1} = k_2 = \frac{2}{3}k_1$ [24,29]. T_2 can be viewed as root-mean-square weighted average of dipolar coupling for a powder sample, and λ is defined as $1/(n+1)$.

This equation contains a Gaussian decay term, corresponding to the rapid initial CP intensity build-up.

1.4.3 Heteronuclear Correlation (HETCOR)

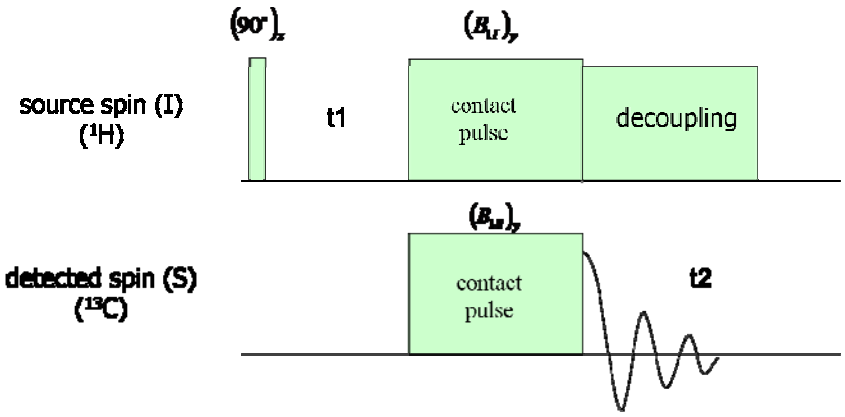

Figure 1.8 Pulse sequence of HETCOR.

Wideline Separation (WISE) [30,31] Heteronuclear Correlation (HETCOR) can be obtained by slight modification of the CP sequence, adding an incremental t1 delay after the ^{1}H 90° excitation pulse, shown in Fig. 1.8. During the t1 delay, the ^{1}H coherence undergoes free evolution in the transverse plane, and the subsequent spin-locking sequence (namely, contact pulse) transfers the ^{1}H polarization to the associated ^{13}C spins, resulting in a 2-dimentional (2-D) NMR spectroscopy. The 2-D spectrum obtained in this way by Fourier Transform (FT) of the t1 and t2 dimensions can separate the ^{1}H spectrum according to the ^{13}C signals, establishing a correlation between heteronuclear coupled ^{13}C and ^{1}H spins. As a result, the ^{1}H spectrum correlated to a ^{13}C resonance in a 2-D HETCOR spectrum only gives rise to signals from those ^{1}H spins which are in proximity to the corresponding ^{13}C spin.

1.5 References

1. Zeebe RE, Zachos JC, Caldeira K, Tyrrell T, *Science*, 2008, **321**: 51-52.
2. DeYoreo JJ, Vekilov PG, *Rev. Mineral. Geochem.*, Dove PM, DeYoreo JJ, Weiner S (Eds.), 2003, **54**: 57-93. Mineralogical Society of America: Washington, DC.
3. Niederberger M, Cölfen H, *Phys. Chem. Chem. Phys.*, 2006, **8**: 3271-3287.
4. Mann S. *Biomineralization: principles and concepts in bioinorganic materials chemistry*. Oxford University Press: New York, 2001, xii, 198 p.
5. Weiner S, Traub W, *Philos. Trans. R. Soc. London, Ser. B*, 1984, **304**: 425-&.
6. Lowenstam HA, Weiner S. *On biomineralization*. Oxford University Press: New York, 1989, ix, 324 p.
7. Takahashi K, Yamamoto H, Onoda A, Doi M, Inaba T, Chiba M, Kobayashi A, Taguchi T, Okamura T, Ueyama N, *Chem. Commun.*, 2004: 996-997.
8. Nassif N, Pinna N, Gehrke N, Antonietti M, Jäger C, Cölfen H, *Proc. Natl. Acad. Sci. U.S.A.*, 2005, **102**: 12653-12655.
9. Jäger C, Cölfen H, *Crystengcomm*, 2007, **9**: 1237-1244.
10. Cölfen H, Mann S, *Angew. Chem. Int. Ed.*, 2003, **42**: 2350-2365.
11. Brooks R, Clark LM, Thurston EF, *Philos. Trans. R. Soc. London, Ser. A*, 1950, **243**: 145-167.
12. Hasse B, Ehrenberg H, Marxen JC, Becker W, Epple M, *Chemistry-a European Journal*, 2000, **6**: 3679-3685.
13. Politi Y, Levi-Kalisman Y, Raz S, Wilt F, Addadi L, Weiner S, Sagi I, *Adv. Funct. Mater.*, 2006, **16**: 1289-1298.

14. Lam RSK, Charnock JM, Lennie A, Meldrum FC, *Crystengcomm*, 2007, **9**: 1226-1236.

15. Slichter CP. *Principles of magnetic resonance*. Springer-Verlag: Berlin, New York, 1989.

16. Bak M, Rasmussen JT, Nielsen NC, *J. Magn. Reson.*, 2000, **147**: 296-330.

17. Haeberlen U, *Adv. Magn. Reson.*, Waugh JS (Ed.), 1976, **Suppl. 1**. Academic Press: New York.

18. Mehring M. *Principles of high-resolution NMR in solids*. Springer-Verlag: Berlin, New York, 1983.

19. Andrew ER, Bradbury A, Eades RG, *Nature*, 1958, **182**: 1659.

20. Lowe IJ, *Phys. Rev. Lett.*, 1959, **2**: 285.

21. Hartmann S, Hahn EL, *Phys. Rev.*, 1962, **128**: 2042-&.

22. Demco DE, Tegenfeldt J, Waugh JS, *Phys. Rev. B*, 1975, **11**: 4133-4151.

23. Muller L, Kumar A, Baumann T, Ernst RR, *Phys. Rev. Lett.*, 1974, **32**: 1402-1406.

24. Hediger S. *Improvement of heteronuclear polarization transfer in solid-state NMR*, Ph.D. dissertation, 1997. Eidgenössische Technische Hochschule, Zürich.

25. Alemany LB, Grant DM, Alger TD, Pugmire RJ, *J. Am. Chem. Soc.*, 1983, **105**: 6697-6704.

26. Wu XL, Zhang SM, Wu XW, *Phys. Rev. B*, 1988, **37**: 9827-9829.

27. Wu XL, Zilm KW, *J. Magn. Reson.*, 1991, **93**: 265-278.

28. Kolodziejski W, Klinowski J, *Chem. Rev.*, 2002, **102**: 613-628.

29. Fyfe CA, Lewis AR, Chezeau JM, *Can. J. Chem.*, 1999, 77: 1984-1993.

30. Vega AJ, J. Am. Chem. Soc., 1988, 110: 1049-1054.

31. Schmidt-Rohr K, Clauss J, Spiess HW, Macromolecules, 1992, 25: 3273-3277.

Chapter 2

Observation of bicarbonate in calcite by NMR spectroscopy

Abstract

We show that the signal observed in $^{13}C\{^{1}H\}$ cross-polarization magic-angle-spinning (CP/MAS) NMR spectra of synthetic calcite precipitated at room temperature arises from bicarbonate ion. Although this peak occurs at the same chemical shift as for the bulk carbonate signal, its observation by CP/MAS indicates that it corresponds to carbonate associated with H. The variation in the CP/MAS intensity with contact time shows oscillations characteristic of C-H pairs separated by 1.9(1) Å and remote from other H, consistent with bicarbonate. $^{13}C\{^{1}H\}$ heteronuclear correlation spectra indicate that the hydrogen in the bicarbonate groups gives a relatively narrow ^{1}H NMR signal at +7.4 ppm. A peak at this chemical shift is also observed in direct-observe ^{1}H MAS NMR spectra of the synthetic sample, and also in natural biogenic and abiogenic calcite. This ^{1}H chemical shift indicates a moderate hydrogen bonding interaction $d(OH\ldots O) \approx 1.85$ Å, which suggests significant structural relaxation occurs near the bicarbonate.

2.1 Introduction

Interaction with organic matter has a large influence on the precipitation and growth of calcite as both biomineral and in abiogenic settings. As a result, naturally occurring calcite from many low-temperature environments contains some organic material considered to be "intracrystalline" in the sense that the organic molecules are inaccessible to fluids, but are released upon digestion of the mineral [1-5]. Most studies of this intracrystalline organic matter have relied on extraction and concentration methods for subsequent analysis. Study by in situ spectroscopic [3] and microchemical [6,7] methods is needed to understand the structural relationship between occluded organic molecules and the calcite host.

NMR spectroscopy is a potentially useful tool for study of natural and synthetic calcite/organic composites because of its sensitivity to the relevant light elements (^{13}C, ^{1}H, and ^{15}N), and its ability to establish spatial proximities via through-space dipole-dipole interactions. Several studies have reported ^{13}C NMR data for synthetic calcite/organic composites, using $^{13}C\{^{1}H\}$ cross-polarization magic-angle-spinning (CP/MAS) methods. In all cases, these spectra contain peaks from carbonate groups in addition to those from the organic molecules [8-10]. Signal observed by $^{13}C\{^{1}H\}$ CP/MAS arises only from carbon atoms within a few Å of rigid ^{1}H nuclei. Bulk carbonate groups more distant from ^{1}H are invisible to this technique, making it possible to use CP/MAS NMR to detect carbonate groups located near intracrystalline organic molecules [7]. We have found that $^{13}C\{^{1}H\}$ CP/MAS NMR spectra of inorganically precipitated calcite samples formed in low-temperature settings, both natural and synthetic, contain a peak at the position for carbonate carbon, even for samples in which

the organic content is low. Here we report NMR spectroscopic data for one such sample, prepared with ^{13}C-enriched carbonate, that show bicarbonate to be the source of the CP/MAS signal. These bicarbonate ions yield a distinctive signal in ^{1}H MAS NMR spectra that is also observed in natural calcite. These results indicate that bicarbonate ion is a significant source of CP/MAS signal in biogenic and other natural calcites.

2.2 Experimental

2.2.1 Sample Materials

A synthetic ^{13}C-enriched calcite sample was prepared by the seeded constant addition method, as described in detail by Phillips et al. [8]. Briefly, about 0.7 g of ^{13}C-enriched overgrowth was precipitated on 0.5 g of 5 μm calcite seeds (natural ^{13}C abundance) in a 0.7 L suspension, by addition of 0.1 *M* $CaCl_2$ and $Na_2{}^{13}CO_3$ solutions at 150 μL min^{-1}. The crystals are rhombohedral and give XRD patterns consistent with calcite as the only phase present. A portion of a calcite speleothem (ER67a) (calcite formed naturally in caves) from the Grotta di Ernesto (Italy) was crushed to -120 mesh and treated in commercial sodium hypochlorite solution for nine days and rinsed. Reagent grade sodium bicarbonate (Alfa Aesar) and a natural trona specimen (trisodium hydrogen dicarbonate dehydrate, $Na_3H(CO_3)_2{\cdot}2H_2O$) from the Westvaco mine, Sweetwater Co., Wyoming (Wards) were also examined.

2.2.2 NMR Spectroscopy

Solid-state NMR spectra were obtained on a 400 MHz (9.4 T) Varian Inova spectrometer operating at 100.6 MHz for ^{13}C and 399.76 MHz for ^{1}H. The $^{13}C\{^{1}H\}$ CP/MAS spectra were obtained with a Varian T3 probe assembly configured for 7.5 mm (o.d.) rotors. The ^{1}H MAS NMR spectra were obtained at a spinning rate of 15 kHz with a Chemagnetics probe assembly fitted for 4 mm rotors and modified to yield low ^{1}H background. The $^{13}C\{^{1}H\}$ cross-polarization dynamics were measured at a spinning rate of 3.0 kHz at the $n = 1$ sideband match condition, with the carbonate center band on-resonance and no modulation of the B_1 fields during the contact period. The sample was restricted to the central 1/2 of the rotor volume to maximize B_1 homogeneity. The ^{13}C chemical shift anisotropies (CSA) were determined from analysis of spinning sideband intensities obtained at a spinning rate of 1.0 kHz using the WSOLIDS program [11]. We measured 2-dimensional $^{13}C\{^{1}H\}$ heteronuclear correlation (HetCor) spectra at a spinning rate of 5 kHz and a contact time (τ_c) of 4 ms using a linear ramp of the ^{13}C B_1 field (11 kHz total width) to flatten the match condition. No homonuclear ^{1}H decoupling was applied during $t1$. Several spectra were measured, varying the $F1$ spectral width from 20 to 80 kHz. Chemical shifts are reported relative to tetramethylsilane (TMS) using secondary standards of adamantane for ^{13}C (δ = 38.6 ppm for CH_2) and hydroxylapatite for ^{1}H (δ = 0.2 ppm).

2.3 Results and discussion

2.3.1 $^{13}C\{^{1}H\}$ CP/MAS spectra and ^{13}C single-pulse MAS spectra

The $^{13}C\{^{1}H\}$ CP/MAS spectra of the synthetic calcite (Fig. 2.1a) contain a single resonance at a chemical shift, $\delta_{C\text{-}13}$ = 168.7 ppm, that is the same within experimental uncertainty (<0.1 ppm) as that for the bulk mineral obtained by single-pulse excitation (Fig. 2.1b). However, the peaks observed by CP/MAS are significantly broader, 1.2 ppm (FWHM) at τ_{CP} = 1 ms, compared to a width near instrumental resolution (<0.1 ppm FWHM) for the single-pulse spectrum. This result indicates that the average chemical shift for carbonate groups near rigid H-bearing species (observed by CP/MAS) does not differ significantly from that for carbonate groups in well-ordered regions of calcite structure.

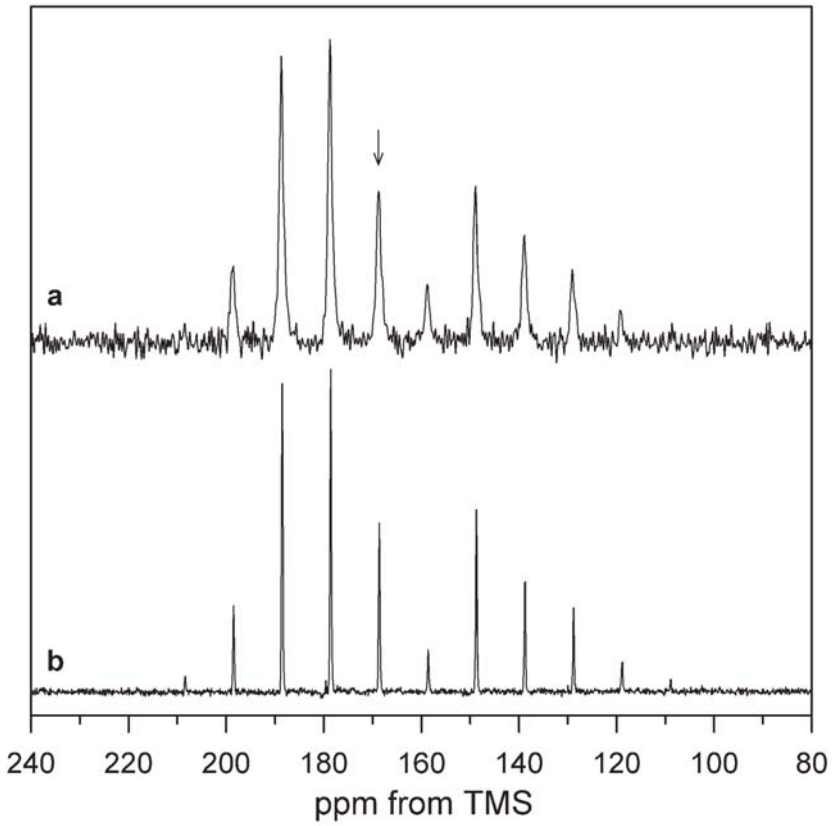

Figure 2.1 ^{13}C MAS NMR spectra of synthetic ^{13}C-enriched calcite at 1.0 kHz spinning rate. (**a**) CP/MAS, 1 ms contact time, 130,000 acquisitions at 1s relaxation delay. (**b**) Single-pulse acquisition, 4 acquisitions at 3600 s relaxation delay. Arrow denotes center band position; remaining peaks are spinning sidebands.

2.3.2 $^{13}C\{^1H\}$ CP kinetics curve

The variation of $^{13}C\{^1H\}$ CP/MAS intensity with τ_c (Fig. 2.2) shows an initial increase of intensity up to about τ_c = 0.7 ms, followed by a series of oscillations that are characteristic of isolated ^{13}C-^1H spin pairs [12,13]. The oscillation frequency of the CP dynamics is related to the ^{13}C-^1H dipolar coupling frequency, which varies with the ^{13}C-^1H internuclear distance as $(r_{C\text{-}H})^{-3}$. Using a form given by Hediger [12] and Fyfe et al. [13], good fits of the CP dynamics curve can be obtained with $r_{C\text{-}H}$ = 1.9 ± 0.1 Å (Fig. 2.2), similar to the C-H distance determined by XRD methods for bicarbonate ion in nahcolite [14]. The observed data cannot be modeled perfectly with any single C-H distance, which suggests a small distribution in the structure or a contribution from an adjacent (e.g., H-bonded) carbonate. The data at short τ_c are fit best with $r_{C\text{-}H}$ = 1.87 Å, whereas 2.05 Å fits best at long τ_c. To produce C-H distances near 1.9 Å with other possible species such as hydroxyl or water would require a very strong hydrogen bond to the carbonate group, $r_{(H\ldots O)} < 1.3$ Å, but ^1H chemical shift data presented below indicate a moderate hydrogen bond interaction for the associated H. On this basis we assign the signal observed by $^{13}C\{^1H\}$ CP/MAS to bicarbonate ions and adjacent carbonate.

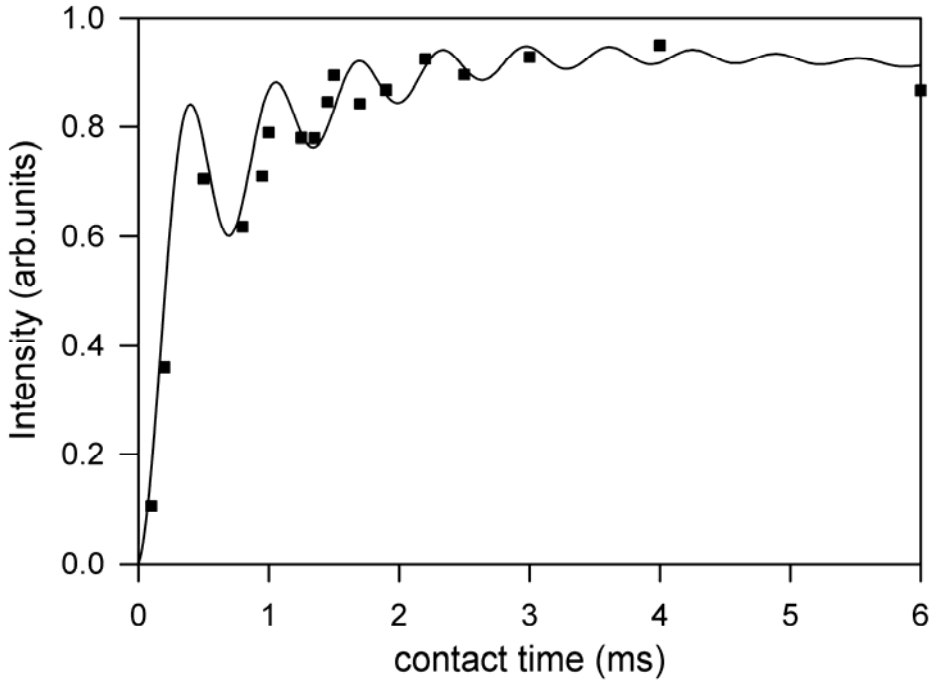

Figure 2.2 $^{13}C\{^{1}H\}$ CP/MAS kinetics for synthetic ^{13}C-enriched calcite. Points are observed data, line is a scaled theoretical curve assuming isolated ^{13}C-^{1}H spin pairs separated by 1.9 Å. Data acquired at a spinning rate of 3.0 kHz for 40,000 acquisitions at each contact time, using a 1s relaxation delay.

2.3.3 ^{13}C Chemical shift anisotropy (CSA)

The ^{13}C chemical shift anisotropy (CSA) provides additional evidence for assignment of the $^{13}C\{^{1}H\}$ CP/MAS peak to bicarbonate ion. For calcite, axial site symmetry at the C-position constrains two of the principal CSA tensor components to be equal. Allowing all the parameters to vary, a fit of the single pulse spinning sideband (SSB) intensities gives a CSA that is axially symmetric within uncertainty: δ_{11} = 194.7, δ_{22} = 192.8, δ_{33} = 118.6 ppm. These values are in excellent agreement with previous measurements for calcite using single crystal [15] and static powder [16] methods. Fits to the CP/MAS intensities obtained at τ_c = 0.3 ms yield a CSA that differs significantly from axial symmetry: δ_{11} = 203, δ_{22} = 184, and δ_{33} = 119 ppm. Similar values were obtained at τ_c = 1 ms, but were consistent with the presence of a contribution from carbonate groups. By symmetry, the δ_{33} direction lies approximately normal to the carbonate plane, so that the splitting of the values for δ_{11} and δ_{22} is consistent with a change in the shielding in the direction of one of the O atoms due to protonation.

2.3.4 $^{13}C\{^{1}H\}$ HetCor spectra

The $^{13}C\{^{1}H\}$ HetCor spectrum (Fig. 2.3) shows that H in the bicarbonate groups gives a narrow ^{1}H MAS-NMR peak at $\delta_{H\text{-}1}$ = 7.4 ppm. This experiment observes the ^{13}C CP/MAS spectrum (*F*2 dimension), but with an incremented delay (*t*1) between 1H excitation and the contact period to produce a second frequency dimension (*F*1) that contains an indirectly detected ^{1}H NMR spectrum [17,18]. The signal in this ^{1}H dimension is due to those ^{1}H from which magnetization was transferred to ^{13}C during τ_c, and corresponds to the hydrogen physically located near carbon atoms. The *F*1 cross-sections taken at the carbonate peak position in *F*2 show only a single ^{1}H NMR signal, which must correspond to the H of the bicarbonate groups. No signal was detected that could be attributed to other H-bearing species, such as water molecules or hydroxyl groups [19], even though we looked carefully for a broad component in the *t*1 time domain at wide *F*1 spectral windows. This result indicates that the distance to other rigid hydrogen must be too large for significant ^{1}H-^{1}H spin exchange over the 4 ms contact period.

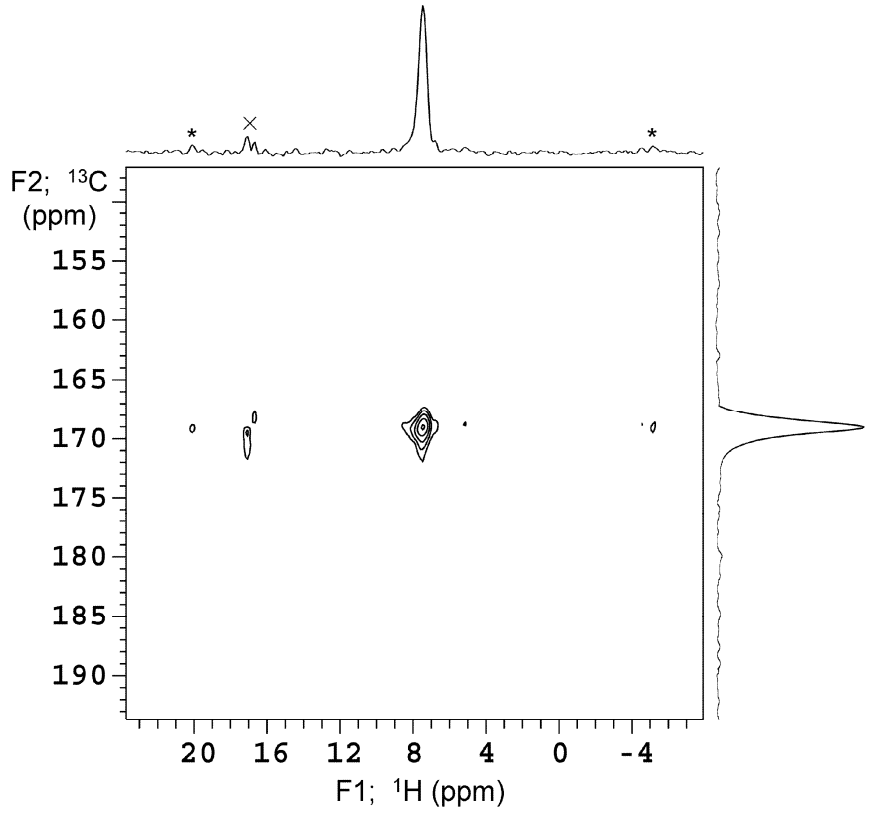

Figure 2.3 $^{13}C\{^{1}H\}$ HetCor NMR spectra of synthetic ^{13}C-enriched calcite. Contours are at 6.5, 12.7, 24.7, 48.2, and 93.9% intensity. Spectra at top and right are skyline projections. Data acquired with a contact time of 4 ms with 48 hypercomplex points in *t*1 at an increment of 50 μs. * denotes spinning sidebands; **x** is an instrumental artifact.

2.3.5 ^{1}H MAS spectra for synthetic and natural calcite

By comparison with the HetCor data, a small peak that occurs at 7.4 ppm in single-pulse ^{1}H MAS NMR spectra of the synthetic calcite can be assigned to bicarbonate ion (Fig. 2.4b). These data show that bicarbonate represents only a small fraction of the H present in this sample, less than ca. 1%. The peaks at 4.8 - 6 ppm are likely due to water molecules, and those near 1.2 ppm to hydroxyl groups [19]. Based on previous measurement for total H content of this sample (ca. 70 μmol H/g; Phillips et al. [8]), we estimate the bicarbonate content to be approximately 70 (±20) ppm for this sample, which is relatively low compared to natural calcite (e.g., Bischoff et al. [20]). A weak, but distinct peak at +7.4 ppm also occurs in spectra of natural calcite samples, such as that for a calcite speleothem shown in Figures 4c and 4d and which also gives a carbonate CP/MAS signal. Spectra obtained by Gaffey [19] for echinoid calcite (i.e., calcite formed in organisms which are classified as Echinoidea) also show a shoulder at $\delta_{H\text{-}1}$ = 7.4 ppm. For calcite/citrate co-precipitates, the peak at 7.4 ppm appears much more prominent in ^{1}H MAS and ^{13}C{^{1}H} HetCor spectra [8], which suggests that bicarbonate substitution can serve as a local charge balance mechanism near large defects or mosaic boundaries [21].

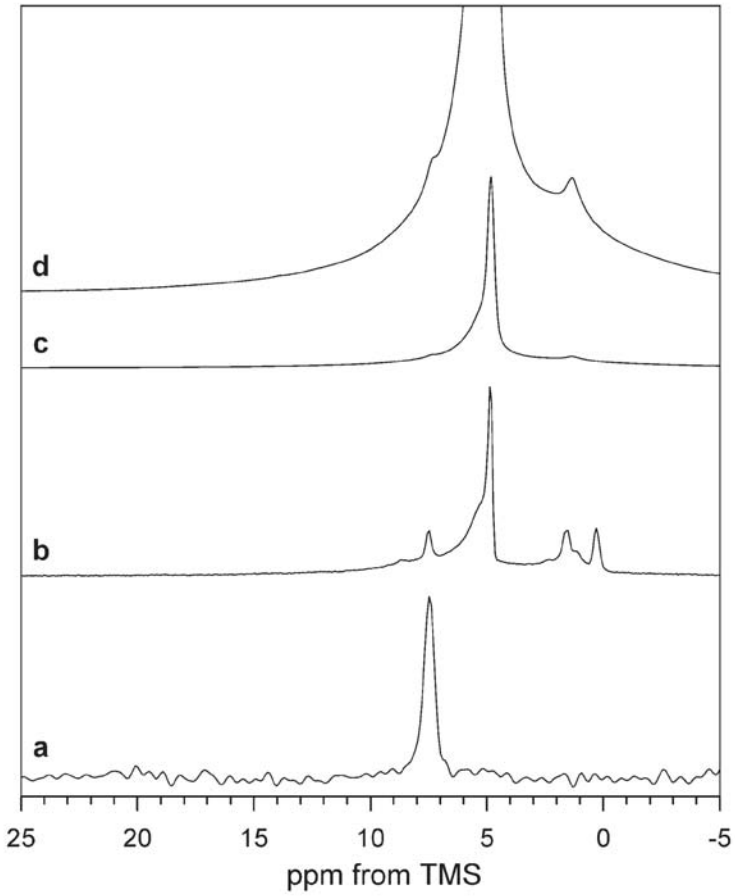

Figure 2.4 ^{1}H NMR spectra of synthetic ^{13}C-enriched calcite (**a**.**b**) and a natural speleothem calcite (**c**.**d**). (**a**) Indirectly detected spectrum from the 2-d HetCor data shown in Figure 2.3, obtained as a summed projection across the width of the carbonate peak in *F*2. (**b**) Direct observe ^{1}H MAS NMR spectrum obtained at a 15 kHz spinning rate. (**c**) Speleothem Er67a, single-pulse excitation at 15 kHz spinning rate. (**d**) Same as in **c**, but at 10× vertical scaling.

2.3.6 H-bonding and structural indications

Previous studies have found good correlations between the ^{1}H NMR chemical shift and the strength of hydrogen bonding, from which some information on the local structure of the bicarbonate can be obtained. From the observed $\delta_{H\text{-}1}$ = 7.4 ppm, the expression by Brunner and Sternberg [22] gives a moderate H-bond length of $r_{(H\ldots O)}$ = 1.85 Å, whereas the correlation given by Yesinowski et al. [23] gives $r_{(O\ldots O)}$ = 2.81 Å. These values are nearly identical if one assumes $r_{(O\text{-}H)}$ = 0.97 Å and linear geometry. For comparison, we measured ^{1}H chemical shifts for bicarbonate ions in nahcolite ($NaHCO_3$; $\delta_{H\text{-}1}$ = 14.1 ppm) and trona ($Na_3H(CO_3)_2(H_2O)_2$; $\delta_{H\text{-}1}$ = 18.6 ppm), for which the correlation by Yesinowski et al. [23] yields O…O distances of 2.55 and 2.37 Å, respectively. These values agree reasonably well with those from diffraction data: 2.61 Å for nahcolite [14] and 2.46 Å for trona [24], although the systematic differences suggest that the correlation might differ for carbonate groups. However, simply extrapolating the data for nahcolite and trona to 7.4 ppm gives $r_{(O\ldots O)}$ = 2.83 Å for bicarbonate in calcite, in good agreement with the correlations of Yesinowski et al. [23] and Brunner and Sternberg [22].

For a hydrogen-bond length of $r_{(H\ldots O)}$ = 1.85 Å and $r_{(O\text{-}H)}$ = 0.97 Å, the maximum possible O-O distance, 2.82 Å, results from a linear geometry (Fig. 2.5). This maximum O-O distance is significantly shorter than that between O atoms in adjacent carbonate groups in the calcite structure, the smallest of which is 3.187 Å [25]. This observation suggests that significant structural relaxation occurs around the bicarbonate substitution.

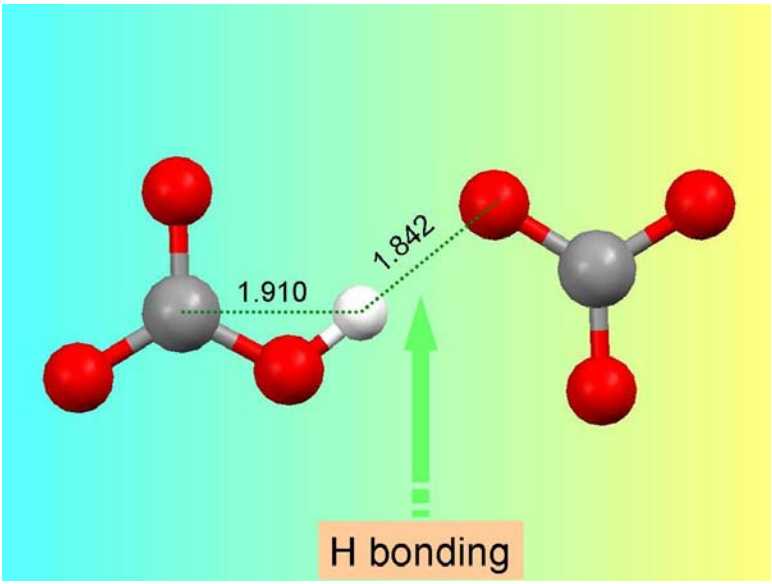

Figure 2.5 Inferred H bonding structure for bicarbonate defects in calcite. Red balls represent O, gray balls represent C and white balls represent H.

2.4 Conclusion

The present results indicate that bicarbonate defects in calcite can contribute significantly to $^{13}C\{^{1}H\}$ CP/MAS NMR spectra and are indistinguishable from the calcite carbonate groups by ^{13}C chemical shift. These observations are relevant to studies of natural and synthetic organic/calcite composites, because the carbonate chemical shift overlaps the chemical shift range for carboxyl carbons and the associated ^{1}H NMR peak lies in the range often attributed to amide groups. Furthermore, the rapid build-up of CP/MAS intensity, due to the relatively short C-H distance, can interfere with contact-time spectral editing methods for organic components in biominerals (e.g., Nassif et al. [26]). Considering the likely role of bicarbonate and other hydrated species for local charge-balance and structural accommodation in organic/calcite composites, observation of a carbonate signal by CP/MAS NMR is itself insufficient to establish spatial proximity to organic H [7], although HetCor data could provide this information.

2.5 References

1. Berman A, Addadi L, Kvick A, Leiserowitz L, Nelson M, Weiner S, *Science*, 1990, **250**: 664-667.
2. Neuweiler F, Rutsch M, Geipel G, Reimer A, Heise KH, *Geology*, 2000, **28**: 851-854.
3. Ramseyer K, Miano TM, D'Orazio V, Wildberger A, Wagner T, Geister J, *Org. Geochem.*, 1997, **26**: 361-378.
4. Sykes GA, Collins, M. J., Walton, D. I., *Org. Geochem.*, 1995, **23**: 1059-1065.
5. Walton D, *Org. Geochem.*, 1998, **28**: 389-410.
6. Dauphin Y, Cuif JP, Salome C, Susini J, *Am. Mineral.*, 2005, **90**: 1748-1758.
7. Takahashi K, Yamamoto H, Onoda A, Doi M, Inaba T, Chiba M, Kobayashi A, Taguchi T, Okamura T, Ueyama N, *Chem. Commun.*, 2004: 996-997.
8. Phillips BL, Lee YJ, Reeder RJ, *Environ. Sci. Technol.*, 2005, **39**: 4533-4539.
9. Takahashi K, Doi M, Kobayashi A, Taguchi T, Onoda A, Okamura TA, Yamamoto H, Ueyama N, *Chem. Lett.*, 2004, **33**: 192-193.
10. Ueyama N, Hosoi T, Yamada Y, Doi M, Okamura T, Nakamura A, *Macromolecules*, 1998, **31**: 7119-7126.
11. Eichele K, Wasylishen RE. *HBA*, Version: 1.5. Dalhousie University and Universität Tübingen, 2006.
12. Hediger S. *Improvement of heteronuclear polarization transfer in solid-state NMR*, Ph.D. dissertation, 1997. Eidgenössische Technische Hochschule, Zürich.
13. Fyfe CA, Lewis AR, Chezeau JM, *Can. J. Chem.*, 1999, **77**: 1984-1993.
14. Sharma BD, *Acta Crystallogr.*, 1965, **18**: 818-&.

15. Lauterbur PC, *Phys. Rev. Lett.*, 1958, **1**: 343-344.

16. Pines A, Rhim WK, Waugh JS, *J. Chem. Phys.*, 1971, **54**: 5438-&.

17. Zumbulyadis N, *Phys. Rev. B*, 1986, **33**: 6495-6496.

18. Schmidtrohr K, Clauss J, Spiess HW, *Macromolecules*, 1992, **25**: 3273-3277.

19. Gaffey SJ, *Am. Mineral.*, 1995, **80**: 947-959.

20. Bischoff WD, Sharma SK, Mackenzie FT, *Am. Mineral.*, 1985, **70**: 581-589.

21. Duffy DM, Travaille AM, van Kempen H, Harding JH, *J. Phys. Chem. B*, 2005, **109**: 5713-5718.

22. Brunner E, Sternberg U, *Prog. Nucl. Magn. Reson. Spectrosc.*, 1998, **32**: 21-57.

23. Yesinowski JP, Eckert H, Rossman GR, *J. Am. Chem. Soc.*, 1988, **110**: 1367-1375.

24. Choi CS, Mighell AD, *Acta Crystallogr., Sect. B-Struct. Sci.*, 1982, **38**: 2874-2876.

25. Markgraf SA, Halliyal A, Bhalla AS, Newnham RE, Prewitt CT, *Ferroelectrics*, 1985, **62**: 17-26.

26. Nassif N, Pinna N, Gehrke N, Antonietti M, Jäger C, Cölfen H, *Proc. Natl. Acad. Sci. U.S.A.*, 2005, **102**: 12653-12655.

Chapter 3

NMR spectroscopy of citrate in solids: cross-polarization kinetics in weakly coupled systems

Abstract

Solid-state NMR spectroscopy is a potentially powerful method for obtaining molecular level structural information crucial for understanding the specific relationship between calcite crystals and occluded organic molecules that are important in biomineralization and biomimetic materials. In this work, a method is developed based on cross-polarization/magic angle spinning (CP/MAS) NMR to measure the heteronuclear distances and obtain structural information for large intracrystalline citrate defects in a synthetic calcite/citrate composite. Using compounds with well-characterized crystal structures, Mg(II) citrate and Sr(II) citrate, a correlation is established between T_{IS}, the CP time, and M_2^{IS}, the van Vleck heteronuclear dipolar second moment, which contains distance and structural information. This correlation is supported by peak assignments obtained from calculations of the ^{13}C chemical shifts for crystalline Mg(II) citrate. On the basis of T_{IS}^{-1} *versus* M_2^{IS} correlation, measurement of T_{IS} for carbonate ions associated with citrate defects in a calcite(^{13}C-enriched)/citrate coprecipitate yields

an estimate for the distance between citrate and the nearest carbonate carbon that indicates close spatial proximity and provides useful constraints for future computational studies. The applicability of T_{IS}^{-1} *versus* M_2^{IS} correlations to other weakly coupled spin-1/2 systems is discussed in terms of the effects of ^1H homonuclear dipolar coupling, using the CP kinetics of Zn(II) dihydroxybenzoate and kaolinite for comparison. The results suggest a limited range of correlation constants and indicate that quantitative information can be obtained from CP/MAS kinetics obtained under similar experimental conditions.

3.1 Introduction

Dissolved organic matter is common in natural water systems from which calcite precipitates, and its presence at the calcite/fluid interface can affect precipitation and dissolution rates of calcite. These interactions depend to a large degree on the detailed organic molecular structures [1-6], so that knowledge of molecular level structure is of fundamental importance for understanding these surface interactions. Although calcite/organic interactions are clearly important for biomineralization, even calcite precipitated inorganically in natural low temperature environments contains organic molecules in 'intracrystalline' forms [7-11]. Disorder of the defects and presence primarily of light elements are impediments for applying X-ray scattering or absorption techniques to obtain structural information for this and similar systems. NMR spectroscopy has the advantage of being sensitive to local molecular structures and the relevant light elements, such as ^{13}C, ^{1}H, and ^{15}N, and hence is a potentially useful tool for the study of natural and synthetic mineral/organic composites. Cross polarization/magic angle spinning (CP/MAS) NMR can be used to selectively observe those carbons, which are close to protons in nominally anhydrous materials, and to probe the heteronuclear spatial proximity between defects and the calcite host [6,12-15].

In a previous study of synthetic calcite/citrate composites containing ~1 wt% citrate, $^{13}C\{^{1}H\}$ CP/MAS and heteronuclear correlation (HetCor) NMR results showed that the citrate methylene protons are located near the carbonate carbons, indicating that

the citrate molecules are dispersed within the calcite crystals as defects. In addition, it was found that a significant amount of rigid structural H_2O was associated with the organic defect, suggesting that hydrogen bonding plays a role in these interfacial interactions [12]. However, no specific geometrical or stereochemical information could be obtained about this calcite-host/citrate-defect structure. The goal of the present work is to obtain more quantitative structural information by measuring calcite/citrate heteronuclear distances using NMR spectroscopy.

Several NMR techniques are well established for measuring distances between heteronuclear atoms. The rotational echo double resonance (REDOR) technique has been applied to isolated heteronuclear spin pairs, yielding internuclear distances with accuracy comparable to those obtained by X-ray diffraction [16]. For example, particularly successful applications of REDOR have included $^{13}C–^{15}N$ distance measurements in singly or doubly labeled biological solids [17-19]. Alternately, description of CP/MAS has also been developed for isolated spin pairs, which allows the heteronuclear distance to be obtained by fitting the peak intensity variations with contact time to an analytical equation [20,21]. In most materials, however, the condition of truly isolated spin pairs is not a realistic assumption [22], which limits the direct quantitative applications of these techniques. REDOR has been extended to multispin systems ($S–I_n$) either by modifying REDOR equations to take more spins into account [23], or by fitting the data at short evolution time to obtain approximate values of the heteronuclear dipolar second moment

M_2 [22], which characterizes a sum over distances raised to the inverse 6th power. Such scalar properties can provide constraints on possible geometries and be useful for testing computational structural models. The quantitative REDOR measurements can be sensitively influenced by some experimental conditions, such as finite pulse length, pulse imperfections, and spinning stability [24]. We have also found that the application of multispin REDOR can be prohibitively time consuming for examining defect-level concentrations, since the relative error at short evolution time (i.e. $\Delta S/S_0 < 0.3$) is much larger than that at long evolution time.

In the present work, we examine the CP/MAS method for obtaining an approximate value of the heteronuclear second moment (M_2) that is suitable for components present at low concentrations, by establishing a correlation between the CP kinetics and the corresponding second moment, using model compounds with well-characterized structures. We chose the 3 : 2 compounds of Mg(II) citrate and Sr(II) citrate, of which the carboxyl and central carbons exhibit weak to moderate dipolar coupling to protons of citrate and crystal H_2O, hence comprising classical CP systems. The crystal structures of these compounds have been reported [25,26], including all H positions, so that the heteronuclear dipolar coupling M_2^{CH} can be calculated for each carbon site. Furthermore, both compounds contain multiple inequivalent carbons, thus several correlation points can be obtained from each of the compounds. This method is suitable for classical CP systems with weak heteronuclear coupling and can be applied under

experimental conditions easily obtained for large-volume sample configurations required by low concentrations.

3.2 Experimental

3.2.1 Materials

Magnesium(II) citrate decahydrate $[Mg(H_2O)_6][MgC_6H_5O_7(H_2O)]_2 \bullet 2H_2O$ (Mg(II)-cit) was prepared by mixing 40 ml of 2.1 M $MgCl_2$ and 40 ml of 1.4 M sodium citrate solutions in stoichiometric ratios. Stirring this solution with gentle heating, white precipitates appear in about 1 h. Strontium(II) citrate pentahydrate $[Sr_3(C_6H_5O_7)_2] \bullet 5H_2O$ (Sr(II)-cit) was synthesized by mixing 40 ml of 0.12 M $SrCl_2$ and 40 ml of 0.08 M sodium citrate solutions in a stoichiometric ratio, which quickly formed white precipitates. Partially deuterated samples were prepared similarly except using 70% D_2O as solvent.

For the preparation of zinc(II) 2,6-dihydroxybenzoate octahydrate $Zn[C_6H_3(OH)_2COO]_2 \bullet 8H_2O$ (Zn(II)-dhb), we first prepared a solution of 0.25 M sodium 2,6-dihydroxybenzoate (Na(I)-dhb) by dissolving the 2,6-dihydroxybenzoic acid at 80–90 °C and adding NaOH to adjust the pH to 10. Then 80 ml of 0.25 M Na(I)-dhb were mixed with 40 ml of 0.25M $Zn(acetate)_2$ solution at 80–90 °C. White precipitates appeared when the solution cooled down to room temperature. The kaolinite sample used in the study is a natural sample from Alta Mesa, NM (Wards Scientific). X-ray diffraction patterns obtained with a Scintag powder X-ray diffractometer and Cu Kα radiation for all these materials were consistent with their respective crystallographic data [25-28]. The calcite/citrate coprecipitate examined here is the same material as described previously

and denoted cc3109 [12]. This sample was synthesized in D_2O solvent at room temperature using a modified version of the seeded constant-addition method [29,30]. Briefly, 500 mg analytical reagent calcite (Alfa Aesar) were added as seeds to a reaction vessel containing 700 ml of an initial growth solution with 0.05 mM citric acid. The reaction vessel was maintained by addition of a mixture of citric acid and $CaCl_2$ (0.100 M $CaCl_2$, 0.5 mM citric acid and 0.050 M NaCl, pH = 5.6) and $Na_2{}^{13}CO_3$ (0.100 M $Na_2{}^{13}CO_3$, 0.050 M NaCl) solutions from syringes at a constant rate of 150 μl/min. D_2O (99%) was used as solvent for all solutions so that other H-bearing defects incorporated into the calcite are deuterated and the major source of ^1H is from citrate molecules. This sample is ~99% ^{13}C-enriched for carbonate carbon in the overgrowths and contains approximately 1 wt% citrate (natural ^{13}C abundance). Data are also presented for a second sample that was prepared similarly but with natural isotopic abundances.

3.2.2 NMR spectroscopy

All solid-state NMR spectra were collected on a 400 MHz (9.4 T) Varian Inova spectrometer. For $^{13}C\{^{1}H\}$ CP/MAS experiments, we used a Varian/Chemagnetics 'T3' probe assembly configured for 7.5 mm (outer diameter) rotors with samples packed into the middle 1/3 of the rotor volume to optimize radiofrequency (RF) homogeneity. All the $^{13}C\{^{1}H\}$ CP/MAS spectra for determining CP kinetics were obtained at 3.0 kHz spinning rate (ν_{rot}) with 6 μs excitation pulses (90°) for ^{1}H, unless indicated otherwise. During the spin-locking period, the transverse fields were $\nu_{1,H}$ = 41.7 kHz and $\nu_{1,C}$ = 38.5 kHz, corresponding to the first sideband match condition $\nu_{1,C} = \nu_{1,H} - \nu_{rot}$. We used CWCP,with no modulation of either pulse amplitudes or phases. For Mg(II)-cit and Sr(II)-cit, the variable contact time CP/MAS experiments for determining the CP kinetics were conducted separately for the carboxyl carbons and the central C–OH carbons, each with their center bands close to the carrier frequency, to reduce the effects of resonance offset on polarization transfer efficiency during the spin-locking period. For Zn(II)-dhb, the RF carrier is also set close to the center bands of carboxyl, –C–OH and C*–COO− carbons respectively. The ^{13}C single pulse spectrum for calcite/citrate coprecipitate was collected as a single acquisition after overnight equilibration (12 h), due to extremely slow spin lattice relaxation. The $^{29}Si\{^{1}H\}$ CP/MAS experiments for kaolinite were set up with the same probe configurations and experimental conditions.

^{2}H single pulse MAS spectra were obtained using a 4 mm Chemagnetics probe at 8 kHz spinning rate, and all the ^{2}H MAS spectra were analyzed by simulation or iterative fitting using the STARS computer program [31].

3.2.3 Chemical shift calculations

Standard methods and basis sets of molecular orbital theory as implemented in Gaussian 03 [32], including HF/6-31G(d,p), HF/6-31+G(d,p), HF/6-311+G(d,p), B3LYP/6-311+G(d,p) and B3LYP/6-31G(d,p) [33-37], were employed to obtain ^{13}C NMR chemical shielding tensors using the gauge-including atomic orbital (GIAO) method of Wolinski *et al* [38]. The chemical shifts were evaluated based on subtracting the isotropic chemical shielding of each C atom from the value obtained using the same methodology on the NMR standard compound trimethylsilane (TMS). This technique has proven effective in the past for predicting ^{13}C chemical shifts of organic acids to within a few ppm. Three different model sizes were created to investigate possible system size effects on calculated ^{13}C NMR chemical shifts. These models consist of 6 Mg^{2+} + 3 citrate molecules, 6 Mg^{2+} + 4 citrate molecules, and 7 Mg^{2+} + 6 citrate molecules, respectively. Water molecules, H atoms, and OH groups were added to the Mg^{2+} ions to complete the coordination sphere and charge balance the cluster. In addition, NMR calculations were run on the largest of these three models with the experimental atomic coordinates fixed, then the H atoms were allowed to relax to account for changes in O–H bond length and the NMR shieldings were recalculated. This procedure allowed us to check for the effect of H-bonding on the O–H bond length and the isotropic chemical shielding of C atoms bonded to OH groups.

3.3 Resulsts

3.3.1 CP kinetics of Mg(II)-cit and Sr(II)-cit

3.3.1.1 $^{13}C\{^{1}H\}$ CP/MAS spectra and kinetics of Mg(II)-cit and Sr(II)-cit

$^{13}C\{^{1}H\}$ CP/MAS NMR spectra of Mg(II)-cit and Sr(II)-cit are shown in Fig. 3.1. For Mg(II)-cit (Fig. 3.1a), the presence of three peaks arising from carboxyl carbons (δ_{C-13} = 184.5, 179.9, 178.1 ppm), one peak from central carbon (C–OH, δ_{C-13} = 78.1 ppm) and two relatively poorly resolved peaks from methylene groups (near 50 ppm) is consistent with the crystal structure data determined by X-ray diffraction [25]. For Sr(II)-cit (Fig. 3.1b), the presence of two peaks from central carbons (C–OH, δ_{C-13} = 77.2, 74.8 ppm) is also consistent with the reported crystal structure [26]. However, although the crystallographic data indicate six inequivalent carboxyl carbons in the Sr(II)-cit structure, only five peaks are observed in the corresponding spectral region (~180 ppm). We attribute this discrepancy to the peak at 179.6 ppm representing a superposition of two carboxyl positions with nearly identical isotropic chemical shifts. This explanation is supported by the CP kinetics of this peak, which yielded a total intensity for this peak approximately twice that for the other carboxyl peaks, indicating the intensity of this peak arises from two sites. For comparison, a $^{13}C\{^{1}H\}$ CP/MAS spectrum of a calcite sample containing approximately 1 wt % citrate is shown in Fig. 3.1c. This spectrum contains

peaks for the citrate defects at positions similar to those observed for crystalline Mg(II)-cit and Sr(II)-cit, but which are broad indicating a distribution of local configurations. The peak from carbonate groups (167.8 ppm) dominates the spectrum but is truncated in Fig. 3.1c for clarity. Previous HETCOR results [12], however, show that water molecules are the dominant ^{1}H reservoir for carbonate ions in this sample.

For each sample, the CP kinetics were measured separately for the central and carboxyl carbons by setting the RF carrier close to the frequency of the center band of the respective resonances in order to reduce any resonance-offset effects on the CP rates. The variation of the peak intensity with contact time (τ_{CP}) for each inequivalent carbon were fit to the CP dynamics equation,

$$M^{C}(\tau_{CP}) = M_0^{C} \cdot \left(1 - \frac{T_{CH}}{T_{1\rho,H}}\right)^{-1} \left[1 - \exp\left(-\frac{(1-\lambda)\tau_{CP}}{T_{CH}}\right)\right] \exp\left(-\frac{\tau_{CP}}{T_{1\rho,H}}\right); \quad for\ T_{1\rho,C} >> T_{1\rho,H} \qquad (3.1)$$

where M_0^{C} is a constant related to the number of ^{13}C in dipolar contact with ^{1}H, T_{CH} is the CP time constant for ^{13}C–^{1}H polarization transfer, $T_{1\rho,H}$ and $T_{1\rho,C}$ are spin-lattice relaxation times in the rotating frame for ^{1}H and ^{13}C, respectively, and $\lambda = T_{CH}/T_{1\rho,H}$ [39]. This equation is applicable in the thermodynamic limit, under the conditions of $T_{1\rho,C} >> T_{1\rho,H}$, the amount of ^{13}C is much less than that of ^{1}H (i.e. $N_{13C}/N_{1H} << 1$) and the sample spinning rate is relatively low compared with the ^{1}H homonuclear dipolar coupling [40,41], but is more typically used empirically as a means for describing experimental data. Allowing $T_{1\rho,H}$, T_{CH}, and M_0^{C} to vary freely, Eqn (3.1) yielded an excellent fit to the

data for all the carboxyl and central carbon signals, from which the CP times T_{CH} were obtained (Table 3.1). It should be noted that the peak at 179.6 ppm in the spectrum of Sr(II)-cit represents signals arising from two carbon sites as stated above, so the intensity variations were fitted to a sum of two curves. The average values of ^{1}H $T_{1\rho,H}$ are 5.0 and 2.9 ms for Mg(II)-cit and Sr(II)-cit respectively. The $T_{1\rho,H}$ values obtained for the different peaks in each compound were the same within errors, indicating that ^{1}H decays as a single spin system for both samples.

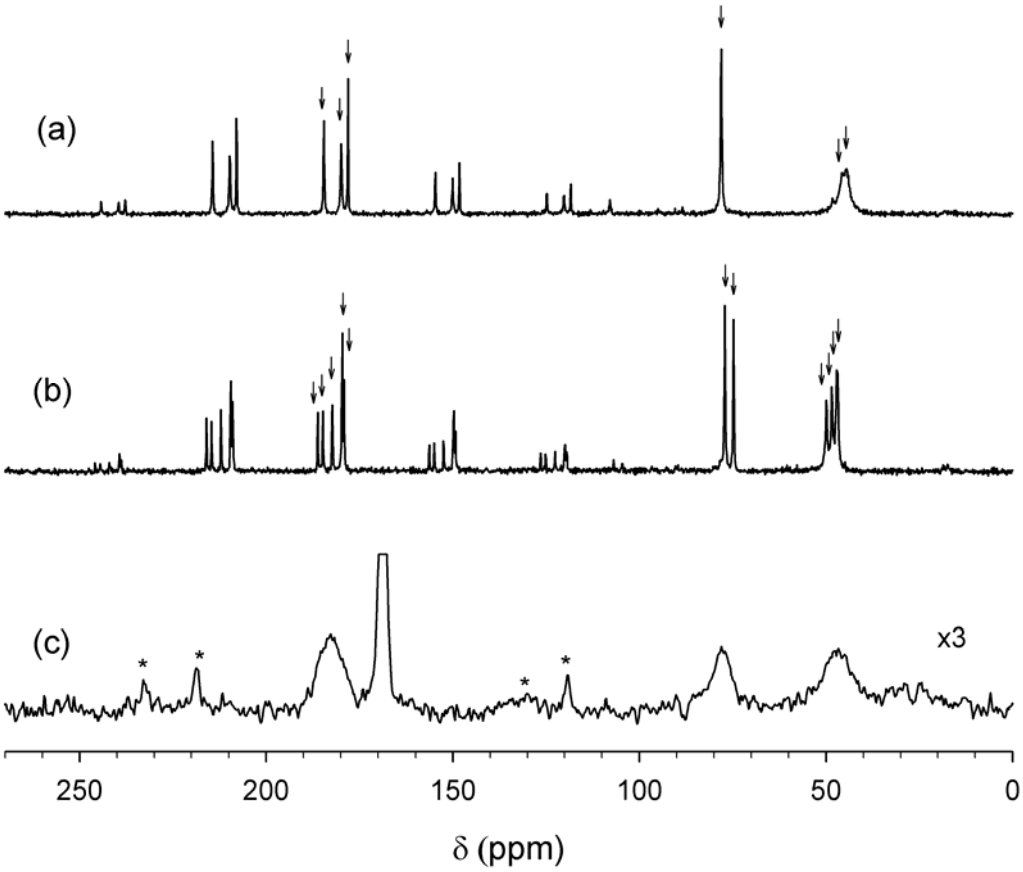

Figure 3.1 $^{13}C\{^{1}H\}$ CP/MAS NMR spectra of (a) Mg(II)-cit; (b) Sr(II)-cit; (c) citrate/calcite coprecipitate (natural 13C abundance) with 3x vertical scaling and peak from carbonate groups (167.8 ppm) truncated. Both (a) and (b) acquired at 3 kHz spinning rate, 1.2–1.3 ms contact time; (c) obtained with 5 ms ramped CP and 5 kHz spinning rate. Arrows denote the center bands; all other peaks are spinning sidebands.

Table 3.1 Calculated heteronuclear dipolar Second Moments M_2^{IS} of Mg(II)-cit, Sr(II)-cit, Zn(II)-dhb, kaolinite as well as experimentally measured T_{IS}^{-1}.

Compounds	Functional Groups	Atom Position [a]	Second Moment M_2^{IS} (10^6 s^{-2})	Isotropic Chemical Shift (ppm)	T_{IS}^{-1} (ms^{-1})
Mg(II)-cit	Carboxyl	C6	4.19	184.5	1.5 ± 0.09
		C5	8.00	179.9	2.8 ± 0.15
		C1	6.92	178.1	2.7 ± 0.09
	central C-OH	C3	14.29	78.1	5.4 ± 0.16
	$-CH_2$	C2,C4	—	45.5, 44.4	n.d.
Sr(II)-cit	Carboxyl	C6	1.97	186.1	0.7 ± 0.12
		C12	1.99	184.8	0.8 ± 0.12
		C5	6.46	182.3	2.5 ± 0.17
		C1	5.97	179.6	2.0 ± 0.12
		C7	7.19	179.6	2.6 ± 0.12
		C11	7.54	179.1	3.1 ± 0.16
	central C-OH	C9	14.71	77.2	5.5 ± 0.15
		C3	13.22	74.8	4.8 ± 0.14
	$-CH_2$	C2, C4, C8, C10	—	49.8, 48.4, 47.1, 46.7	n.d.
Zn(II)-dhb	Carboxyl	C1	4.38	178.7	2.4 ± 0.11
	-C-OH	C3, C7	9.75 [b]	158.7	3.4 ± 0.13
	$-C^*-COOH$	C2	3.31	103.5	1.9 ± 0.12
	-CH	C4, C5, C6	—	133.1, 107.5, 105.9	n.d.

a. Atom labels are according to original papers which report the structures [25,26] (see Fig. 3.2).
b. Values given here are the average second moment or T_{CH}.
c. n.d., not determined.

(a)

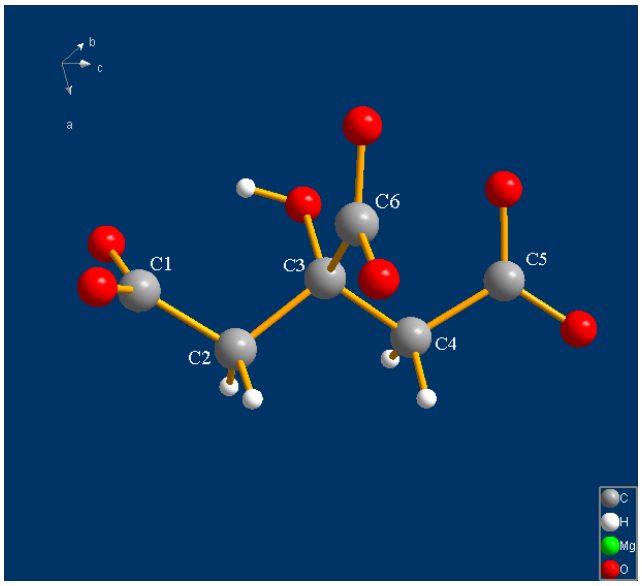

(b)

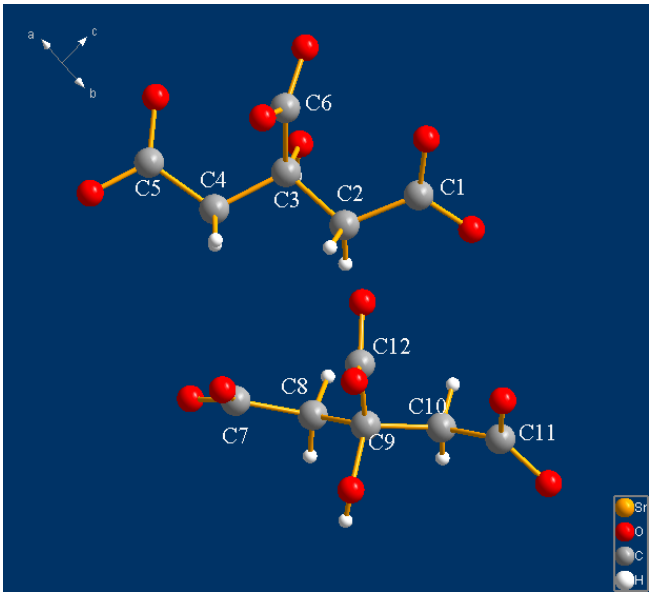

Figure 3.2 C atom (gray balls) labeling for Mg(II)-cit (a) and Sr(II)-cit (b) according to ref. [25,26].

3.3.1.2 Correlation of T_{CH}^{-1} *versus* M_2^{CH}

Assignment of the carboxyl resonances of Mg(II)-cit and Sr(II)-cit was accomplished by correlation of the measured T_{CH} values with the heteronuclear $^{13}C–^{1}H$ dipolar second moments (M_2^{CH}) calculated from the crystal structure. According to Mehring [39,42], the polarization transfer rate between carbon and proton systems in the classical limit is characterized by the CP time T_{CH}, which can be expressed as follows:

$$T_{CH}^{-1} = A \cdot M_2^{CH} \cdot C_x(\nu_1^C, \nu_1^H, \tau_c) \tag{3.2}$$

where A is a constant related to experimental settings, such as $\nu_{1,C}$, $\nu_{1,H}$ and the resonance offsets, and M_2^{CH} is the van Vleck second moment of the heteronuclear $^{13}C–^{1}H$ dipolar coupling, which is related to the $^{13}C–^{1}H$ distances (r_i). For a rigid lattice,

$$M_2^{CH} = \frac{4}{15}\gamma_H{}^2\gamma_C{}^2\left[\frac{\mu_0}{4\pi}\right]^2\left[\frac{\hbar}{2\pi}\right]^2 I_H(I_H+1)\sum_i r_i^{-6} \tag{3.3}$$

where γ_H and γ_C are gyromagnetic ratios for ^{1}H and ^{13}C, μ_0 is the vacuum permeability, $\hbar$ is the Planck constant over 2π, I_H is the ^{1}H nuclear spin quantum number and r_i is the internuclear distance between ^{13}C and the i^{th} ^{1}H. $C_x(\nu_{1,C}, \nu_{1,H}, \tau_c)$ is a function describing the influence of pulse strengths as well as $^{1}H–^{1}H$ homonuclear spin diffusion, represented by the correlation time τ_c. For non-protonated, weakly dipolar coupled carbons in the same phase, it is reasonable to expect the effects of $^{1}H–^{1}H$ spin diffusion on T_{CH} to be a constant (i.e. τ_c in Eqn (3.2) is a constant). Thus the T_{CH} for weakly coupled carbons in

each of the compounds can be correlated to the calculated M_2^{CH} according to the inversely proportional relationship.

The van Vleck dipolar second moment (M_2^{CH}) was calculated for each carbon position in Mg(II)-cit and Sr(II)-cit (illustrated in Fig. 3.2) according to Eqn (3.3) using crystal structure data from XRD [25,26]. To check whether the water molecules in Mg(II)-cit and Sr(II)-cit are rigid, we obtained ^{2}H MAS NMR spectra for partially deuterated samples. The ^{2}H MAS NMR spectrum of Sr(II)-cit (Fig. 3.3a) shows only a broad powder pattern characterized by the quadrupolar coupling constant C_Q = 0.20 MHz, indicating rigid crystal water molecules. The pattern of Mg(II)-(cit) (Fig. 3.3c) contains, however, some evidence of water molecules undergoing 180° 'flips' about the H–O–H bisector, producing added intensity in the central region compared to the spectrum for Sr(II)-cit (Fig. 3.3a). The narrow MAS sidebands indicate that the flipping motion is rapid. Assuming a two-site model of rigid plus flipping water molecules, a least-squares fit of the ^{2}H spectrum for Mg(II)-cit gives a ratio of flipping to rigid waters of approximately 0.31. For all the carboxyl carbons and the central C–OH carbon in Mg(II)-cit, the M_2^{CH} values calculated by assuming that all water molecules undergo flipping motions differ slightly from the values calculated assuming fully rigid water molecules, where the contributions from protons in flipping waters to M_2^{CH} are approximated using the average of two C–H distances. For Mg(II)-cit, the M_2^{CH} values given in Table 3.1 are

the averages of the two extreme cases, the range of which are indicated by the horizontal error bars in Fig. 3.4a.

For both Mg(II)-cit and Sr(II)-cit, assignments of carboxyl and central C–OH carbons in order of decreasing T_{CH} with increasing calculated M_2 (Table 3.1) produced a linear relationship between T_{CH}^{-1} and M_2^{CH} (Fig. 3.4a). A correlation curve with T_{CH}^{-1} *versus* M_2^{CH} can be obtained from a least-squares fit of the data for both Mg(II)-cit and Sr(II)-cit, which gives a slope of 0.37 [$(ms^{-1})/(10^6\ Hz^2)$] and intersects the origin. The fact that the slope for Eqn (3.2) is same for Sr(II)-cit and Mg(II)-cit suggests that ^1H–^1H spin diffusion is similar for both compounds. Considering that the ^1H density in Mg(II)-cit (48.9 H/nm^3) is higher than that of Sr(II)-cit (38.1 H/nm^3) and the different configurations for the crystal waters in the two samples, it appears that the effective ^1H–^1H spin diffusion (τ_c) is primarily determined by intramolecular protons in the citrate molecules.

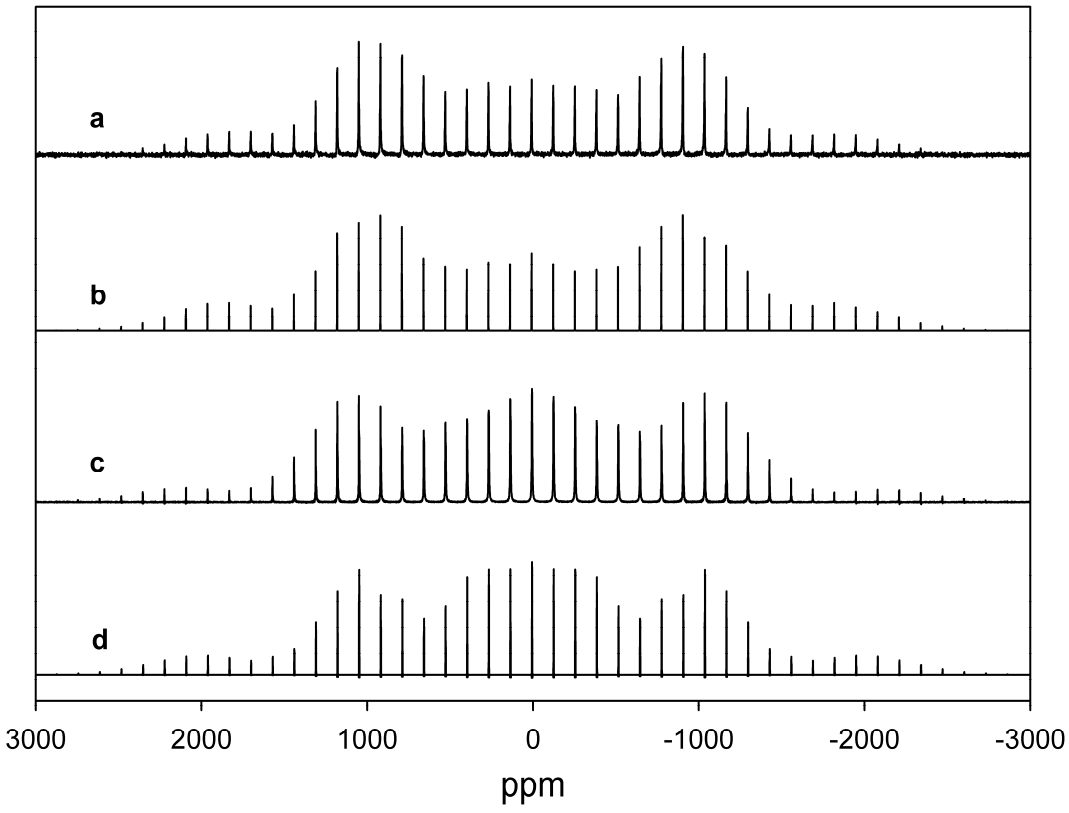

Figure 3.3 ^{2}H MAS NMR spectra obtained at 8 kHz spinning rate of (a) Sr(II)-cit prepared in D_2O. (b) simulated spectrum of Sr(II)-cit. (c) Mg(II)-cit prepared in D_2O. (d) simulated spectrum of Mg(II)-cit.

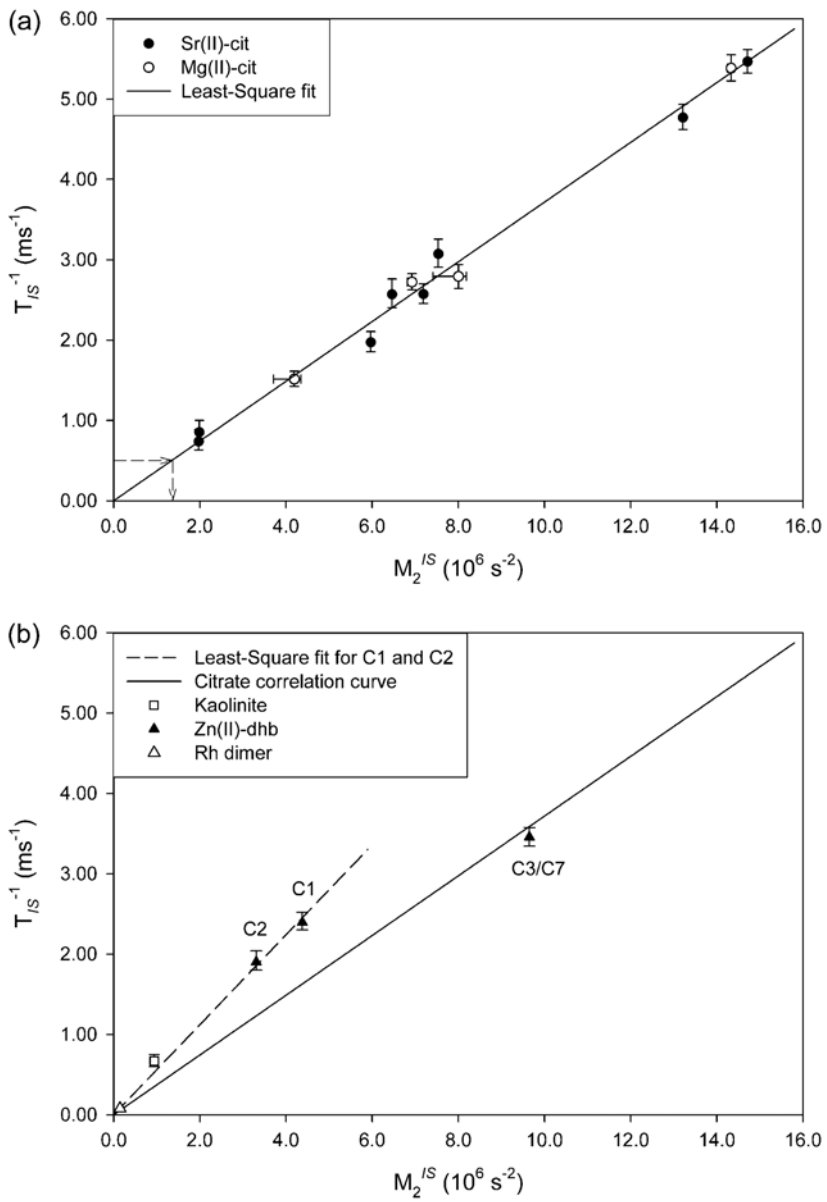

Figure 3.4 (a) Correlation curve of T_{IS}^{-1} *versus* M_2^{IS} from data are for Sr(II)-cit (●) and Mg(II)-cit (○) (Table 3.1). The solid line is a linear least-squares fit of the experimental data. Dashed arrows (--›) indicate the measurement of M_2^{CH} for calcite/citrate composite. (b) Comparison of the citrate correlation curve (—) with experimental CP/MAS kinetics data of kaolinite (□), Zn(II)-dhb (▲) and Rh-dimer (Δ). Dashed line (---) is linear least-squares fit for CP kinetics data of C1 and C2 in Zn(II)-dhb.

3.3.1.3 Chemical shift calculations

To test the assignments suggested by the T_{CH}^{-1} *versus* M_2^{CH} relationship, we also calculated the chemical shifts with Gaussian 03. We built three Mg(II)-cit clusters with different sizes, which are labeled respectively as small, medium, and large for convenience. All of these clusters contain a core citrate molecule, but differ in the completeness of more distant coordination environments. The small cluster (133 atoms) is built up exactly to the 2nd coordination shell with a few added hydrogen atoms to balance the charges. The medium cluster (184 atoms) is based on the small one, but with H_2O molecules coordinating to the outer Mg(II) ions, i.e. the structure contains some atoms from the 3rd and 4th coordination shell. The large cluster (218 atoms) contains the full 3rd coordination shell with complete citrate molecules. For these three model clusters, we first calculated chemical shieldings with fixed geometry from the crystal structure using the Hartree-Fock method and the 6-31+G(d,p) basis set to compare the cluster-size effects. As can be seen in Table 3.2, the calculated carboxyl chemical shifts of the core citrate molecule vary significantly with cluster size. For the large cluster, the calculated shieldings and measured chemical shifts are consistent with the peak assignments suggested by the T_{CH}^{-1} *versus* M_2^{CH} relationship (Table 3.2), but we noted some differences between calculated and measured values, especially for the central C–OH carbon. We then applied several basis sets and levels of calculation on the original large cluster and a modified large cluster produced by energy minimization for all OH protons

only. The results are listed in Table 3.3, which show that, although the calculated shieldings differ somewhat from the experimental chemical shifts, the relative differences among the distinct sites obtained from different basis sets or theory levels are all consistent with experimentally determined values. Relaxation of H atom positions improves agreement between observation and theory significantly, which is probably due to the original O–H bond lengths determined from XRD data being too short (e.g. approximately 0.86 versus 0.96 Å). These results strongly suggest that the peak assignments based on CP/MAS kinetics (i.e. Eqn (2)) are valid, and our assumption for Mg(II)-cit and Sr(II)-cit to be classical systems is reasonable.

Table 3.2 ^{13}C chemical shift values calculated with HF/6-31+G(d,p) method and basis sets for the three Mg(II)-cit clusters with different size, corresponding to 133 (small), 184(medium) and 218 atoms (large).

	Position	Experimental Chemical Shift (ppm)	Calculated (small) (HF/6-31+g)	Calculated (medium) (HF/6-31+g)	Calculated (large) (HF/6-31+g)
Carboxyl	C-6	184.5	185.6	181.2	184.9
	C-5	179.9	187.6	181.2	182.8
	C-1	178.1	175.1	174.9	176.5
Central C-OH	C-3	78.1	68.6	69.8	69.7

Table 3.3 ^{13}C chemical shifts of large Mg(II)-cit cluster calculated using variable methods and basis sets.

	Atom Position	Measured Chemical Shift (ppm)	Reported structure		Geometry optimized (H positions only)			
			HF/ 6-31g	HF/ 6-31+g	HF/ 6-311+g	HF/ 6-31g	b3lyp/ 6-311+g	b3lyp/ 6-31g
Carboxyl	C-6	184.5	185.0	184.9	195.5	185.7	191.9	177.0
	C-5	179.9	180.9	182.7	192.2	181.0	186.9	170.5
	C-1	178.1	176.2	176.5	185.5	176.4	177.6	164.9
Central C-OH	C-3	78.1	70.8	69.7	72.4	71.5	85.2	80.5

3.3.2 $^{13}C\{^1H\}$ CP/MAS spectra and kinetics of Zn(II)-dhb and kaolinite

To examine the variation of the T_{CH}^{-1} *versus* M_2^{CH} relationship with homonuclear ^1H–^1H coupling, we also measured CP kinetics for Zn(II)-dhb and kaolinite, which have well-known crystal structures with H positions. The $^{13}C\{^1H\}$ CP/MAS NMR spectrum of Zn(II)-dhb (Fig. 3.5a) contains a peak at 178.7 ppm, which is assigned to the carboxyl carbon, and five other peaks with center bands at 158.7, 133.2, 107.5, 105.9, and 103.5 ppm, respectively. The spectrum shown in Fig. 3.5a was acquired at 4 kHz spinning rate, to better show the isotropic peaks. The CP kinetics was measured with 3 kHz spinning rate, where the isotropic peak at 133.2 ppm overlaps with the $n = -1$ sideband of the carboxyl peak (178.7 ppm). The peak assignments were made according to the CP kinetics data and agree with well-established variations in ^{13}C chemical shift with molecular structure [27]. The peaks at 133.2, 107.5, and 105.9 ppm do not exhibit classical CP kinetics, showing oscillations with large amplitudes which are typical for rigid –CH groups [20,21]. Therefore, these peaks are assigned to the three –CH carbons in the benzene ring and are not considered further in the present context. The intensity variations of the peaks at 178.7, 158.7, and 103.5 ppm with contact time are described well by Eqn (1), suggesting these peaks arise from carbons lacking directly bonded H. The fitted value of M_0^C for the peak at 158.7 ppm is twice of those for the carboxyl carbon at 178.7 ppm and the peak at 103.5 ppm, which indicates that this peak is the superposition of two carbon signals with identical chemical shifts. From the crystal

structure of Zn(II)-dhb, we can assign this peak at 158.7 ppm to the two –C–OH carbons, since both carbons are not directly bonded to H and have similar chemical environments and nearly equal calculated M_2^{CH}. This assignment is also consistent with the relationship between T_{CH}^{-1} and M_2^{CH}, as listed in Table 3.1, where the M_2^{CH} are calculated according to Eqn (2) assuming a rigid lattice. With these assignments, the $^{13}C\{^1H\}$ CP/MAS spectrum and corresponding kinetics data are consistent with the reported crystal structure [27].

The $^{29}Si\{^1H\}$ CP/MAS NMR spectrum of kaolinite (Fig. 3.5b) contains two distinct peaks at −90.86 and −91.50 ppm, which is consistent with the spectra obtained by Hayashi *et al* [43]. However, both the T_{SiH} determined from the CP kinetics data and the calculated M_2^{SiH} based on the crystal structure [28] are nearly identical so that peak assignments cannot be made based on CP kinetics alone. Since our primary interest is the relationship between T_{SiH} and M_2^{SiH}, we treat both peaks as one point in the CP kinetics plot using the average values (Fig. 3.4b).

The comparison of the CP kinetics data of Zn(II)-dhb and kaolinite with the correlation curve obtained for Mg(II)-cit and Sr(II)-cit is illustrated in Fig. 3.4b. Also included are the $^{103}Rh\{^1H\}$ CP kinetics data for an aqua complex of a dihydroxy-bridged Rh dimmer measured previously [44], which exhibits weak heteronuclear coupling owing to the small value of γ_{Rh-103}. These data lie reasonably close to the correlation derived from Mg(II)-cit and Sr(II)-cit. The deviations are primarily due to the different ^1H–^1H

homonuclear dipolar couplings among these materials (i.e. the parameter τ_c in Eqn (2)). The role of homonuclear dipolar couplings is discussed further below. A similar correlation curve was obtained for $^{29}Si\{^1H\}$ CP/MAS by Fyfe *et al*. [45] in a study of ZSM-5/p-xylene. The slope of the correlation curve from the zeolite/p-xylene complex, 0.87 [$(ms^{-1})/(10^6\ Hz^2)$], is larger than that obtained from Mg(II)-cit and Sr(II)-cit [0.37 $(ms^{-1})/(10^6\ Hz^2)$] and Zn(II)-dhb [for C1 and C2, 0.56 $(ms^{-1})/(10^6\ Hz^2)$], but smaller than that obtained from kaolinite [1.02 $(ms^{-1})/(10^6\ Hz^2)$]. These differences can be attributed in part to the differences of ^1H homonuclear dipolar coupling between these systems, but the different ν_1 used in Ref. [45] could also have an effect.

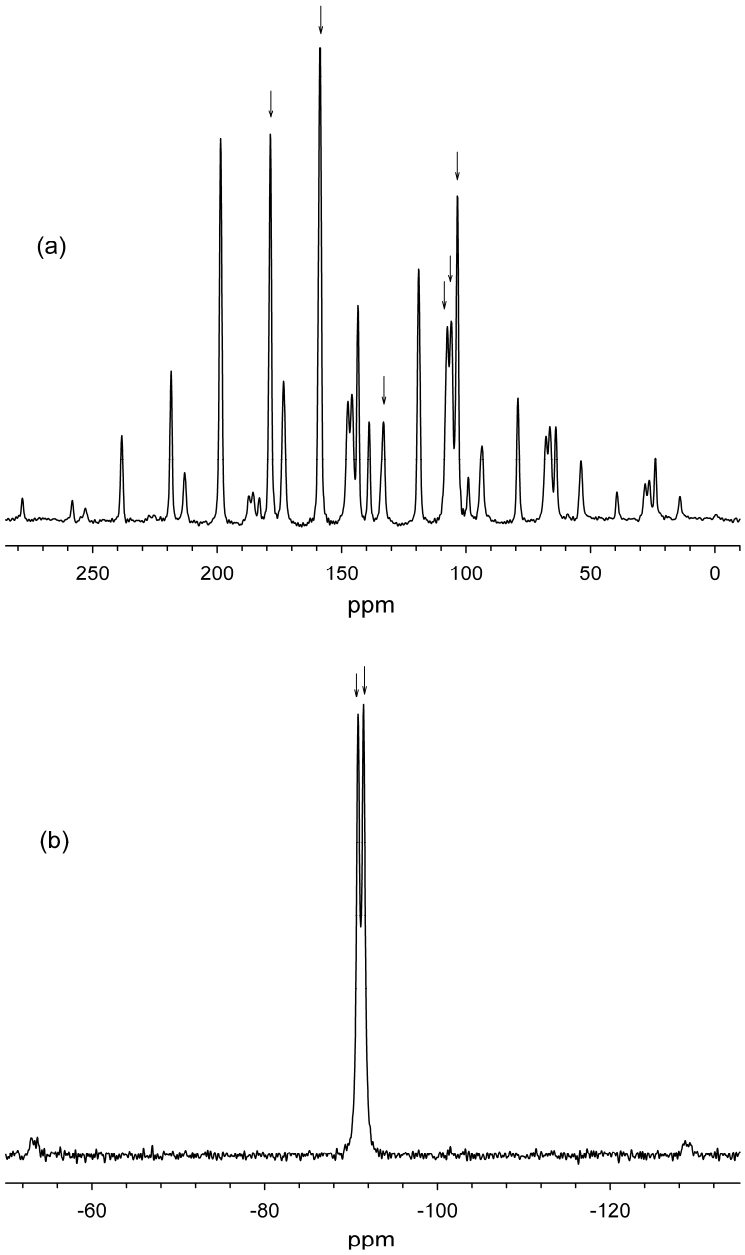

Figure 3.5 (a) $^{13}C\{^{1}H\}$ CP/MAS spectrum of Zn(II)-dhb, acquired with 2 ms contact time at 4 kHz spinning rate; (b) $^{29}Si\{^{1}H\}$ CP/MAS spectrum of kaolinite, acquired with 5 ms contact time at 3 kHz spinning rate. Arrows denote the center bands.

3.3.3 $^{13}C\{^1H\}$ CP dynamics of a calcite/citrate coprecipitate

The $^{13}C\{^1H\}$ CP/MAS NMR spectrum of the calcite/citrate coprecipitate (Fig. 3.6a) contains a single peak at 168.7 ppm arising from carbonate carbon (^{13}C-enriched). The chemical shift value is identical within error to that of carbonate carbon in the bulk mineral obtained by ^{13}C single pulse excitation (Fig. 3.6b). However, the peak in the CP/MAS spectrum is much broader (1.4 ppm of FWHH compared to 0.3 ppm of that in SP spectrum), indicating some distortion of the calcite structure near these organic defects. This sample was prepared in D_2O solvent, making citrate molecules the dominant ^1H reservoir in the calcite. The CP kinetics curve was obtained by fitting the variation of the peak intensity with contact time to a modified classical kinetics equation [39],

$$M^C(\tau_c) = M_0^C \cdot (1 + N_{13C} / N_{1H})^{-1} \cdot \left[1 - \exp\left(-\frac{(1 + N_{13C} / N_{1H})\tau_c}{T_{CH}}\right)\right] \quad \textbf{(4)}$$

since the ^{13}C-enriched calcite/citrate composite is unconventional for CP in the sense that the sample contains much more ^{13}C than ^1H. The assumption $N_{13C} << N_{1H}$ for Eqn (1) is no longer valid and the ratio N_{13C}/N_{1H} needs to be taken into account explicitly. The CP kinetics curve (Fig. 3.7) shows a classical pattern without any oscillation behavior, indicating that the heteronuclear dipolar coupling between carbonate carbons and citrate protons is weak compared with ^1H–^1H homonuclear coupling and that this system can be treated with the classical model. Furthermore, the ^{13}C–^{13}C dipolar interaction strength, calculated from crystal structure data as follows:

$$d_{^{13}C-^{13}C} = \left(\frac{1}{2\pi}\right)\cdot\left(\frac{\mu_0}{4\pi}\cdot\frac{\gamma_{^1H}\gamma_{^{13}C}\hbar}{r^3}\right) \cong 118\ Hz \qquad (5)$$

is much smaller than the applied spinning rate of 3 kHz, so that the ^{13}C–^{13}C homonuclear dipolar coupling can be neglected.

To estimate the number of carbonate carbons which are in dipolar contact with protons (i.e. the ratio N_{13C}/N_{1H} in Eqn (4)), we also collected a single pulse ^{13}C MAS spectrum of the coprecipitate (Fig. 3.6b) under conditions in which the intensity can be compared quantitatively to the corresponding CP experiment. Previous ^1H NMR results for this sample indicated a ^1H content of 0.21 mmol/g [12], so the ratio of protons to carbons is $^1H/^{13}C$ = 0.21 (mmol/g ^1H)/10 (mmol/g carbonate ^{13}C) = 0.021. Although hydroxyl protons are labile, previous work suggests that exchange did not occur significantly under the synthesis conditions [12], because both ^1H MAS spectra and $^{13}C\{^1H\}$ HETCOR spectra show a strong, relatively narrow peak at 5.3 ppm, which is very likely due to citrate hydroxyl protons. Assuming that the five protons of each citrate molecule are in dipolar contact with only one carbonate carbon, i.e. N_{13C}/N_{1H} = 0.2, then the ratio of maximum CP intensity to single pulse spectrum intensity should be

$$\frac{I_{CP}(\max)}{I_{SP}} = 0.021\cdot\frac{N_{13C}}{N_{1H}}\cdot\frac{\gamma_H}{\gamma_C}\cdot(1+\varepsilon)^{-1} = \frac{0.021}{5}\cdot 4\cdot\frac{1}{1.2} = 0.0140 \qquad \mathbf{(6)}$$

This value is in excellent agreement with experimental result 0.0139. The term $\gamma_H/\gamma_C\cdot(1+\varepsilon)^{-1}$ in the above expression represents the maximum signal enhancement by CP with respect to direct ^{13}C polarization. These results indicate that the citrate protons are in

dipolar contact only with the closest carbonate carbon of calcite, and a structural model for the citrate defect in calcite should contain on average only one carbonate group in close proximity to the citrate molecule. With $N_{13C}/N_{1H} = 0.2$, the least-squares fit of the data to Eqn (4) yields $T_{CH}^{-1} = 0.50 \pm 0.01$ (ms^{-1}). By comparison with the correlation curve obtained with Mg(II)-cit and Sr(II)-cit, the observed T_{CH} corresponds to $M_2^{CH} = 1.43 \cdot 10^6$ (s^{-2}) (denoted by dashed arrows in Fig. 3.4a), or $\sum_{i=1}^{n}[r_i(C-H_i)]^{-6} = 7.83 \times 10^{-3}$ ($Å^{-6}$) (Eqn (3)).

We also attempted to measure the $^{13}C–^{1}H$ heteronuclear dipolar coupling using a multispin REDOR experiment but failed due to low signal levels. An example of our measurements is shown in Fig. 3.8, which yields a fraction value $\Delta S/S_0 = 0.18$ but an uncertainty of ±0.11 arising from subtraction of spectra with low S/N ratio. The acquisition for this experiment took half a day, so presumably 12 days are needed to reduce the error to an acceptable 0.02 (~10%). Since five points are generally the minimum for a REDOR measurement, the total spectrometer time consumption would be at least 60 days. Considering that the application of the compensated sequence with an additional dummy pulse might be necessary to remove up to 20% of the systematic error [24], which is caused by the finite pulse length, pulse imperfections, spinning stability etc., the measurements with multispin REDOR would be extremely time-consuming for components at low concentrations or with long T_1, both of which characterize the calcite/citrate coprecipitate.

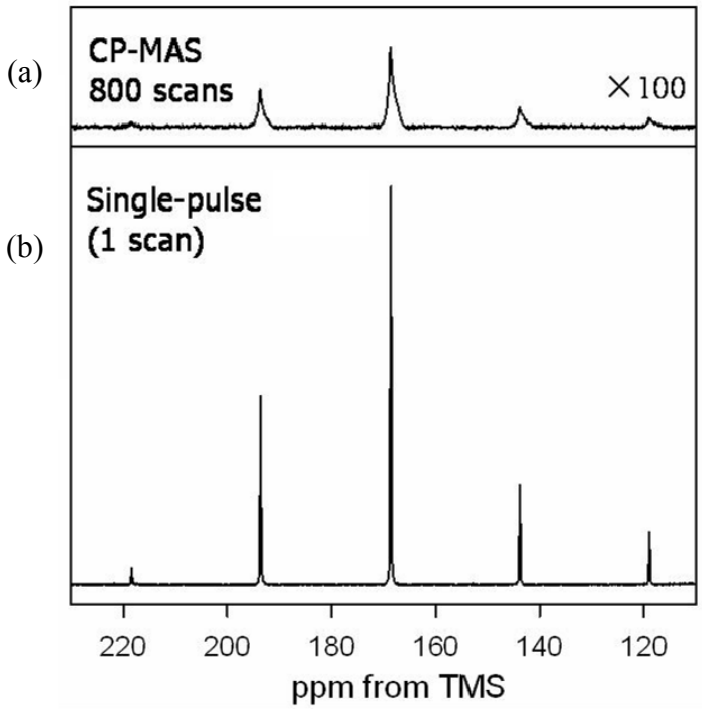

Figure 3.6 ^{13}C NMR spectra of calcite(^{13}C)/citrate coprecipitate synthesized in D_2O solvent. (a) $^{13}C\{^1H\}$ CP/MAS with 4 ms contact time, 2.5 kHz spinning rate, 10 s pulse delay, and 800 scans. (b) ^{13}C single pulse MAS, obtained as a single acquisition after 12 h equilibration period. Spectra scaled by absolute intensity with (a) multiplied by a factor of 100.

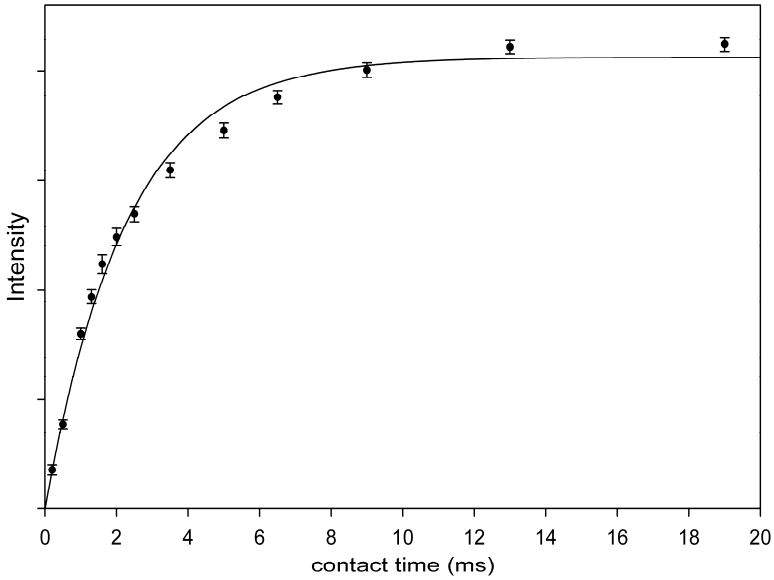

Figure 3.7 $^{13}C\{^{1}H\}$ CP kinetics of calcite(^{13}C-enriched)/citrate coprecipitate synthesized in D_2O solvent, acquired with CWCP at 3 kHz spinning rate and 10 s pulse delay.

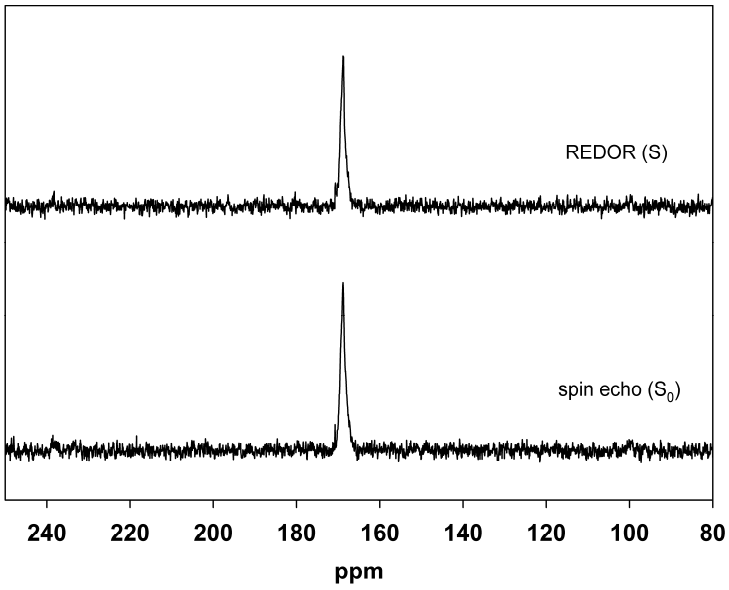

Figure 3.8 $^{13}C\{^{1}H\}$ CP-REDOR spectra of calcite(^{13}C)/citrate coprecipitate synthesized in D_2O solvent, acquired with four rotor cycles, 5 kHz spinning rate, 10 s ^{1}H pulse delay, 15 ms contact time, and 2200 scans.

3.4 Discussion

3.4.1 Citrate defects in calcite

Although estimated values of M_2^{CH} obtained by the above method cannot directly yield molecular structure, they can constrain the range of possible configurations and limit the models accordingly for further investigation. For example, one possible structural model for accommodation of the isolated citrate defect in calcite with citrate molecules in close proximity to carbonate groups involves hydrogen bonding between carbonate oxygen and the citrate hydroxyl group. Previous HETCOR NMR spectra [12] show that the hydroxyl ^{1}H chemical shift is 5.3 ppm, suggesting a hydrogen bond distance of d(OH···O) = 1.91 Å [46]. Assuming a reasonable geometry (linear OH···O; C–O···H ≈ 109.5°), yields a C–H (carbonate carbon to hydroxyl proton) distance of approximately 2.63 Å for this configuration, which corresponds to a second moment of 0.55×10^6 (s^{-2}), a value much smaller than that estimated from the measured T_{CH}, 1.43×10^6 (s^{-2}). In this configuration, the methylene protons are too far from the carbonate carbon to contribute more than a small fraction to the total second moment owing to its dependence on the inverse 6th power of the distance. Based on this, we conclude that the single hydrogen bonding model is not applicable and the carbonate carbon must also be in dipolar contact with methylene protons, as indicated by the ^{13}C{^{1}H} HETCOR spectra previously [12]. Alternatively, a maximum distance can be obtained by assuming that the

four methylene protons are equidistant to the carbonate carbon, giving a C–H (carbonate carbon to methylene protons) distance of 2.83 Å from the estimated M_2^{CH} and Eqn (3). This maximum distance indicates close association of the occluded citrate molecules with the calcite structure. Otherwise, a large number of specific configurations are possible, as reflected in the distribution of ^{13}C chemical shifts represented by the line width of the ^{13}C CP/MAS spectrum, but the associated geometrical term $\sum_{i=1}^{n}[r_i(C-H_i)]^{-6} = 7.83 \times 10^{-3}$ ($Å^{-6}$) can constrain computational models for a typical defect [47].

3.4.2 Estimating heteronuclear dipolar coupling from T_{IS}

The linear relationship between T_{IS}^{-1} and M_2^{IS} (more generally, where I denotes the directly excited nucleus and S is that observed by CP) is useful in the sense that it allows more quantitative information to be obtained from CP/MAS experiments that are easily measured even for difficult samples and at low concentrations. Observed T_{IS} parameters are usually compared qualitatively to distinguish S resonances based on relative distances to I nuclei (typically, ^{1}H). Direct quantitative information could be more meaningful in many cases, especially for those lacking relevant model compounds. For example, T_{IS} can be used to distinguish protonated and H-bonded oxyanions, such as carbonate or phosphate present as defects in a host phase or as adsorbed species in rigid systems. In these systems, if the H-bearing defects form isolated ^{13}C–^{1}H or ^{31}P–^{1}H spin pairs, the internuclear distances can be measured from the characteristic oscillations in the CP kinetics [15]. However, in most cases the oxyanions occur near other H-bearing components, such as rigid water molecules or hydroxyl groups, and yield classical CP kinetics. The internuclear distances cannot be obtained directly from T_{IS}, but the couplings from protonated groups can be distinguished. For example, for a singly protonated carbonate group, the distance between carbon and proton d(C–H) = 1.9 Å corresponds to a short T_{CH} = 0.7 ms that is otherwise very difficult to generate through hydrogen bonds only. As calculated above, a weak H bond with d(OH···O) = 1.91Å yields a long T_{CH} of 4.9 ms. Even a strong H bond with d(OH···O) = 1.5Å yields a T_{CH} =

2.1 ms, a value much larger than that expected for bicarbonate. Therefore, a T_{CH} smaller than or close to 0.7 ms suggests the existence of a bicarbonate, while a value larger than about 1 ms suggests that other H species are the source of the CP signal. Similarly, the citrate correlation yields T_{CH} = 10.8ms for a distance d(C–H) = 3 Å and distances of 4 ~ 5 Å correspond to T_{CH} values of 60 – 220 ms. These estimates clearly show that T_{CH} is very sensitive to the closest ^{13}C–^{1}H distance and place on a more quantitative basis the common statement that observation of CP signal requires S–H distances within a few Å, in agreement with other estimates for detectable heteronuclear coupling [48].

The CP kinetics for Zn(II)-dhb and kaolinite indicate that the effects of ^{1}H–^{1}H homonuclear dipolar coupling should be considered when applying the T_{IS}^{-1} *versus* M_2^{IS} correlations to other spin systems. For Zn(II)-dhb and kaolinite, the deviations of T_{IS} from the citrate correlation curve is presumably due to the smaller ^{1}H homonuclear dipolar couplings (Fig. 3.4b). Although no method is available for easily calculating the effective ^{1}H homonuclear dipolar coupling as it affects the CP rate directly from crystal structures, some information can be obtained by comparing the homonuclear second moments (M_2^{HH}) of the proton nearest to the observed site. For example, Zorin *et al.* [49] found that comparison of the root-sum-square dipolar coupling was relevant for understanding the effect of MAS rate on line width. Calculations show that the ^{1}H dipolar couplings for Zn(II)-dhb (H8, $M_2^{HH} = 1.24 \times 10^8$ s^{-2} and kaolinite (H2, $M_2^{HH} = 7.86 \times 10^7$ s^{-2}) are much weaker than that for Mg(II)-cit (H1, $M_2^{HH} = 5.33 \times 10^8$ s^{-2}), which explains the

observation that all the points for Zn(II)-dhb and kaolinite are above or close to the citrate correlation (Fig. 3.4b). It should also be noted that M_2^{HH} for the citrate compounds and the Zn(II)-dhb cover a fairly broad range of strong homonuclear dipolar couplings. In Mg(II)-cit and Sr(II)-cit, carboxyl and central C–OH carbons are in dipolar contact with the strongly coupled ^{1}H–^{1}H pairs from methylene groups. In Zn(II)-dhb, as a comparison, the ^{1}H nearest to those carbons with weak heteronuclear dipolar coupling (C1, C2, C3, and C7) is the relatively isolated proton from hydroxyl groups (i.e. H7 or H8), which couples to H_2O through weak H bonds (e.g. d(H(7)O(6)···H(5) = 2 Å). Most of the inorganic hydrous defects (i.e. systems containing H_2O and/or hydroxyl groups) which can induce classical CP kinetics are expected to have proton configurations with similar intermediate homonuclear dipolar couplings.

Considering the influence of the ^{1}H homonuclear dipolar coupling, the method for applying the T_{IS}^{-1} *versus* M_2^{IS} correlation depends on the range of the heteronuclear second moment. For weak heteronuclear dipolar couplings (i.e. $0 < M_2^{IS} < 2.0 \times 10^6$ s^{-2}), the correlation coefficient [0.37 (ms^{-1})/(10^6 s^{-2})] obtained from citrate compounds can be used, since the correlation for Zn(II)-dhb [dashed line in Fig. 3.4b; 0.56 (ms^{-1})/(10^6 s^{-2})] and that from citrates converge, and the difference in this range is comparable to typical measurement uncertainty. An example is the T_{Rh-H} for the H-dense Rh-dimer, which is estimated accordingly to be 18 ms, a value reasonably close to the experimentally measured 13 ms, considering the spin locking nutation frequency used in the ^{103}Rh{^{1}H}

CP/MAS experiments was much smaller than that applied in the current work [44]. Estimation of the T_{IS} could be especially useful in CP/MAS experiments for low-γ nuclei (e.g. ^{103}Rh), which generally exhibit long T_{IS} and low sensitivity, making it difficult to optimize the experimental parameters. Since the second moment is dominated by the short-range structure, the M_2^{IS} can be approximated by the intramolecular contributions for an estimate of the CP time, which combined with a measurement of $T_{1\rho,H}$ can provide anticipated CP kinetics.

For larger heteronuclear dipolar couplings, the present results suggest a range of estimates for the relationship between the second moment and CP rate. For example, when using the correlation to distinguish the protonated and H-bonded carbonates, a bicarbonate group with d(C–H) = 1.9 Å yields a T_{CH} between 0.45 to 0.70 ms according to Zn(II)-dhb correlation and citrate correlation respectively. For a H-bonded carbonate with d(OH···O) = 1.5 Å, T_{CH} is estimated to be in the range of 1.4 to 2.1 ms, which does not overlap with that obtained for bicarbonate. Therefore, the defect species can be potentially identified based on T_{CH}, if combined with the HETCOR spectra to estimate the H bond length [50].

The apparently distinct T_{CH}^{-1} *versus* M_2^{CH} relationships among the carbon sites C1, C2 *versus* C3/C7 for Zn(II)-dhb can be attributed to variation in the ^{1}H homonuclear dipolar couplings. The classical CP model requires that the dipolar coupling between ^{13}C and ^{1}H spin reservoirs is weak compared to the ^{1}H homonuclear coupling. For example,

the linear relationship between T_{CH}^{-1} *versus* M_2^{CH} appears to be valid at least until the heteronuclear second moment of 15×10^6 s^{-2} for citrate systems (Fig. 3.4a), so the carbons with second moments smaller than this value can be described by the classical model and correlated linearly with T_{CH}^{-1}, as the case of calcite/citrate composite. The ^1H homonuclear dipolar coupling in Zn(II)-dhb is weaker compared with that of citrate systems. The linear relationship between T_{CH}^{-1} and M_2^{CH} is, therefore, expected to be valid in a smaller range of M_2^{CH}. As can be seen in Fig. 3.4b, the C1 and C2 can still be fit by a straight line going through the origin (dashed line in Fig. 3.4b). As the M_2^{CH} becomes larger, deviation occurs for the CP kinetics data (C3/C7). This explanation is supported by the calculations of the dipolar coupling according to the crystal structure. From the structure data [27], the dipolar coupling of C1 with the nearest proton H7 is 2.3 kHz, which is much smaller than the 7.1 kHz between H7 and H5 (that nearest H7). However, the coupling of 5.7 kHz between C7 and the nearest proton H7 is comparable to that between H7 and H5. Presumably, the CP kinetics for C3/C7 is an intermediate case between classical and I–I*–S models [51]. The measured T_{CH} should represent an apparent value, and the kinetics data are expected to fit to the equation for I–I*–S models, if more data points are collected at initial contact time range [51,52]. The observation that the kinetics data for C3/C7 is below the correlation curve from C1 and C2 is consistent with slow ^1H spin diffusion serving as a bottleneck for polarization transfer. The direct $^{13}C\{^1H\}$ polarization transfer from distant protons is slow so that contact with the ^1H spin

reservoir beyond the nearest H is transferred indirectly, yielding a CP rate for C3/C7 slower than expected by the classical model.

3.5 Conclusion

Our results show that under carefully controlled experimental conditions the CP rate (T_{IS}^{-1}) is linearly proportional to the heteronuclear dipolar second moment (M_2^{IS}) as expected from the classical treatment of the CP experiment. A correlation was established from Mg(II)-cit and Sr(II)-cit, with 3 kHz sample spinning rate and the pulse fields of 41.7 and 38.5 kHz for ^{1}H and ^{13}C respectively. Based on the citrate correlation curve, the second moment for the large citrate defects in calcite/citrate coprecipitate could be obtained from the measurement of T_{IS}^{-1}. The estimated second moment value suggests that the surface interactions between citrate and calcite host is not through the direct hydrogen bonding and carbonate carbon should be close to the methylene groups of citrate. To apply the correlation to other spin-1/2 systems for measuring distances or optimizing CP experiments, the effects of ^{1}H homonuclear dipolar coupling should be considered.

3.6 References

1. Amjad Z, *Langmuir*, 1987, **3**: 224-228.

2. Geffroy C, Foissy A, Persello J, Cabane B, *J. Colloid Interface Sci.*, 1999, **211**: 45-53.

3. Orme CA, Noy A, Wierzbicki A, McBride MT, Grantham M, Teng HH, Dove PM, DeYoreo JJ, *Nature*, 2001, **411**: 775-779.

4. Reddy MM, Hoch AR, *J. Colloid Interface Sci.*, 2001, **235**: 365-370.

5. Teng HH, Dove, P. M., *Am. Mineral.*, 1997, **82**: 878-887.

6. Ueyama N, Hosoi T, Yamada Y, Doi M, Okamura T, Nakamura A, *Macromolecules*, 1998, **31**: 7119-7126.

7. Berman A, Addadi L, Kvick A, Leiserowitz L, Nelson M, Weiner S, *Science*, 1990, **250**: 664-667.

8. Neuweiler F, Rutsch M, Geipel G, Reimer A, Heise KH, *Geology*, 2000, **28**: 851-854.

9. Ramseyer K, Miano TM, DOrazio V, Wildberger A, Wagner T, Geister J, *Org. Geochem.*, 1997, **26**: 361-378.

10. Sykes GA, Collins, M. J., Walton, D. I., *Org. Geochem.*, 1995, **23**: 1059-1065.

11. Walton D, *Org. Geochem.*, 1998, **28**: 389-410.

12. Phillips BL, Lee YJ, Reeder RJ, *Environ. Sci. Technol.*, 2005, **39**: 4533-4539.

13. Takahashi K, Doi, M., Kobayashi, A., Taguchi, T., Onoda, A., Okamura, T. A., Yamamoto, H., Ueyama, N., *Chem. Lett.*, 2004, **33**: 192-193.

14. Ueyama N, Kozuki H, Doi M, Yamada Y, Takahashi K, Onoda A, Okamura T, Yamamoto H, *Macromolecules*, 2001, **34**: 2607-2614.

15. Feng J, Lee YJ, Reeder RJ, Phillips BL, *Am. Mineral.*, 2006, **91**: 957-960.

16. Gullion T, Schaefer J, *J. Magn. Reson.*, 1989, **81**: 196-200.

17. Christensen AM, Schaefer J, *Biochemistry*, 1993, **32**: 2868-2873.

18. Pan Y, Shenouda NS, Wilson GE, Schaefer J, *J. Biol. Chem.*, 1993, **268**: 18692-18695.

19. Hing AW, Tjandra N, Cottam PF, Schaefer J, Ho C, *Biochemistry*, 1994, **33**: 8651-8661.

20. Hediger S. *Improvement of heteronuclear polarization transfer in solid-state NMR*, Ph.D. dissertation, 1997. Eidgenössische Technische Hochschule, Zürich.

21. Fyfe CA, Lewis AR, Chezeau JM, *Can. J. Chem.*, 1999, **77**: 1984-1993.

22. Bertmer M, Eckert H, *Solid State Nucl. Magn. Reson.*, 1999, **15**: 139-152.

23. Goetz JM, Schaefer J, *J. Magn. Reson.*, 1997, **127**: 147-154.

24. Chan JCC, Eckert H, *J. Magn. Reson.*, 2000, **147**: 170-178.

25. Johnson CK, *Acta Crystallogr.*, 1965, **18**: 1004-&.

26. Zacharias DE, Glusker JP, *Acta Crystallogr., Sect. C-Cryst. Struct. Commun.*, 1993, **49**: 1732-1735.

27. Cariati F, Erre L, Micera G, Panzanelli A, Ciani G, Sironi A, *Inorg. Chim. Acta-Bioinorg. Chem.*, 1983, **80**: 57-65.

28. Neder RB, Burghammer M, Grasl T, Schulz H, Bram A, Fiedler S, *Clays Clay Miner.*, 1999, **47**: 487-494.

29. Tesoriero AJ, Pankow JF, *Geochim. Cosmochim. Acta*, 1996, **60**: 1053-1063.

30. Zhong SJ, Mucci A, *Geochim. Cosmochim. Acta*, 1993, **57**: 1409-1417.

31. Jakobsen HJ, Skibsted J, Bildsoe H, Nielsen NC, *J. Magn. Reson.*, 1989, **85**: 173-180.

32. Frisch MJ, Trucks GW, Schlegel HB, Scuseria GE, Robb MA, Cheeseman JR, Montgomery JA, Jr. , Vreven T, Kudin KN, Burant JC, Millam JM, Iyengar SS, Tomasi J, Barone V, Mennucci B, Cossi M, Scalmani G, Rega N, Petersson GA, Nakatsuji H, M. Hada, M. Ehara, K. Toyota, Fukuda R, Hasegawa J, Ishida M, Nakajima T, Honda Y, Kitao O, Nakai H, Klene M, Li X, Knox JE, Hratchian HP, Cross JB, Adamo C, Jaramillo J, Gomperts R, Stratmann RE, Yazyev O, Austin AJ, Cammi R, Pomelli C, Ochterski JW, Ayala PY, Morokuma K, Voth GA, Salvador P, Dannenberg JJ, Zakrzewski VG, Dapprich S, Daniels AD, Strain MC, Farkas O, Malick DK, Rabuck AD, Raghavachari K, Foresman JB, Ortiz JV, Cui Q, Baboul AG, Clifford S, Cioslowski J, Stefanov BB, Liu G, Liashenko A, Piskorz P, Komaromi I, Martin RL, Fox DJ, Keith T, Al-Laham MA, Peng CY, Nanayakkara A, Challacombe M, Gill PMW, Johnson B, Chen W, Wong MW,

Gonzalez C, Pople JA. *Gaussian 03*, Version: C.01. Gaussian Inc., Wallingford, CT, 2004.

33. Becke AD, *J. Chem. Phys.*, 1993, **98**: 5648-5652.

34. Gordon MS, Binkley JS, Pople JA, Pietro WJ, Hehre WJ, *J. Am. Chem. Soc.*, 1982, **104**: 2797-2803.

35. Krishnan R, Binkley JS, Seeger R, Pople JA, *J. Chem. Phys.*, 1980, **72**: 650-654.

36. Lee CT, Yang WT, Parr RG, *Phys. Rev. B*, 1988, **37**: 785-789.

37. Mclean AD, Chandler GS, *J. Chem. Phys.*, 1980, **72**: 5639-5648.

38. Wolinski K, Hinton JF, Pulay P, *J. Am. Chem. Soc.*, 1990, **112**: 8251-8260.

39. Mehring M. *Principles of high-resolution NMR in solids*. Springer-Verlag: Berlin, New York, 1983.

40. Stejskal EO, Memory JD. *High resolution NMR in the solid state : fundamentals of CP/MAS*. Oxford University Press: New York, 1994.

41. Michel D, Engelke F, *Solid-State NMR III: Organic Matter*, Blümich B (Ed.), 1994, **31**. Springer-Verlag, Berlin.

42. Demco DE, Tegenfeldt J, Waugh JS, *Phys. Rev. B*, 1975, **11**: 4133-4151.

43. Hayashi S, Ueda T, Hayamizu K, Akiba E, *J. Phys. Chem.*, 1992, **96**: 10922-10928.

44. Phillips BL, Houston JR, Feng J, Casey WH, *J. Am. Chem. Soc.*, 2006, **128**: 3912-3913.

45. Fyfe CA, Diaz AC, Grondey H, Lewis AR, Forster H, *J. Am. Chem. Soc.*, 2005, **127**: 7543-7558.

46. Yesinowski JP, Eckert H, Rossman GR, *J. Am. Chem. Soc.*, 1988, **110**: 1367-1375.

47. de Leeuw NH, Cooper TG, *Cryst. Growth Des.*, 2004, **4**: 123-133.

48. Gu ZT, Ridenour CF, Bronnimann CE, Iwashita T, McDermott A, *J. Am. Chem. Soc.*, 1996, **118**: 822-829.

49. Zorin VE, Brown SP, Hodgkinson P, *Mol. Phys.*, 2006, **104**: 293-304.

50. Brunner E, Sternberg U, *Prog. Nucl. Magn. Reson. Spectrosc.*, 1998, **32**: 21-57.

51. Kolodziejski W, Klinowski J, *Chem. Rev.*, 2002, **102**: 613-628.

52. Kaflak-Hachulska A, Slosarczyk A, Kolodziejski W, *Solid State Nucl. Magn. Reson.*, 2000, **15**: 237-238.

Chapter 4

Structural characteristics of synthetic amorphous calcium carbonate: an NMR spectroscopic study

Abstract

Amorphous calcium carbonate (ACC) is an important phase involved in calcification by a wide variety of invertebrate organisms and is increasingly of interest in the development of functionalized materials using templates. Despite widespread scientific interest in this phase a full characterization of its structure is lacking. This is mainly due to its metastability and difficulties in evaluating structure using conventional structure determination methods. Here we present new findings from the application of nuclear magnetic resonance spectroscopy, which provide new insight to structural aspects of synthetic additive-free ACC. $^{13}C\{^{1}H\}$ 2-D HETCOR NMR spectra show that most of the hydrogen in ACC is present as structural H_2O, about half of which undergoes restricted motion on the millisecond time scale near room temperature. The motion of H_2O can be significantly reduced by lowering the temperature to -120 °C, as is indicated by both $^{13}C\{^{1}H\}$ CP kinetics measurement and $^{13}C\{^{1}H\}$ HETCOR spectra. Combining

* Portions of this chapter were published at *Chemistry of Materials*, 2008, **20**, 4720

with the results from pair distribution function (PDF) analysis, the ^{13}C and ^{1}H chemical shift values also provide constraints on the identity and linkage of the CO_3 units in the synthetic ACC. In addition, we also demonstrate that ^{13}C single pulse MAS NMR spectra can be used as fingerprints for distinguishing various calcium carbonate polymorphs, including ACC, calcite, aragonite, monohydrocalcite and vaterite, so that the evolution process of ACC can be monitored in real-time by ^{13}C MAS spectra. Although the structure of ACC is still not fully understood, the results presented provide an important baseline for future experiments evaluating biogenic ACC and samples containing certain additives that may play a role in the stabilization of ACC, its crystallization kinetics, and final polymorph selection.

4.1 Introduction

It is now recognized that the amorphous calcium carbonate (ACC) is widely produced by calcifying invertebrate organisms as a precursor in the formation of final crystalline phases of biogenic $CaCO_3$, typically calcite or aragonite. Despite the metastable nature of the amorphous phase, organisms can provide temporary stabilization on ACC for days to weeks, control the kinetics of subsequent transformation, and select final phase and morphology. Many biogenic minerals contain organic molecules or matrices, forming mineral/organic composites possessing delicate structures and unique mechanical properties [1], which has attracted research efforts in this field during the last several decades [1,2]. The pathway through an amorphous precursor is a highly promising route, and has inspired the design and synthesis of functional calcium carbonate phases or composites [3,4].

For understanding the principles behind the biological control over the crystallization process, and the fundamentals of the complex interactions between mineral and organism, it is essential to elucidate the structure of amorphous calcium carbonate, which determines the properties of the mineral phase and constrains the interaction with the organic templates that may direct the assembly. In biogenic ACC, the presence of inorganic and organic impurities, as well as structural H_2O (most forms approximating $CaCO_3 \cdot H_2O$ in composition), implies that these components might play an important in stabilizing ACC and in controlling the following transformation [5].

However, the occurrence of multiple foreign components contained in natural samples also introduces complexities for the analysis of the functions of each additive and their respective effects on the structure of ACC. Therefore, much of the research effort has been focused on laboratory-synthesized ACC, for which proper experimental design can produce ACC with controlled impurity species and concentrations. The effects of each additive component on the structure and properties of ACC can thus be evaluated individually.

Structural characterization of ACC is difficult due to the amorphous nature of the material, which excludes the application of conventional X-ray diffraction techniques. The combined application of complementary techniques for local structure evaluation potentially provides a more complete picture of the ACC structure. Extended X-ray absorption fine structure (EXAFS) is a powerful technique for characterization of short-range structure. However, it primarily gives structural information limited to the first coordination sphere of Ca ions. Pair distribution function (PDF) analysis of the total X-ray scattering measures the probability for finding atomic pairs with a separation *r*, giving structural information for a material over relatively large length scales, but it is insensitive to H, which is a major component of most ACC. NMR spectroscopy has the advantage of providing element-specific information and for being sensitive to the relevant light elements, such as ^{1}H, ^{13}C etc. Consequently, it is particularly useful for understanding the role of protons (i.e., water and hydroxyls) in a structure. Furthermore,

double-resonance NMR techniques can also probe the proximity between atoms through dipole-dipole interactions.

In the present chapter we report findings obtained from application of nuclear magnetic resonance (NMR) spectroscopy, that provide new insight to structural aspects of synthetic ACC. This report focuses on additive-free ACC and provides a baseline for evaluation of biogenic samples as well as ACC samples containing additives. The ^{13}C and ^{1}H NMR data provide the first evidence for the structural role of water and the first constraints on the coordination of the CO_3 units in synthetic ACC. The ^{13}C single pulse MAS NMR spectra prove to be effective for characterizing the transformation pathway and kinetics of ACC.

4.2 Experimental

4.2.1 Synthesis of Amorphous Calcium Carbonate

Two different methods were used to synthesize ACC in this study. Method I was adapted from the procedure described by Koga et al. [6], in which calcium chloride and sodium carbonate solutions, equimolar in Ca and CO_3, were rapidly mixed. In this method 147 mg of solid sodium carbonate was added to 20 mL of a 0.5 M sodium hydroxide solution and 30 mL deionized water. This solution was combined with 50 mL of a 1 mM calcium chloride solution and stirred rapidly, followed immediately by vacuum filtration and rinsing with acetone to dry the solid. Samples for NMR analysis were prepared from sodium carbonate enriched to 99% in ^{13}C. Method II was derived from the procedure described by Faatz et al. [7] and differed primarily from method I by use of dimethyl carbonate as the CO_3 source. This method involves addition of 147 mg of solid calcium chloride and 450 mg of dimethyl carbonate to 80 mL deionized water, followed by addition of 20 mL of 0.5 M sodium hydroxide solution. This mixture was stirred for approximately 2.5 minutes, and the solid precipitate was vacuum-filtered and dried with acetone. Both methods were conducted at room temperature in open air.

4.2.2 NMR Techniques

Most solid-state NMR spectra were collected on a 400 MHz (9.4 T) Varian Inova spectrometer operating at 100.6 MHz for ^{13}C and 399.76 MHz for ^{1}H. $^{13}C\{^{1}H\}$ two-dimensional heteronuclear correlation (HETCOR) NMR spectra [8] were obtained using a Varian/Chemagnetics "T3" probe assembly configured for 3.2 mm (outer diameter) thin wall rotors. The HETCOR spectra were acquired at a 10 kHz spinning rate with 1 s acquisition delay and a linear ramp of the ^{13}C B_1 field during the contact time. To stabilize the initial ACC, the sample was dried in vacuum for 30 min after being loaded into the rotor, which was then sealed. ^{13}C single pulse magic angle spinning (SP/MAS) NMR spectra and $^{13}C\{^{1}H\}$ CP/MAS NMR spectra acquired before and after each HETCOR experiment showed no changes, indicating that no transformation occurred during the HETCOR acquisition. ^{1}H MAS NMR spectra were obtained under similar experimental conditions. $^{13}C\{^{1}H\}$ CP kinetics were measured with a Varian/Chemagnetics "T3" probe assembly configured for 7.5 mm (outer diameter) rotors. The experimental conditions for $^{13}C\{^{1}H\}$ CP/MAS NMR were 3 kHz spinning rate, 8 μs 90° ^{1}H excitation pulse, 1 s acquisition delay, and 32 kHz spin-locking (CW mode) power for ^{1}H channel and 29 kHz for ^{13}C during contact time corresponding to the 1st sideband match. For quantitative comparison, a ^{13}C SP/MAS NMR spectrum was obtained at 3 kHz spinning rate, with 8 μs 90° excitation pulse and 1 h acquisition delay due to the long spin-lattice relaxation time of ^{13}C.

4.3 Results and discussion

4.3.1 ^{13}C SP/MAS and ^{13}C{^{1}H} CP/MAS NMR spectra of ACC

The ^{13}C NMR spectra for the initial ACC synthesized using methods I and II are virtually identical and are characterized by a broad (3.6 ppm full-width at half maximum; fwhm), symmetric peak at a chemical shift of 169.0 ± 0.05 ppm (Fig. 4.1(a-b)). This feature is essentially identical whether acquired by SP or CP methods. For comparison, Fig. 4.1(c-f) show center bands of ^{13}C MAS NMR spectra acquired by either SP or CP methods of other calcium carbonate phases, including those for monohydrocalcite (Fig. 4.1d; δ_C (M) = 171.7 ppm, FWHH = 2.3 ppm) and vaterite (Fig. 4.1f; δ_C (V) = 170.7 ppm and 169.6 ppm, FWHH = 0.8 ppm), which have not been reported previously. Dotted lines in Fig. 4.1 represent the chemical shifts for calcite (Fig. 4.1c, δ_C (C) = 168.7 ppm, FWHH = 0.5 ppm) and aragonite (Fig. 4.1e, $\delta_{C\text{-}13}$ (A) = 171.0 ppm, FWHH = 0.5 ppm). The large peak width for ACC, which spans the ^{13}C chemical shift range of crystalline calcium carbonates, is much broader than that of the crystalline phases and is consistent with the amorphous nature of the initial ACC.

The ^{13}C{^{1}H} CP/MAS signal intensity varies with contact time (τ_c) according to classical biexponential kinetics [9,10] characterized by T_{CH} = 0.5 ms and $T_{1\rho,H}$ = 5.0 ms (Fig. 4.2), with 1 ms contact giving maximum signal intensity. The inferred $T_{1\rho,H}$ from the CP kinetics was confirmed by a ^{13}C-observed ^{1}H $T_{1\rho,H}$ measurement undertaken at a

constant τ_c = 1 ms. In terms of peak position and width, no variation in the ^{13}C CP spectrum was found with contact time.

Quantitative comparison of $^{13}C\{^1H\}$ CP kinetics with the ^{13}C SP/MAS spectra provides additional structural information of ACC. In the classical bi-exponential equation for CP kinetics, the parameter $I_{0,CP}$ represents the maximum possible ^{13}C signal enhancement by CP, which can be achieved for a system with negligible ratio of $N_{C\text{-}13}/N_{H\text{-}1}$, and infinitely long $T_{1\rho,H}$ and $T_{1\rho,C}$. Otherwise, $I_{0,CP}$ can be obtained from fitting the experimental CP kinetics data to the bi-exponential equation. At the Hartmann-Hahn condition, CP can improve the ^{13}C signal intensity by a factor of $\gamma_{H\text{-}1}/\gamma_{C\text{-}13}$ at best, i.e. $I_{0,CP}/I_{SP}$ = 4. However, at room temperature, a least-squares fit of the experimental CP kinetics for synthetic ACC to the classical bi-exponential equation (shown in Fig. 4.2) yields a maximum ratio $I_{0,CP}/I_{SP} \approx 1$, suggesting that only a small fraction (~ 1/4, assuming the ratio $N_{C\text{-}13}/N_{H\text{-}1}$ to be 1/2) of the carbonate carbons are in dipolar contact with rigid H. The $^{13}C\{^1H\}$ HETCOR NMR spectra and low temperature NMR results shown below indicate that a significant amount of structural H undergoes restricted motion, which reduces the CP efficiency. As a result, the maximum signal intensity per scan is lower for a CP/MAS experiment than for SP acquisition (Fig. 4.2, inset)

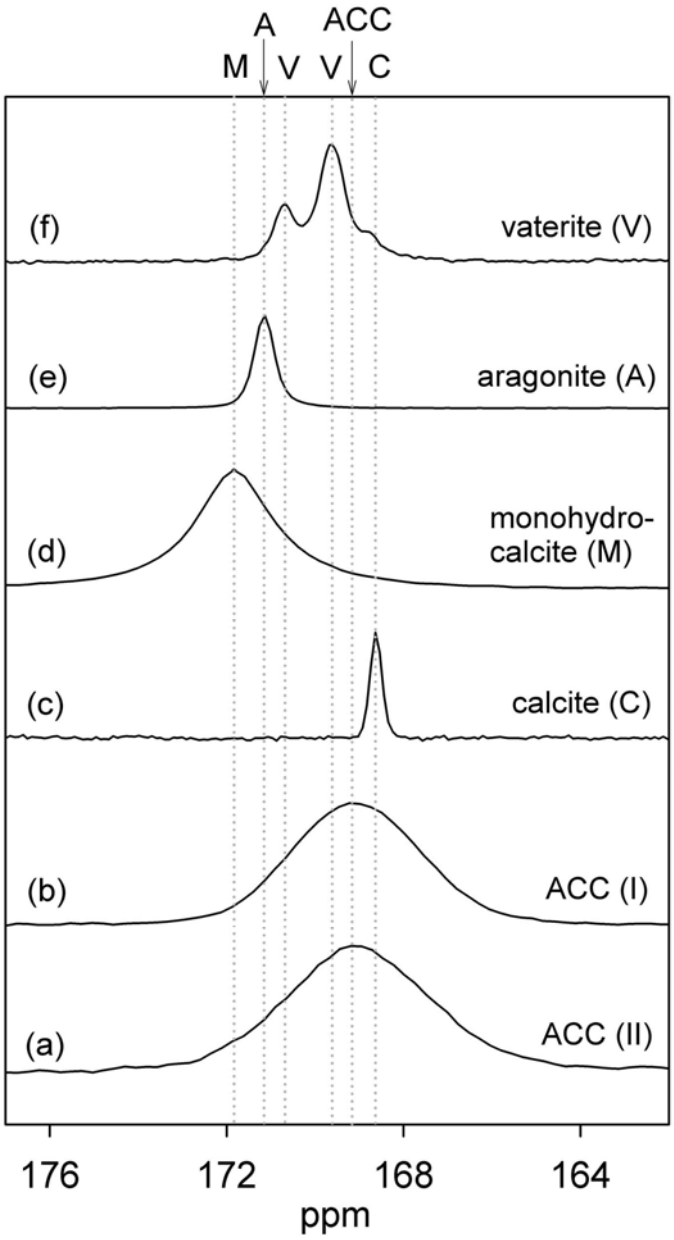

Figure 4.1 ^{13}C NMR spectra of calcium carbonate phases: (a) ACC method II (δ_C = 169 ppm), ^{13}C SP/MAS at 3 kHz spinning rate (b) ACC method I (δ_C = 169 ppm), ^{13}C SP/MAS, 3 kHz spinning rate, 1 hour acquisition delay, 2 scans (c) calcite (δ_C = 168.7 ppm), ^{13}C SP/MAS (d) monohydrocalcite (δ_C = 171.7 ppm), $^{13}C\{^1H\}$ CP/MAS (e) aragonite (δ_C = 171 ppm), ^{13}C SP/MAS (f) vaterite (δ_C = 170.7 ppm, 169.6 ppm), ^{13}C SP/MAS. Dotted lines denote the isotropic chemical shift positions of the spectra for comparison.

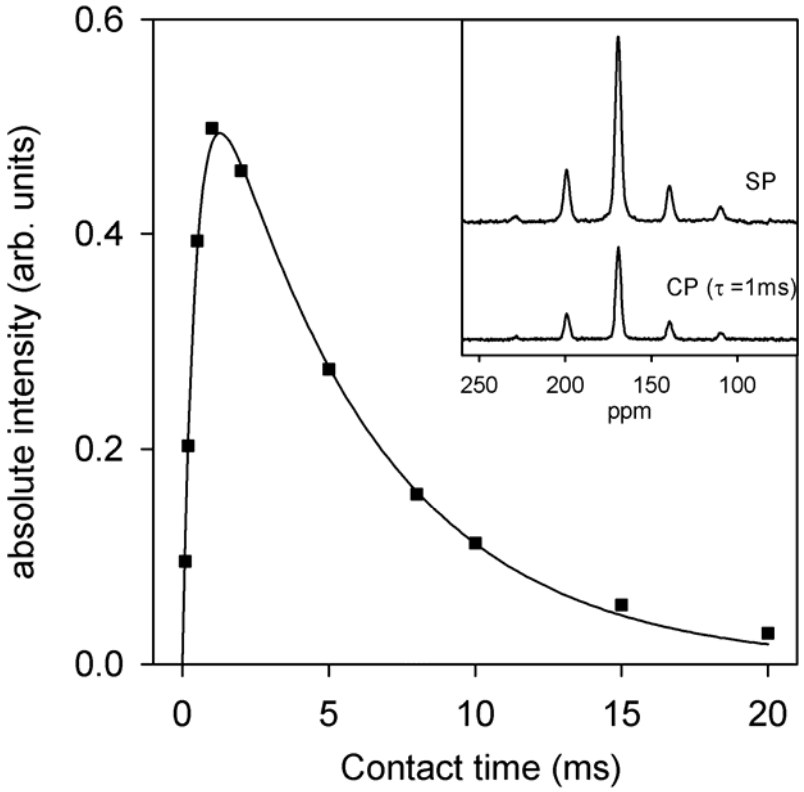

Figure 4.2 $^{13}C\{^{1}H\}$ CP kinetics data for ACC (■) and least-squares fit to classical biexponential behavior (solid line) yielding T_{CH} = 0.5 ms and $T_{1\rho,H}$ = 5.0 ms. The ordinate units indicate the theoretical ratio of signal intensity enhanced by CP/MAS experiments compared with the SP/MAS experiments. The inset shows NMR spectra in absolute intensity mode for quantitative comparison: (top) ^{13}C SP/MAS NMR spectrum, 2 scans; (bottom) $^{13}C\{^{1}H\}$ CP/MAS spectrum acquired with 1 ms contact time. Refer to experimental section for more detailed description about NMR instrumental settings.

4.3.2 $^{13}C\{^1H\}$ HETCOR NMR spectra

$^{13}C\{^1H\}$ 2-D HETCOR NMR spectra were obtained to determine the nature of H associated with carbonate in the ACC structure. Projection across the ^{13}C dimension of the 2-D contour plot (Fig. 4.3) shows only the characteristic signal of ACC (δ_C = 169 ppm, FWHH = 3.6 ppm). The ^1H slices (F1) across the ACC ^{13}C resonance from δ_C = 172 to 165 ppm are essentially identical, so that the ^1H sum projection can be used to represent the ^1H spectrum arising from hydrogens in close proximity to carbonate. Fig. 4.4a shows the ^1H sum projection (integrated from δ_C = 170.0 to 167.5 ppm) from the $^{13}C\{^1H\}$ HETCOR spectrum acquired with 1 ms contact time. This ^{13}C-detected ^1H spectrum contains at least three components, including two narrow peaks, at δ_H = 1.5 ppm and 5.3 ppm, and a broad spinning sideband (SSB) pattern centered at δ_H = 6 ppm (obtained as the average of the $n = \pm1, \pm2$ SSB positions). The narrow peak at 1.5 ppm is assigned to OH groups and the peak at 5.3 ppm likely arises from mobile molecular water [11]. The broad SSB pattern indicates the presence of quasi-isolated rigid molecular H_2O. $^{13}C\{^1H\}$ HETCOR spectra with shorter contact time (e.g., 0.2 ms) were also obtained, but the ^1H projections are very similar to that obtained at 1 ms contact time.

To quantify the different H-bearing species associated with the carbonate, $^{13}C\{^1H\}$ HETCOR NMR spectra were obtained with a mixing time (τ_{mix}) added before the $^{13}C/^1H$ contact period. During τ_{mix}, the ^1H magnetization is stored along B_0, allowing spins in different environments to exchange polarization through the ^1H-^1H homonuclear dipolar

interactions. At long mixing time, the ^{1}H magnetization reaches equilibrium, giving a quantitative and indirectly observed ^{1}H spectrum from the HETCOR experiment, with the ^{1}H intensity of each component proportional to the population of corresponding species in the dipolar coupled H network near C. The ^{1}H HETCOR sum projection acquired with τ_{mix} = 100 ms is nearly identical to that with 50 ms mixing time (Fig. 4.4b), indicating the ^{1}H polarization has equilibrated within 50 ms. Therefore, the ^{1}H signal intensities in Fig. 4.4b represent the ratio of different H-bearing species near carbonate groups in ACC. Least-squares fits to the spectrum in Fig. 4.4b show that the SSB pattern represents about 40% of the ^{1}H intensity, indicating that a significant fraction of the H-bearing species in ACC are present as rigid structural H_2O. This observation suggests that rigid H_2O, which we infer to be coordinated to Ca atoms, and the H-bonding play a crucial role for the formation and stabilization of the ACC structure. The fraction of H present as hydroxyl groups ($\sim 7 \pm 3\%$) is significant, implying the rigid OH groups might also play a role in the ACC structure. Comparison with Fig. 4.4a, for which ^{1}H spin diffusion occurred only during contact time τ_c, shows that with additional mixing time the peak at 5.3 ppm becomes dominant, representing about 55 ± 5% of the H, while the intensities of SSB pattern and the peak at 1.5 ppm decrease, implying that the ^{1}H signal at 5.3 ppm has a lower CP rate, as would be expected for H_2O molecules undergoing restricted motion. The ^{1}H single pulse MAS spectrum was also obtained for comparison (Fig. 4.4c), and shows almost the same pattern as the equilibrated ^{13}C-detected ^{1}H spectrum (Fig. 4.4b),

indicating that all the H are in dipolar contact with the ^{13}C-detected, rigid ^{1}H-bearing species. This result indicates that no significant H is present as a separate fluid phase under these conditions. No signal was observed that could be assigned to hydrogen carbonate groups in ACC. The short C-H distance of bicarbonate should result in a short T_{CH} values, however no distinct signal was significantly enhanced in CP/MAS spectra at short contact time. We have previously reported hydrogen carbonate defects in calcite, which occur near δ_H = 7.4 ppm [12], but such groups do not appear to be abundant in ACC.

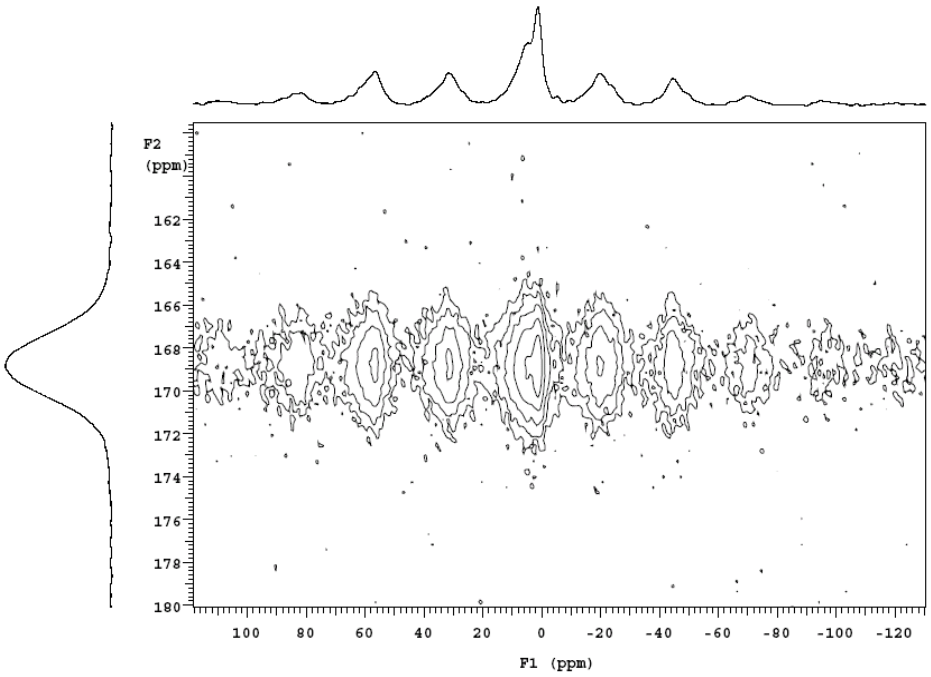

Figure 4.3 $^{13}C\{^{1}H\}$ HETCOR NMR spectrum of ACC acquired at 10 kHz spinning speed, with 1 ms contact time, 1 s acquisition delay, 100 hypercomplex points in *t*1 at an increment of 10 μs. Spectrum at left side is summed projections of the ^{13}C dimension (F2); spectrum at top is summed projections of ^{1}H dimension across the ^{13}C resonance from 170.0 to 167.5 ppm.

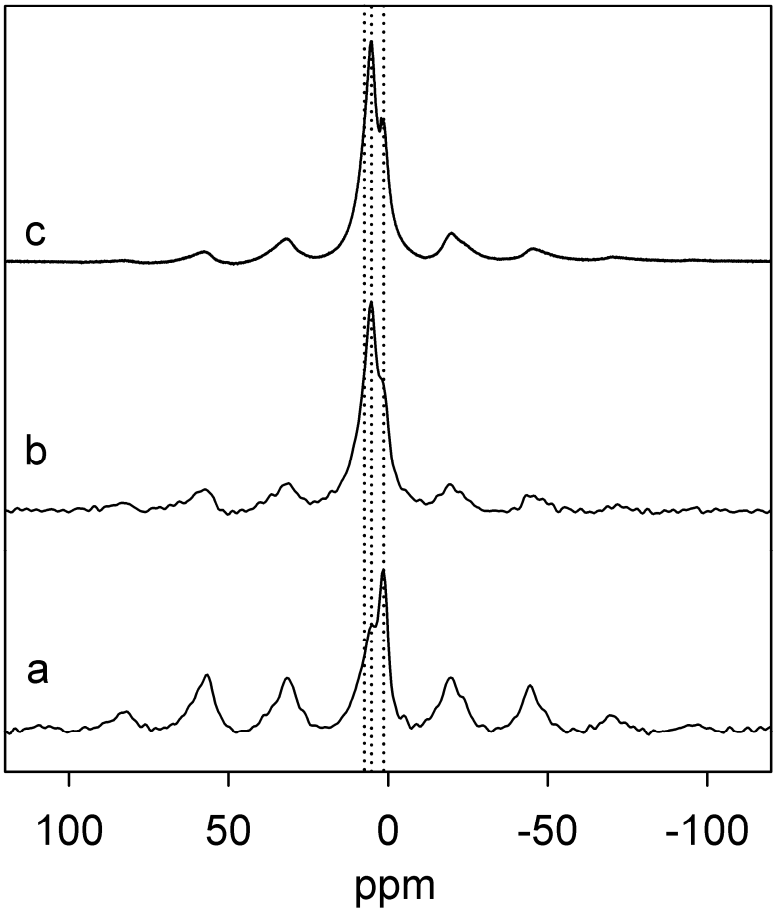

Figure 4.4 (a-b) HETCOR summed projections acquired with 1 ms contact time, 1 s acquisition delay, 100 hypercomplex points in $t1$ at an increment of 10 μs. (b) includes a 50 ms mixing time. (c) ^{1}H single pulse MAS NMR spectrum. All spectra were obtained at 10 kHz spinning rate. HETCOR spectra were summed across the ^{13}C peak from δ_C = 170.0 to 167.5 ppm, and displayed in absolute intensity mode.

4.3.3 Coordination of CO_3 units

In combination with pair distribution function (PDF) [13] analysis of total X-ray scattering, NMR results can provide constraints on the coordination of CO_3 units. The PDF is a measure of the probability of finding pairs of atoms with a separation *r*. It is obtained by Fourier transformation of the total scattering structure function *f*(Q), from scattering of high-energy X-rays [13]. This method has been widely used for studying amorphous materials, due to the advantage of incorporating both Bragg and diffuse scattering contributions. The PDF for ACC is illustrated in Fig. 4.5 (quoted from ref [14]), which also includes the calculated total PDFs for monohydroclacite and calcite and the individual pair correlations (or partials) for Ca-Ca, Ca-O, Ca-C, O-O, C-O and C-C that contribute to the total PDFs. Although a complete structural model cannot be extracted directly from the PDF, it is possible to test whether the observed pair correlations in ACC are consistent with any of the known structures in the calcium carbonate system.

From correlations of ^{1}H NMR chemical shift with hydrogen bond length (e.g., ref [11]), an average hydrogen bond length of d(O…O) = 2.87 Å can be estimated for the rigid structural water in ACC observed by NMR (δ_H = 6 ppm). This O-O distance is in good agreement with a feature near 2.9 Å in the PDF of ACC (Fig. 4.5) which does not occur in calcite, an anhydrous calcium carbonate. A similar feature is observed in the PDF of monohydrocalcite, which arises from $O_{(water)}$-$O_{(carbonate)}$ correlations, although there is also a contribution near this distance for Ca-C correlations from bidentate

carbonate configurations (Fig. 4.5). The large difference in the average ^{13}C chemical shift between ACC and the phases containing bidentate carbonate (monohydrocalcite and aragonite) suggests that most of the carbonate in ACC is monodentate. In this case, the 2.9 Å correlation should be dominated by $O_{(water)}$-$O_{(carbonate)}$ correlations, although we cannot rule out the existence of any Ca-C correlations in this range from bidentate carbonate because the large width of the ^{13}C resonance does overlap slightly the peak position for monohydrocalcite and aragonite.

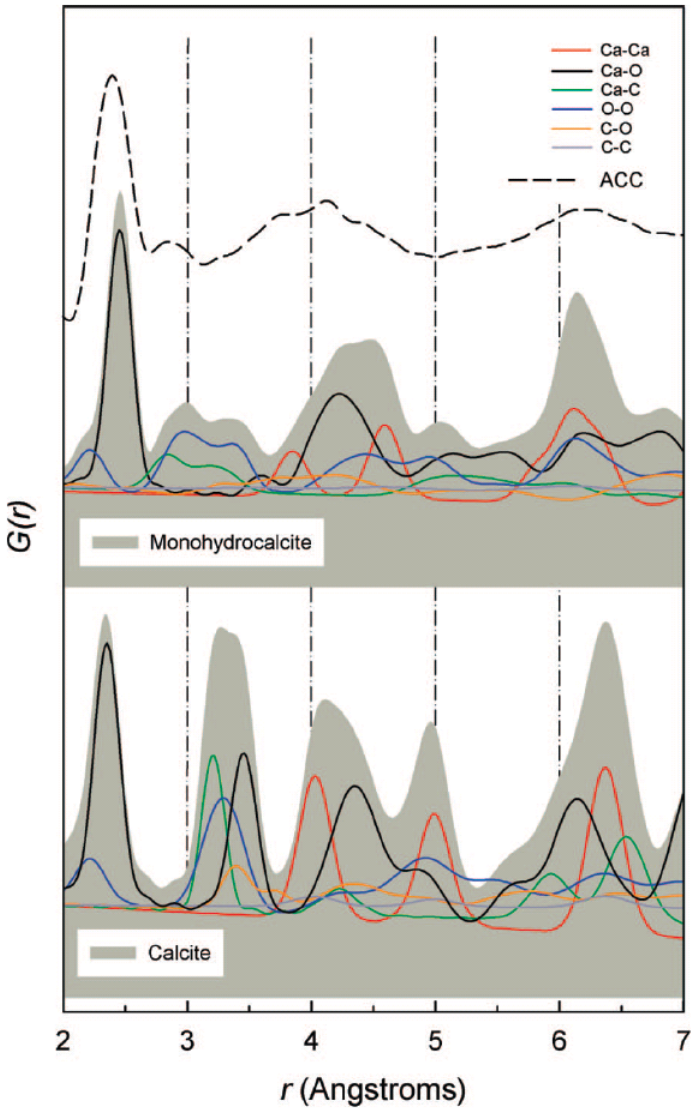

Figure 4.5 Dashed curve on top represents PDF data obtained from high-energy total X-ray scattering for ACC. Calculated total PDFs for monohydrocalcite (top gray fill) and calcite (bottom gray fill) overlain with the partial PDFs for the six pairs of atoms in each structure (colored solid curves). Correlations relating to H are not included for monohydrocalcite. This figure is quoted from ref [14].

4.3.4 NMR experiments at low temperature

NMR spectra acquired at low temperature (-120 °C) provide more direct evidence for the existence of a large amount of mobile structural H_2O in ACC. As stated in section 4.3.1, the observed ^{13}C CP/MAS signal intensity at room temperature is smaller than the ^{13}C SP/MAS intensity ($I_{0,CP}/I_{SP} \approx 1$), suggesting only around 1/4 carbonates are in proximity to rigid H. For comparison, $^{13}C\{^1H\}$ CP/MAS kinetics data were also obtained at -120 °C (Fig. 4.6), of which the least-squares fit to the classical bi-exponential equation gives $I_{0,CP}/I_{SP} \approx 2.3$, indicating a much larger fraction of carbonate carbons (> 1/2) are in dipolar contact with rigid H compared with the observation at room temperature (~ 1/4). This result is consistent with a significant reduction of H motion at low temperature. The ^1H time domain free induction decay (FID) from $^{13}C\{^1H\}$ HETCOR spectra at -120 °C (Fig. 4.7a) contains a sharper initial decay (~ 100 kHz) than that obtained at room temperature, which is caused by the stronger ^1H-^1H homonuclear dipolar coupling resulting from increased H_2O rigidity. The broad component corresponding to the initial rapid ^1H free induction decay cannot be resolved in the ^1H frequency domain (Fig. 4.7b, complete Fourier transform of HETCOR spectra), which is in contrast to the SSB pattern observed in the ^1H spectra from HETCOR obtained at room temperature. Due to the poor sensitivity of this preliminary HETCOR experiment (Fig. 4.7b), it is not clear whether the signal near 0 ppm arises from OH group or from H_2O with some restricted mobility remaining at -120 °C. More HETCOR experiments at low

temperature with better sensitivity and with a mixing time are needed to investigate fully whether the CP intensity loss compared to the theoretical ($I_{0,CP}/I_{SP} \approx 2.3$ vs. 4) is caused only by H_2O motion remaining at -120°C or whether there also exists structural non-uniformity manifested in long C-H distances for some carbonate groups.

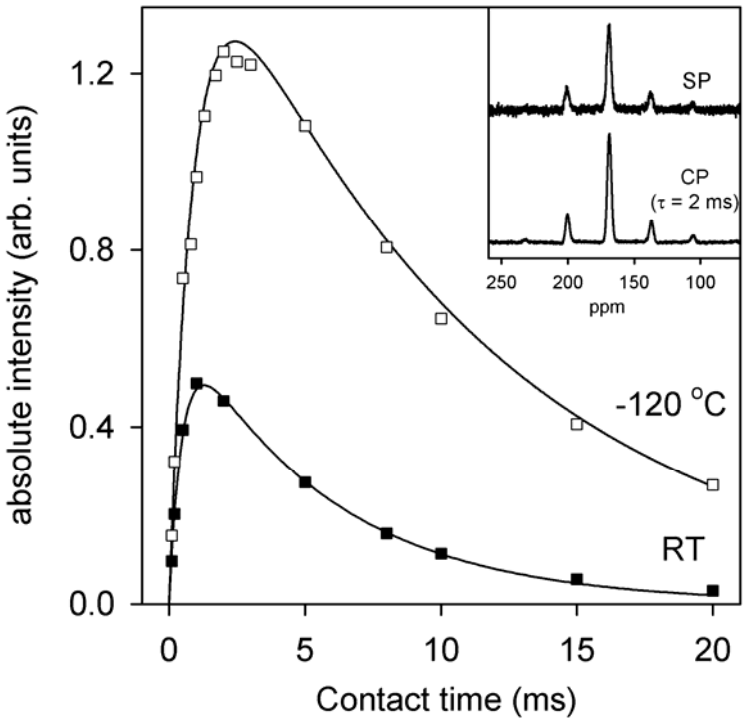

Figure 4.6 $^{13}C\{^{1}H\}$ CP kinetics data for ACC acquired at -120 °C (□) and least-squares fit to classical biexponential behavior (solid line) yielding T_{CH} = 0.9 ms and $T_{1\rho,H}$ = 10.6 ms. The ordinate units indicate the ratio of signal intensity from CP/MAS experiments to that from SP/MAS experiments. Results obtained at RT (■) are shown for comparison. The inset shows NMR spectra at -120 °C in absolute intensity mode for quantitative comparison: (top) ^{13}C SP/MAS NMR spectrum, 2 scans; (bottom) $^{13}C\{^{1}H\}$ CP/MAS spectrum acquired with 2 ms contact time and totally 200 scans. Refer to experimental section for more detailed description about NMR instrumental settings.

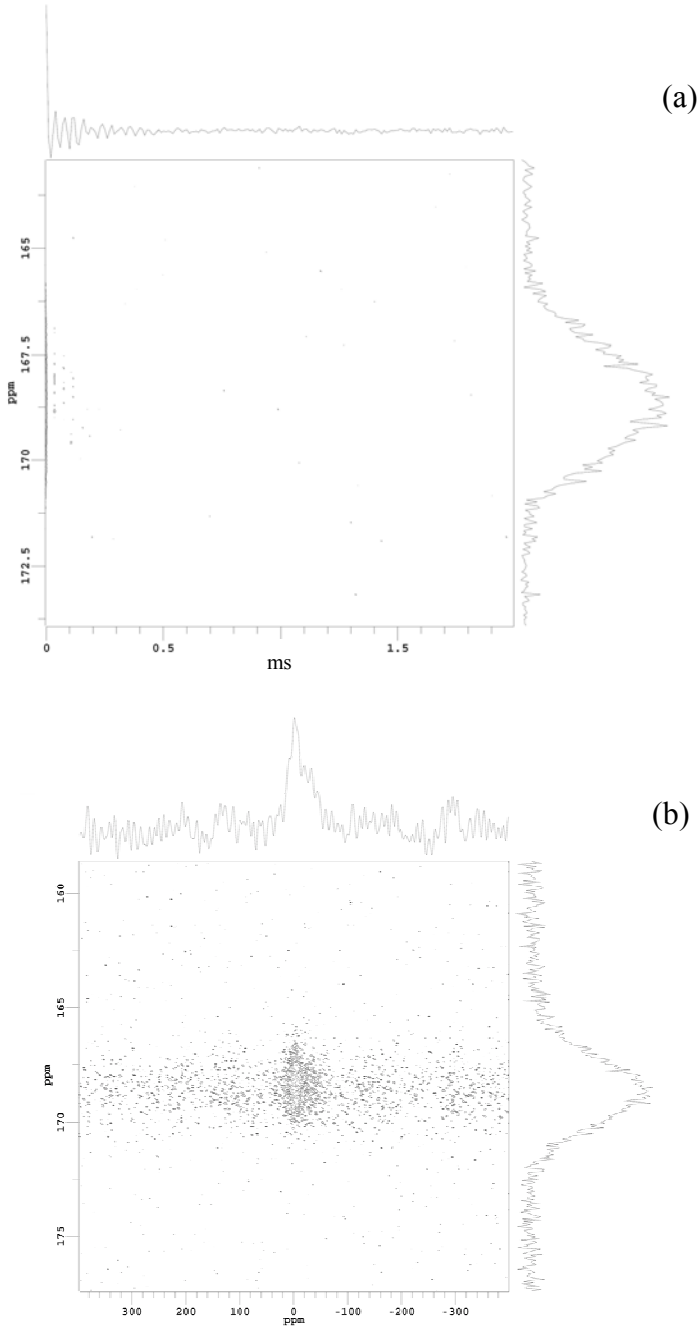

Figure 4.7 $^{13}C\{^{1}H\}$ HETCOR NMR data obtained at -120 °C, with 8 kHz spinning rate, 2 ms contact time, 1 s acquisition delay, 100 hypercomplex points in $t1$ at an increment of 5 μs. (a) Only the ^{13}C dimension is Fourier-transformed to the frequency domain and the abscissa represents the ^{1}H time domain FID. (b) Both ^{1}H and ^{13}C dimensions are displayed in frequency domain.

4.3.5 Stability and transformation of synthetic additive-free ACC

NMR data obtained at various times after synthesis indicate that the stability of the synthetic additive-free ACC strongly depends on the ambient humidity. The sample which was dried in vacuum for 30 min before sealing the rotor was stable for at least 8 days. It can be seen from Fig. 4.8 that the peak width and intensity of the ACC ^{13}C NMR signal acquired after 8 days (Fig. 4.8b) are the same as that acquired within 2 hours after synthesis (Fig. 4.8a), for both the ^{13}C SP/MAS and the $^{13}C\{^{1}H\}$ CP/MAS spectra. In contrast, samples which were directly loaded into a rotor without being dried tend to transform quickly to other crystalline phases which are readily detected in the ^{13}C SP/MAS spectra. Figure 4.9 shows ^{13}C SP/MAS NMR spectra and the corresponding peak fits (dashed lines) obtained at different storage time after sample preparation. During the interval between NMR acquisitions, the sample was stored in the rotor, but with the plug removed, exposing the sample exposing to air. The spectrum in Fig. 4.9a was acquired 2 hours after the ACC was prepared, and contains only the characteristic ACC signal (δ_{iso} = 169 ppm, fwhh = 3.6 ppm). Fig. 4.9(b-e) shows the ^{13}C SP/MAS spectra (solid line) and the corresponding components from least-squares fits (dashed line) obtained respectively at 10, 24, 52 and 230 hours after preparation. Each spectrum was acquired with 1 hour relaxation time and 1 or 2 scans. It can be seen from these ^{13}C SP/MAS spectra that the initially pure ACC phase gradually transformed to primarily calcite (δ_C = 168.7 ppm) plus a small amount of aragonite (δ_C = 171.0 ppm). Nonetheless,

around 20% of the ACC remains in the sample after 230 hours (Fig. 4.9e). The variation of the fraction of ACC in the sample with storage time is plotted in Fig. 4.10. During the transformation, no significant change is observed for the peak position for ACC. However, the ^{13}C line width for the ACC resonance gradually narrows, from 3.6 ppm (fwhh, Fig. 4.9a) to 1.5 ppm (fwhh, Fig. 4.9(b-e)), implying some kind of ordering process occurs, or that some portions of the ACC structure crystallize more readily than others. These results indicate that the ^{13}C NMR can be used to quantitatively characterize the crystallization kinietics of ACC.

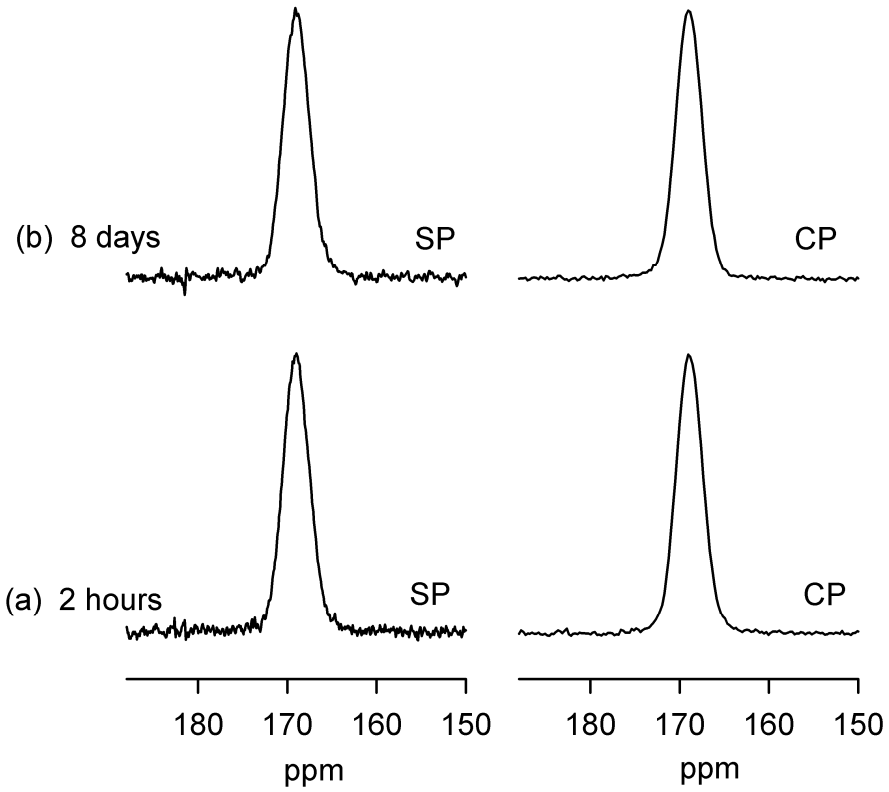

Figure 4.8 ^{13}C SP/MAS (left) and $^{13}C\{^{1}H\}$ CP/MAS (right) NMR spectra (in absolute intensity mode) of ACC (method I) which was dried in vacuum before sealing the rotor. (a) Spectra acquired after 2 hours. (b) Spectra acquired after 8 days. ^{13}C SP/MAS NMR spectra were obtained with 10 kHz spinning rate, 30 min acquisition delay and 4 scans. $^{13}C\{^{1}H\}$ CP/MAS NMR spectra were obtained with 10 kHz spinning rate, 1 ms contact time, 1 s ^{1}H acquisition delay and 100 scans.

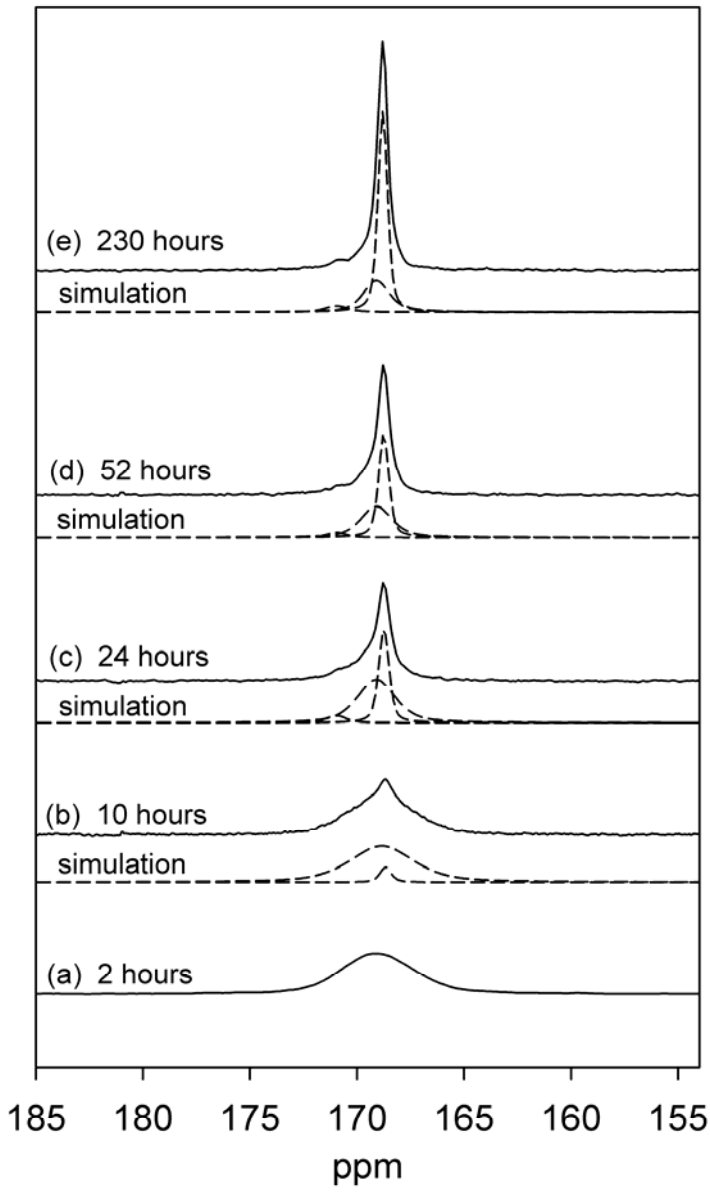

Figure 4.9 ^{13}C single pulse MAS NMR spectra (in absolute intensity mode) obtained at different times after synthesis: (a) 2 hours (b) 10 hours (c) 24 hours (d) 52 hours (e) 230 hours. NMR experimental conditions are 3 kHz spinning rate, 1 hour acquisition delay for a total of 1 scan (b-e) or 2 scans (a). The sample was stored in air between NMR experiments. Dashed lines in (b-e) represent the components of least-squares fits of the spectra to a minimum number of symmetrical curves, all of which contain three components, corresponding to: ACC, calcite and aragonite.

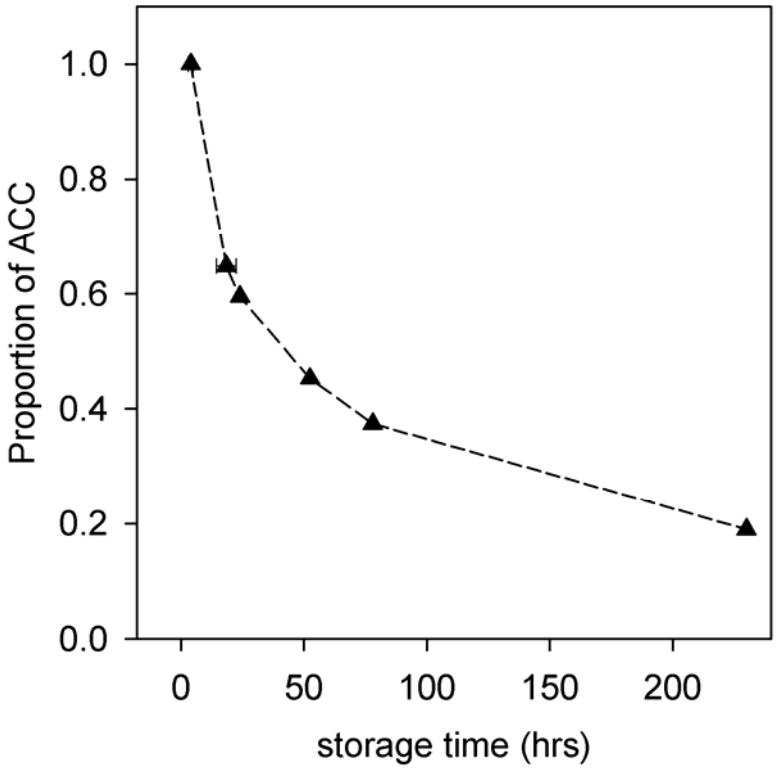

Figure 4.10 Fraction of ^{13}C SP/MAS intensity assigned to ACC in the sample, measured at different storage times. The sample was stored with exposure to air between the NMR acquisitions. The dashed line is merely used to connect experimental points.

4.4 Conclusion

The NMR results indicate that most of the hydrogen in ACC is present as structural molecular water and that an additional fraction of rigid OH groups (～7 ± 3%) might also play a role in the ACC structure. However, over one-half of this structural water exhibits restricted motion on the millisecond time scale which could play a role in the instability of ACC by enhancing transport of Ca and possibly carbonate. These hydrous components are almost certainly coordinated to Ca atoms. Therefore, Ca atoms in the synthetic ACC could be variably coordinated by CO_3, H_2O, and possibly OH groups. Comparison of the X-ray generated PDFs and NMR spectra for ACC to those of monohydrocalcite indicates that these phases have distinct differences in terms of the distribution of interatomic distances as well as the configuration of carbonate which is predominantly monodentate in ACC versus bidentate in monohydrocalcite. These observations confirm that synthetic ACC is not simply a nanocrystalline or disordered form of monohydrocalcite.

In addition, these results show that NMR is a potentially useful tool for real-time study of the transformation of ACC. The chemical shift positions and line widths of ^{13}C resonances can be used as fingerprints for distinguishing various calcium carbonate phases. Since one of the aims for studying ACC is to understand the dominant factors that direct the assembly and that govern the selection of the final crystalline polymorph, it is necessary to have an efficient characterization method for monitoring the transformation

of ACC in situ. In the current work, the ^{13}C SP/MAS NMR spectra prove to be effective for such a role. Although the experimental conditions, such as temperature and humidity, were not strictly controlled, this could easily be achieved through slight modification of the experimental design if the transformation is slow compared to the time required for acquisition of the NMR spectrum.

4.5 References

1. Mann S. *Biomineralization: principles and concepts in bioinorganic materials chemistry*. Oxford University Press: New York, 2001, xii, 198 p.
2. Lowenstam HA, Weiner S. *On biomineralization*. Oxford University Press: New York, 1989, ix, 324 p.
3. Aizenberg J, Muller DA, Grazul JL, Hamann DR, *Science*, 2003, **299**: 1205-1208.
4. Dujardin E, Mann S, *Adv. Mater.*, 2002, **14**: 775-788.
5. Addadi L, Raz S, Weiner S, *Adv. Mater.*, 2003, **15**: 959-970.
6. Koga N, Nakagoe YZ, Tanaka H, *Thermochim. Acta*, 1998, **318**: 239-244.
7. Faatz M, Grohn F, Wegner G, *Adv. Mater.*, 2004, **16**: 996-1000.
8. Schmidtrohr K, Clauss J, Spiess HW, *Macromolecules*, 1992, **25**: 3273-3277.
9. Mehring M. *Principles of high-resolution NMR in solids*. Springer-Verlag: Berlin, New York, 1983.
10. Kolodziejski W, Klinowski J, *Chem. Rev.*, 2002, **102**: 613-628.
11. Yesinowski JP, Eckert H, Rossman GR, *J. Am. Chem. Soc.*, 1988, **110**: 1367-1375.
12. Feng J, Lee YJ, Reeder RJ, Phillips BL, *Am. Mineral.*, 2006, **91**: 957-960.
13. Egami T, Billinge SJL. *Underneath the Bragg peaks : structural analysis of complex materials*. Pergamon: Kiddington, Oxford, UK ; Boston, 2003, xviii, 404 p.

14. Michel FM, MacDonald J, Feng J, Phillips BL, Ehm L, Tarabrella C, Parise JB, Reeder RJ, *Chem. Mater.*, 2008, **20**: 4720-4728.

Chapter 5

Amorphous calcium carbonate and hydrated defects in synthetic aragonite detected by solid-state NMR

5.1 Introduction

Aragonite is one of the most common biogenic mineral phases, particularly as endo- or exo-skeletons in a variety of mollusks [1,2]. Although aragonite is the thermodynamically stable $CaCO_3$ polymorph only at elevated pressure [3,4], organisms can produce aragonite with controlled shape and size under ambient conditions [5]. Many biological materials exhibit delicate structures and unique mechanical properties [6], which has prompted a research effort in this field during the last several decades [1,6]. For example, one of the intensively investigated systems containing aragonite is nacre [7-13], which is composed of layered single crystalline aragonite platelets separated by organic matrix sheets with a sandwich-like structure of a β-chitin core between insoluble protein layers [1,14]. This mesoscopic composite material resembles a brick-and-mortar construct and exhibits a fracture resistance 3000-fold enhanced compared with pure inorganic aragonite [12,13]. When studying the structure of biomineralized materials, electron microscopy plays an important role in elucidating the hierarchical order of the mineral/organic composites, providing information on how the organic matrices control the orientated nucleation and growth of crystals [15]. However, more direct information at the molecular level is needed to fully understand the nature of mineral/organic-matrix interfacial interactions which can eventually inspire new ideas for materials and then synthesis [16].

Complementary to electron microscopy and X-ray scattering or absorption techniques, NMR spectroscopy is a potentially useful tool for studying the molecular interactions at the mineral/organic interface, due to its sensitivity to the relevant light elements (i.e., ^{1}H, ^{13}C, ^{15}N, etc.) and short range structures. Double resonance NMR

methods based on through-space dipole-dipole interactions, such as cross-polarization magic-angle-spinning (CP/MAS) [17-20], heteronuclear correlation (HECTOR) [21,22], rotational echo double resonance (REDOR) [23], transfer of population in double resonance (TRAPDOR) [24,25] and rotational-echo adiabatic-passage double resonance (REAPDOR) [26] etc., can be used to probe the spatial proximities between molecules, such as the organic matrix and mineral phase in biominerals. Several studies on nacre samples have utilized CP/MAS and HETCOR NMR to probe the mineral/organic relationship and infer structural information. For example, Takahashi et al. found that the ^{13}C signals arising from carbonate groups in $^{13}C\{^{1}H\}$ CP/MAS spectra of oyster nacre show significant intensities even at short contact time, and attributed the H source to the nearby biopolymer [11]. Combined with the observations from field emission transmission electron microscopy (FE/TEM) images, they suggested that the aragonite in nacre is composed of highly ordered nanocrystals aligned somehow by the biopolymers, instead of being merely a single crystal. Nassif et al. [12] and Jäger et al. [13] assigned the $^{13}C\{^{1}H\}$ CP/MAS signals obtained for nacre at long contact time to the amorphous calcium carbonate (ACC) phase located between the aragonite and the organic matrix, which challenges the traditional explanations of the existence of an epitaxial match for the mineral/organic interfacial structure [12]. Here, we report results for a purely inorganic synthetic aragonite and find that the $^{13}C\{^{1}H\}$ CP/MAS spectra contain signals arising from intrinsic H-bearing defects and a separate amorphous calcium carbonate phase. In particular, the line shapes of peaks in $^{13}C\{^{1}H\}$ CP/MAS spectra of synthetic aragonite closely resemble those observed by Nassif et al. [12] and Jäger [13] for nacre samples, indicating that the contributions from the bulk intrinsic defects within the

mineral phase should be taken into account when interpreting the NMR results for natural biogenic samples.

5.2 Experimental

5.2.1 Materials

Previous studies (e.g., [27,28]) have shown that the addition of Mg^{2+} can inhibit calcite growth and therefore promote precipitation of aragonite. Therefore our synthesis of aragonite followed the modified constant-addition method for calcite synthesis adapted from Zhong and Mucci [29] and Tesoriero and Pankow [30], and described in refs. [31] and [32], except with high Mg^{2+} concentration. A stirred reaction vessel containing 7 mM $NaHCO_3$, 7 mM $CaCl_2$, 50 mM $MgCl_2$ and 0.1 M NaCl (background electrolyte) was bubbled continuously with water-saturated air. Two separate solutions containing 0.1 M $CaCl_2$ and 0.1 M Na_2CO_3, each with 0.1 M NaCl background electrolyte, were pumped through syringes into the reaction vessel at a constant rate. The initial pH of the solution in the reaction vessel was ~7.8. The total reaction time was 8 hrs. The solution pH increased initially and reached a constant value of 8.3 ± 0.1 within 2 to 3 h. Total CO_2 content in the solution was measured using the procedure described in ref. [33]. The amount of total dissolved CO_2 dropped initially and reached a constant value after approximately 5 hrs, corresponding to near steady-state conditions. The final aragonite powder was collected by vacuum filtration, washed multiple times with deionized water, and dried in an oven at 50 ºC. Two different samples were synthesized. Sample CAM-A3 used ^{13}C-enriched $NaCO_3$ in the anion syringe, resulting in a ^{13}C-enriched aragonite.

Using the program PHREEQC [34], the saturation index values (expressed as log (IAP/Keq)) are oversaturated with respect to several solid phases, with aragonite 1.15,

calcite 1.33, dolomite 3.60 and magnesite 1.18. However, X-ray diffraction (XRD) detected no phases other than well-crystalline aragonite.

5.2.2 NMR spectroscopy

Most solid-state NMR spectra were collected on a 400 MHz (9.4 T) Varian Inova spectrometer operating at 100.6 MHz for ^{13}C and 399.76 MHz for ^{1}H. The $^{13}C\{^{1}H\}$ CP kinetics were measured with a Varian/Chemagnetics 'T3' probe assembly configured for 7.5 mm (outer diameter) rotors. The experimental conditions for measuring $^{13}C\{^{1}H\}$ CP/MAS kenitics were 5 kHz spinning rate, 8 μs 90° ^{1}H excitation pulse and 1 second acquisition delay. The spin-locking (CW mode) powers are set to 32 kHz for the ^{1}H channel and 27 kHz for the ^{13}C channel during the CP contact time, corresponding to the 1st side band match condition. The chemical shift anisotropy (CSA) for resonances in $^{13}C\{^{1}H\}$ CP/MAS spectra were determined from analysis of spinning sideband intensities obtained at a spinning rate of 1.2 kHz using the HBA program [35]. For comparison, the CSA was similarly determined for the signals in ^{13}C single pulse magic angle spinning spectra (SP/MAS) obtained at 1.2 kHz, with 8 μs 90° ^{13}C excitation pulse and 1 h acquisition delay due to the long ^{13}C spin-lattice relaxation time. $^{13}C\{^{1}H\}$ 2-dimensional HETeronuclear CORrelation (HETCOR) NMR spectra [21,22] were obtained using a Varian/Chemagnetics 'T3' probe assembly configured for 3.2 mm (outer diameter) thin wall rotors. The ^{1}H-coupled HETCOR spectra were acquired at 10 kHz spinning rate with 1 s acquisition delays, a linear ramp of ^{13}C B_1 field during contact time and high-power ^{1}H decoupling during t_2, but with no homonuclear ^{1}H decoupling applied during t1.

5.3 Results and Discussion

5.3.1 ^{13}C NMR experiments

The ^{13}C single pulse NMR spectrum of aragonite contains a broad spinning sideband manifold with a single, narrow (0.5 ppm full-width at half-maximum; fwhm) centerband at a chemical shift of 171.0 ppm (Fig. 5.1a), consistent with the crystallographic structure [36-38] and previously reported ^{13}C single pulse NMR spectra [12,13,39]. In comparison, the ^{13}C{^{1}H} CP/MAS spectra (Fig. 5.1b) contain partially resolved signals arising from carbonate carbons near rigid H-bearing species, which can be fit as three components (Fig. 5.2) with chemical shifts of 171.1 ppm (1.1 ppm fwhm), 170.1 ppm (1.6 ppm fwhm) and 169.0 ppm (3.5 ppm fwhm). The multiple peaks and the large peak widths in ^{13}Cs CP/MAS spectra indicate that the H-bearing defects or impurity phases in the synthetic aragonite have a range of structural configurations. The peak at 169.0 ppm in the ^{13}C{^{1}H} CP/MAS spectra has the same chemical shift and linewidth within experimental uncertainty (± 0.1 ppm) as that reported previously for synthetic amorphous calcium carbonate (ACC) [40], and on this basis can be assigned to residual ACC in the sample. The two other resonances in ^{13}C{^{1}H} CP/MAS spectra, at 171.1 and 170.1 ppm, do not correspond to any reported hydrated $CaCO_3$ phases in the sense of both chemical shift values and line widths [40,41], so likely arise from C near the intrinsic H-bearing defects in the aragonite bulk. A similar observation was found for nominally anhydrous calcite precipitated from aqueous solution, in which the concentration of hydrogen carbonate defects is sufficient to yield easily detected ^{13}C{^{1}H} CP/MAS signals [42]. It has been suggested, from the NMR study of various calcium carbonate phases, that ^{13}C chemical

shift values of carbonates can be correlated to the coordination mode between Ca^{2+} ion and CO_3^{2-} group (i.e., monodentate vs. bidentate) [40]. Accordingly, the signal at 171.1 ppm can be assigned to bidentate carbonate groups, essentially similar to those of bulk aragonite, while the signal at 170.1 ppm arises from those carbonates with coordination configurations between fully monodentate and bidentate. Nassif et al. [12] and Jäger [13] observed similar $^{13}C\{^1H\}$ CP/MAS spectra from nacre, a biomineral composed of aragonite platelets covered by β-chitin layer [1], although the total peak span of centerbands (~ 5.5 ppm) is slightly narrower than that obtained in current work (~ 6.5 ppm), which is attributed to the difference in ^1H decoupling strengths and methods (TPPM vs. CW). However, in these studies, the CP/MAS signal is described as a single resonance instead of multiple distinct overlapping components, and the entire asymmetric peak is assigned to an amorphous calcium carbonate phase. This interpretation contradicts the ^{13}C NMR spectra for synthetic additive-free ACC previously obtained by both Michel et al. [40] and Nebel et al. [41], which contain only a single broad symmetrical centerband.

Comparison of the ^{13}C chemical shift anisotropy (CSA) for the three resonances in $^{13}C\{^1H\}$ CP/MAS spectra with that for carbonate in well-ordered bulk crystal, obtained from ^{13}C single pulse spectra, suggests the existence of residual ACC and absence of a significant population of hydrogen carbonate groups near hydrated defects. Allowing all the parameters to vary freely, a least-squares fit of the spinning sideband intensities in the single pulse spectrum gives a CSA of δ_{11} = 205.2, δ_{22} = 192.0, δ_{33} = 116.1 ppm for bulk crystalline aragonite. These values are consistent with the reported crystallographic data, where the unequal C-O bond lengths break the axial symmetry at the C-position, resulting

in a small splitting of δ_{11} and δ_{22} values. In the same way, CSA values were obtained for the signals in CP/MAS spectra, including those for the peak at 171.1 ppm (δ_{11} = 207.0, δ_{22} = 189.6, δ_{33} = 116.5 ppm, $\bar{\sigma}$ = 0.5 ppm), the peak at 170.1 ppm (δ_{11} = 207.4, δ_{22} = 187.5, δ_{33} = 115.2 ppm, $\bar{\sigma}$ = 0.8 ppm) and the peak at 169.0 ppm (δ_{11} = 207.6, δ_{22} = 177.0, δ_{33} = 122.4 ppm, $\bar{\sigma}$ = 1.9 ppm). Estimated uncertainties in the principal CSA values ($\bar{\sigma}$) were obtained by a Monte Carlo method, from fitting several sets of SSB intensities generated by modulating the best-fit values by an amount consistent with a random distribution of estimated errors. The CSA for the resonance at 169.0 ppm is consistent with that previously determined for synthetic ACC (δ_{11} = 207.7, δ_{22} = 180.9, δ_{33} = 118.4 ppm), supporting the assignment of this signal to residual ACC in the aragonite sample.

Previous study by Gu and McDermott [43,44] on the magnetic shielding of carbon in carboxyl groups of amino acids suggested that the CSA can be used to distinguish the protonation states of carboxyl groups. An asymmetry function *A*, defined as $A = \delta_{11} - \delta_{22} + \delta_{33}$, was found to change most significantly upon protonation. Although the asymmetry parameter *A* itself varies over a broad range among different deprotonated amino acids, the change of *A* upon protonation is almost constant (ca. 40 ppm) for all the amino acids studied, indicating that the effect of protonation on the carboxyl electronic structure is relatively independent of the side chains. A similar change of carbon chemical shielding upon protonation was also observed for carbonate groups in calcite, where the asymmetry function for bicarbonate defects (*A* = 138 ppm) is larger than that for bulk carbonate groups (*A* = 120.5 ppm) by ~18 ppm. These experimental results suggest that protonation of both carboxyl and carbonate groups can induce further split of δ_{11} and δ_{22} in O-C-O

plane, resulting in a distinct increase in values of the asymmetry parameter *A*. For the carbonate groups near H-bearing defects of concern here, the asymmetry functions for the resonances at 171.1 ppm (*A* = 134 ppm) and 170.1 ppm (*A* = 135.2 ppm) in $^{13}C\{^{1}H\}$ CP/MAS spectra differ only slightly from that for well-ordered carbonate groups in aragonite bulk as observed in ^{13}C single pulse spectra (A = 129.3 ppm), indicating non-protonated defect carbonate groups. This apparent absence of significant amounts of protonated carbonate in aragonite is in contrast to similarly prepared synthetic calcite [42], in which all of the CP signal appears to arise from hydrogen carbonate defects.

Quantitative study of CP kinetics provides additional evidence for the assignment of resonances in $^{13}C\{^{1}H\}$ CP/MAS spectra. Variations of signal intensities with experimental CP contact time (τ_c) for each of the three peaks in CP/MAS spectra can be fit to the classical biexponential equation [19,20] (shown in Fig. 5.3), resulting in T_{CH}, the CP time constant for ^{13}C-^{1}H polarization transfer, and $T_{1\rho,H}$, the ^{1}H relaxation time in the rotating frame. Best-fit values are T_{CH} = 0.70 ms, $T_{1\rho,H}$ = 65 ms for the peak at 171.1 ppm, T_{CH} = 0.53 ms, $T_{1\rho,H}$ = 9.1 ms for the peak at 170.1 ppm, and T_{CH} = 0.43 ms, $T_{1\rho,H}$ = 8.8 ms for the peak at 169.0 ppm. The large difference of ^{1}H $T_{1,\rho}$ between the peak at 171.1 ppm and the other two resonances clearly indicates that the asymmetric line shape in $^{13}C\{^{1}H\}$ CP/MAS spectra arises from carbonate groups with distinct chemical environments, instead of a quasi-continuous distribution or a single amorphous phase. T_{CH} and $T_{1\rho}$ for the peak at 169.0 ppm are reasonably consistent with those previously measured for synthetic additive-free ACC [40], considering the uncertainty of peak intensities from fitting poorly resolved peaks. For these CP kinetics experiments, the aragonite sample was spun at 5 kHz, higher than that set previously for synthetic ACC (3

kHz) [40]. However, this difference in spinning rate should not change the CP kinetics of ACC significantly, due to the strong ^{1}H-^{1}H homonuclear dipolar coupling and the resulted broad match curve (~ 20 kHz fwhm). The relative populations for the three ^{13}C signals can also be estimated from the parameter $I_{0,CP}$ in the CP kinetics bi-exponential equation, which is proportional to the number of ^{13}C spins which are in dipolar contact to ^{1}H. The resulted ratio of $I_{0,CP}$ for the three resonances at 171.1, 170.1 and 169.0 ppm is about 0.9 : 1.3 :1, indicating the populations corresponding to each C environment are in the same quantitative level. Comparison of the intensity of CP to that of SP shows that the total content of hydrated defects and ACC residue in the aragonite sample is around 1.5 mol. %, consistent with the estimate by Jäger [13] for the natural nacre sample.

No periodic oscillations are observed in ^{13}C{^{1}H} CP kinetics for any of the three resonances, implying the absence of significant amounts of isolated C-H spin pairs, and that the carbonate carbon near H-bearing defect is in dipolar contact to multiple protons. For classical CP kinetics, a correlation has been established [45] between CP time constant T_{CH} and heteronuclear dipolar second moment M_2^{CH}, which is determined by C-H distances. According to this $T_{CH} \sim M_2^{CH}$ correlation, coordination of H-containing species to carbonate groups through a single moderate H-bond (e.g., $d(C\text{-}O\cdots H)$ = 1.5 Å) yields T_{CH} in the range of 1.4 to 2.1 ms, depending on the effective ^{1}H-^{1}H homonuclear dipolar coupling strength. These estimates should be valid for H-bearing carbonate defects in aragonite, since the CP match curves for each of the three ^{13}C resonances show broad patterns, comparable to that for citrate sample, indicating the homonuclear dipolar coupling for the hydrated defects fall in the range considered by the correlation curves [45]. Therefore, the measured T_{IS} for resonances at 171.1 and 170.1 ppm in ^{13}C{^{1}H}

CP/MAS spectra (0.7 and 0.53 ms respectively) appear to correspond to non-protonated carbonate groups interacting with more than one H.

On the other hand, an intermediate ratio of $N_{C\text{-}13}/N_{H\text{-}1}$ can also affect the measured T_{CH} and $T_{I\rho,H}$. The CP parameters (T_{CH} and $T_{I\rho,H}$) obtained by fitting the classical bi-exponential equation are indeed apparent values for systems with non-negligible $N_{C\text{-}13}/N_{H\text{-}1}$. For infinitely large $T_{I\rho,H}$, the measured T_{CH} should be multiplied by a factor of (1 + $N_{C\text{-}13}/N_{H\text{-}1}$) to yield the real values, as was done previously for studying a synthetic calcite/citrate composite [45]. For finite $T_{I\rho,H}$, the real T_{CH} and $T_{I\rho,H}$ can be obtained by solving a more complicated set of equations according to the full CP kinetics equation [19,20]. Assuming $N_{C\text{-}13}/N_{H\text{-}1}$ = 1/4 for defects in the aragonite, the corrected values for $^{13}C\{^{1}H\}$ CP kinetics are T_{CH} = 0.88 ms, $T_{I\rho,H}$ = 51.8 ms for the peak at 171.1 ppm, and T_{CH} = 0.67 ms, $T_{I\rho,H}$ = 7.2 ms for the peak at 170.1 ppm. This is supported by $T_{I\rho,H}$ values (45.2 ms and 5.9 ms for the peaks at 171.1 ppm and 170.1 ppm respectively) obtained indirectly using a ^{13}C-observed CP sequence [20], where a constant CP time is added after the ^{1}H spin-locking time so that the $T_{I\rho,H}$ can be measured for each resonance in the $^{13}C\{^{1}H\}$ CP/MAS spectrum. So, the real T_{CH} values are larger than those obtained directly from fitting the bi-exponential equation, and can be reasonably interpreted as arising from two H-bonds.

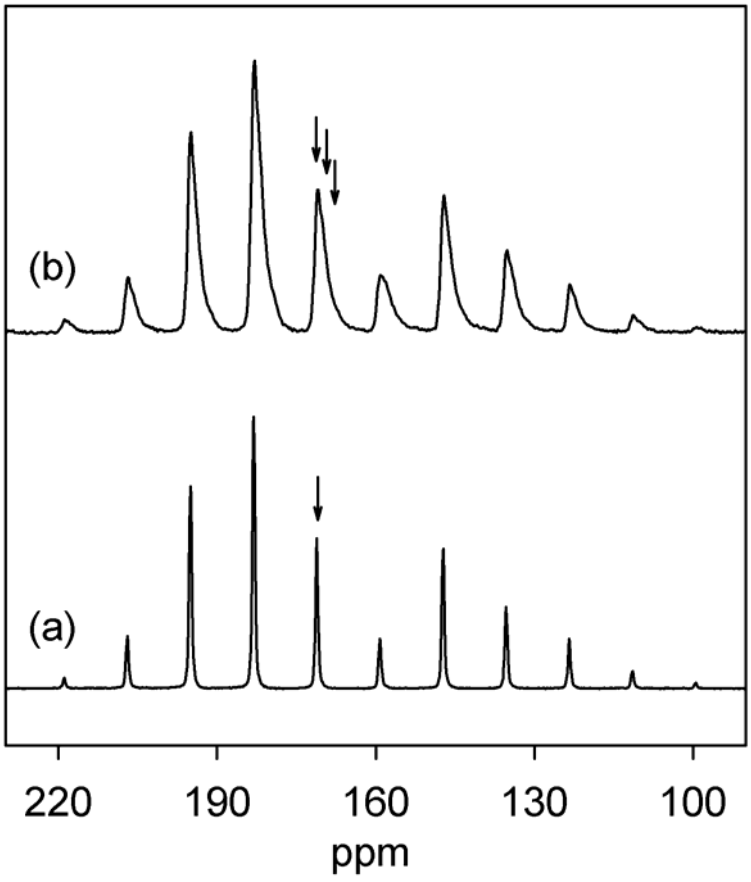

Figure 5.1 ^{13}C MAS NMR spectra of synthetic ^{13}C-enriched aragonite acquired at 1.2 kHz spinning rate. (a) Single pulse spectrum, 1 acquisition with 3600 s relaxation delay. (b) $^{13}C\{^{1}H\}$ CP/MAS spectrum obtained with 5 ms contact time. Arrows denote the center bands; all other peaks are spinning sidebands.

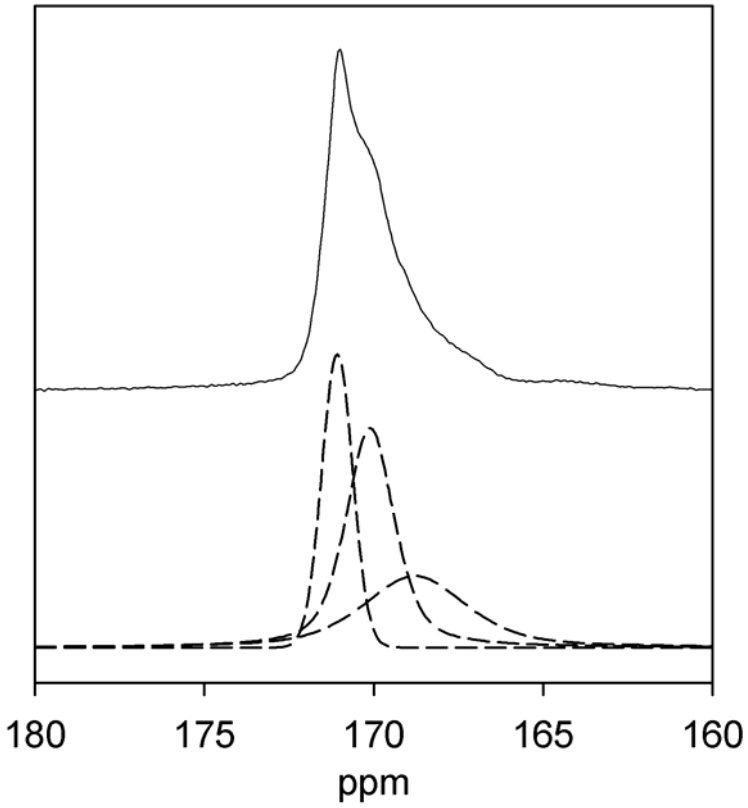

Figure 5.2 (Top, solid line) $^{13}C\{^{1}H\}$ CP/MAS NMR spectra of synthetic ^{13}C-enriched aragonite acquired at 5 kHz spinning rate and 5 ms contact time. Only center bands are shown to improve the clarity. (Bottom, dashed lines) Components of a least-squares fit of the CP/MAS center bands to three Gaussian curves, giving chemical shifts of 171.1, 170.1 and 169.0 ppm.

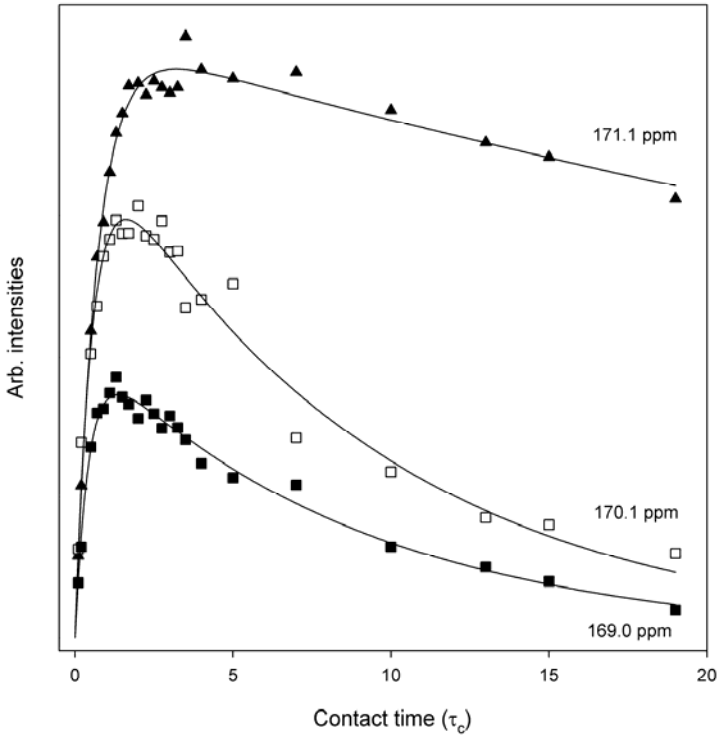

Figure 5.3 CP kinetics for the resonances contained in $^{13}C\{^1H\}$ CP/MAS spectra of the synthetic aragonite, acquired with CW CP at 5 kHz spinning rate. The peak intensities are arbitrarily re-scaled to separate the curves.

5.3.2 H environments

The 2-dimensional (2-D) $^{13}C\{^{1}H\}$ HETCOR NMR spectra were obtained to determine the nature of H in close proximity to carbonate groups. Fig. 5.4 shows the contour plot of a 2-D HetCor spectrum acquired with 4 ms contact time, and ^{1}H slices (F1) taken at ^{13}C peak positions of 171.1, 170.1 and 169.0 ppm are shown in Fig. 5.5(a-c). Each of these indirectly-detected ^{1}H spectra contains at least four components, including a broad spinning sideband (SSB) pattern centered at *ca.* 6.1 ppm, one narrow peak at 5.3 ppm and two small shoulders at ~14.4 ppm and 1.3 ppm. The broad SSB pattern results from strong ^{1}H-^{1}H homonuclear dipolar coupling, which can only be removed if the sample spinning rate is much higher than the coupling strength. Considering the chemical shift value of 6.1 ppm, this SSB pattern should be assigned to rigid H_2O molecules. The relatively narrow peak at 5.3 ppm is assigned to restrictedly mobile H_2O, since the dipolar coupling can be reduced by molecular tumbling. The resonance at 14.4 ppm represents ^{1}H with strong H-bonding, possibly arising from some bicarbonate groups [13]. The peak at 1.3 ppm is assigned to OH groups according to the chemical shift values [46]. Qualitatively, the indirectly observed ^{1}H spectra from HETCOR are very similar to those obtained previously for ACC [40], supporting the point that the peak at 169.0 ppm in $^{13}C\{^{1}H\}$ CP/MAS spectra arises from residual ACC in the sample. However, the ratio of the three H signals in the current HETCOR spectra differs from that obtained for ACC. This and the similarity of the slices to each other can be attributed to the high-degree of peak overlap in the ^{13}C dimension.

To further quantify the various H-bearing species associated with carbonates, $^{13}C\{^{1}H\}$ HETCOR spectra were acquired with an additional mixing time (τ_{mix}) added before the

contact time, during which the ^{1}H magnetization is stored along B_0 and can exchange among different spins via ^{1}H-^{1}H homonuclear dipolar interactions. At long mixing time, the ^{1}H magnetization reaches equilibrium in the sense that the spin temperature is the same for ^{1}H spins in the dipolar-coupled network associated with C, and the indirectly observed ^{1}H spectrum (F1 dimension in HETCOR) is quantitative according to the population of each H species in different environments. The HETCOR spectrum acquired with 75 ms mixing time is nearly identical to that acquired with 50 ms mixing time, indicating that the ^{1}H magnetization has reached equilibrium after 50 ms spin exchange. Fig. 5.5d shows a ^{1}H slice at a 75 ms mixing time taken at ^{13}C position of 171.1 ppm, where the relative intensity of the peak at 5.3 ppm increases compared with Fig. 5.5(a-c), indicating that the ^{1}H signal at 5.3 ppm has a lower CP rate to C, consistent with the assignment to H_2O molecules undergoing restricted motion. Similar to the ^{13}C{^{1}H} HETCOR spectra obtained without a mixing period, no significant variation is observed for equilibrated ^{1}H spectra taken at different ^{13}C peak positions, presumably also due to the strong overlap of ^{13}C resonances. However, it should be noted that the H species associated with the three ^{13}C resonances can not be exactly same, since the measured $T_{1\rho,\mathrm{H}}$ for the peak at 171.1 ppm is much longer than those for the other two resonances, indicating the difference in the time scale of ^{1}H motion. The ^{1}H relaxation in the rotating frame is sensitive to the applied spin-locking pulse power (i.e., $\omega_{1\mathrm{H}} = \gamma_{\mathrm{H}} B_{1\mathrm{H}}$), and the spin motion at the time scale of $2\omega_{1\mathrm{H}}$ (for the current experimental setup, $2\omega_{1\mathrm{H}} \approx 60$ kHz) is most effective for introducing relaxation [47]. So the mobile H_2O near carbonates with chemical shift of 171.1 ppm should have a different motional time scale from those near other carbonates. The $T_{1\rho,\mathrm{H}}$ for the ^{13}C signal at 170.1 ppm is close to that at 169.0 ppm

(ACC), suggesting the similarity of ^{1}H spin motion time scale. Considering a ^{13}C chemical shift value of 170.1 ppm suggests intermediate Ca/CO_3^{2-} bonding configurations between monodentate (e.g., for ACC) and bidentate (e.g., for bulk aragonite) [40], this ^{13}C signal at 170.1 ppm could arise from the poorly crystallized region near amorphous calcium carbonate phase.

Instead of directly measuring peak intensities in frequency domain spectra, the ^{1}H time domain signals were analyzed to avoid the uncertainty potentially introduced by trying to fit the broad peaks arising from rigid H_2O, hence obtain more accurately the ratio of different H species. A least-squares fit was performed for the slowly-decaying oscillation part of the ^{1}H free induction decay (FID) (dotted line in Fig. 5.6), taken at 171 ppm (^{13}C-dimension) in the partially transformed HETCOR spectrum acquired with 50 ms mixing time. The height of the 1st point at t = 0 is proportional to the intensity for this oscillating signal. The 1st point of the ^{1}H FID from HETCOR represents the total H intensity, so the amount of rigid H can be obtained by subtracting the intensity of the oscillating component from the total intensity, giving the ratio of rigid to mobile H around 34:15 (denoted in the ordinate of Fig. 5.6). The rigid H is present primarily as structural H_2O, and the OH and bicarbonate groups are only a small fraction of total intensity. Thus the ratio of rigid to mobile H (i.e., 34:15) implies that the ratio of rigid H_2O to mobile H_2O is around 2:1. The number of rigid H_2O associated with carbonate can be estimated by combination of this ratio with the $^{13}C\{^{1}H\}$ CP kinetics data. Assumption of two rigid H_2O results in the $N_{C\text{-}13}/N_{H\text{-}1}$ ratio (i.e. 4) which gives $T_{1\rho,H}$ values from CP kinetics closest to those $T_{1\rho,H}$ obtained through ^{13}C-detected ^{1}H spin-locking experiments. Therefore, based on the current experimental data we suggest that

an average hydrated defect structure in aragonite would contain two rigid H_2O and one mobile H_2O. So, two hydrogen-bonds could be formed for relevant carbonate groups, as explains the short T_{IS} measured from CP kinetics. Some additional experiments, such as measuring $T_{I\rho,\mathrm{H}}$ at different spin-locking pulse power, could could provide additional information on the nature of the hydrated defects in aragonite.

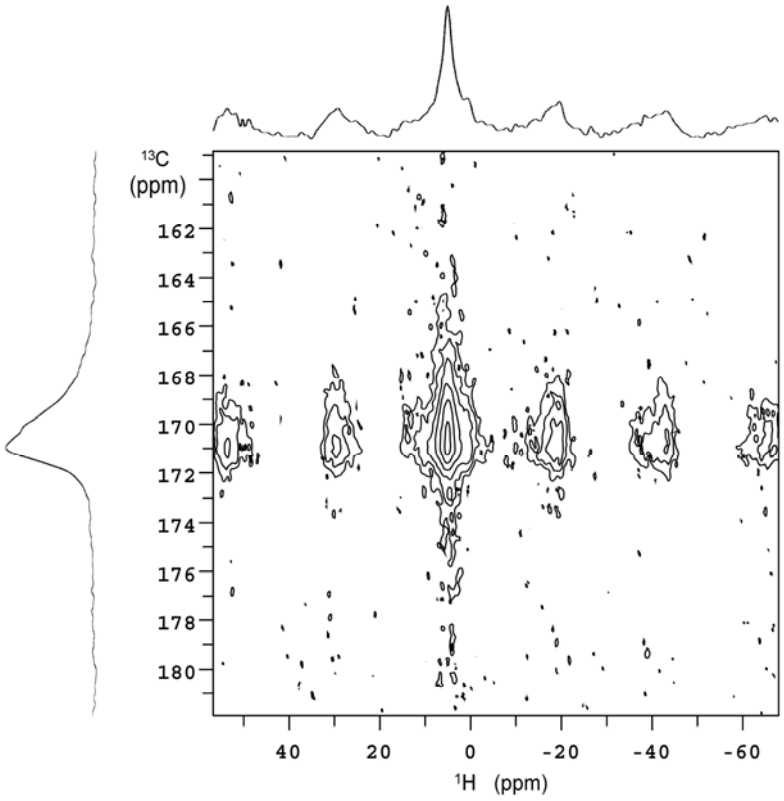

Figure 5.4 $^{13}C\{^{1}H\}$ HETCOR NMR spectrum of synthetic ^{13}C-enriched aragonite, acquired with 4 ms contact time, 10 kHz spinning rate, 80 hypercomplex points in $t1$ with an 20 μs increment, and 4000 scans for each hypercomplex point. No ^{1}H decoupling is applied in $t1$. The spectrum shown at left side is summed projection; top one is a ^{1}H slice across ^{13}C resonance at 171.0 ppm.

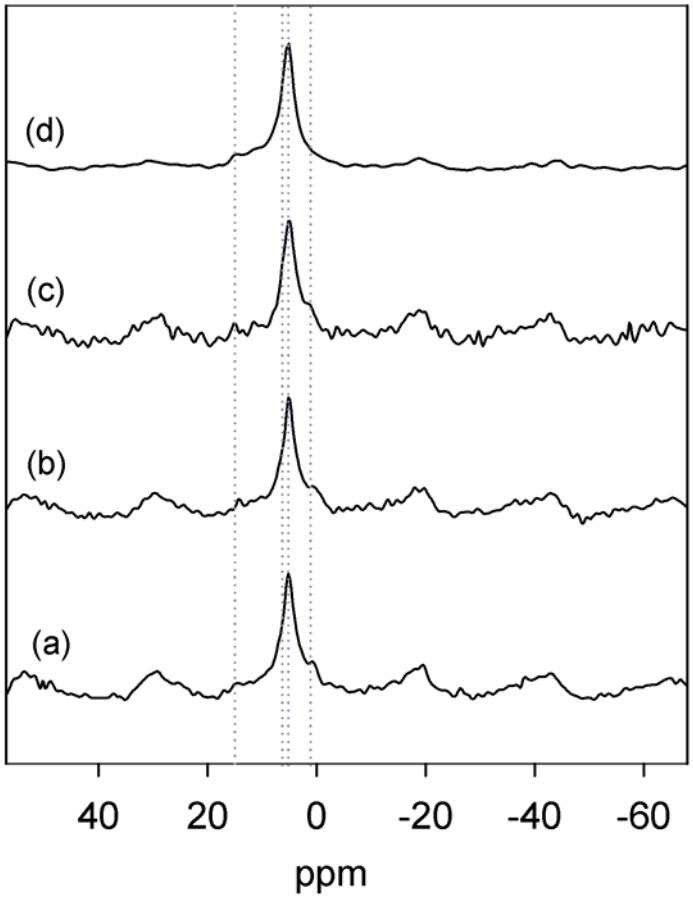

Figure 5.5 (a-c) ^{1}H slices taken from $^{13}C\{^{1}H\}$ HETCOR spectrum acquired at 4 ms contact with no mixing time (i.e., the spectrum shown in Fig. 5.4). The corresponding ^{13}C resonances are 171.1 ppm for (a), 170.1 ppm for (b) and 169.0 ppm for (c). (d) ^{1}H slice taken at 171.1 ppm (^{13}C-dimension) from HETCOR with a 75 ms mixing time. Dotted lines denote the isotropic ^{1}H peak positions.

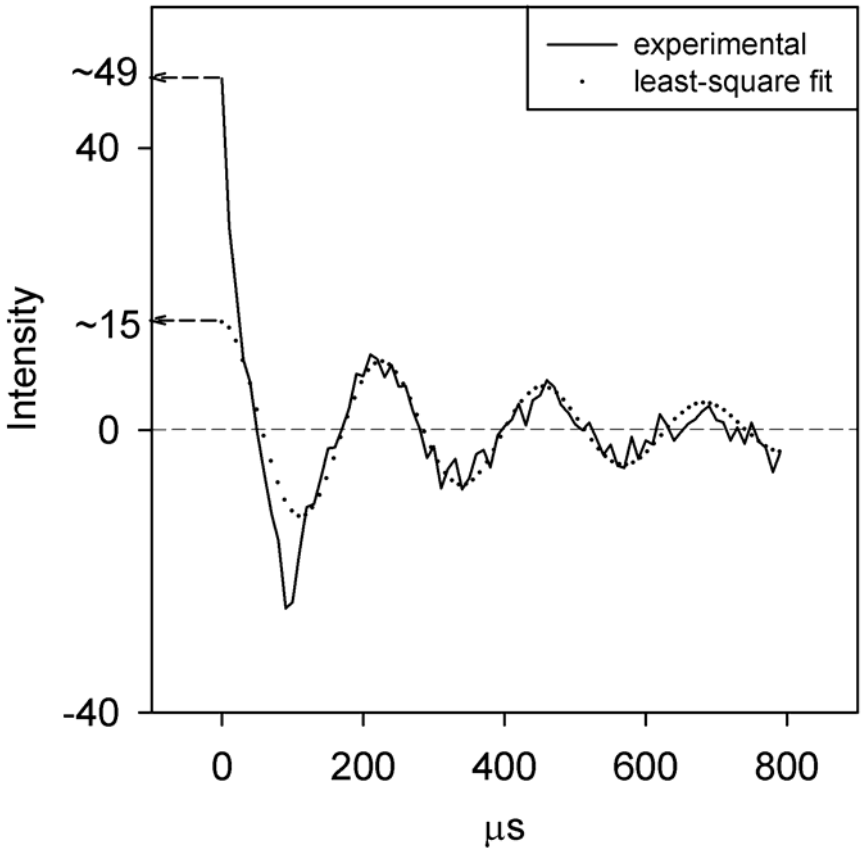

Figure 5.6 (—) Solid line represents the ^{1}H time domain FID ($t1$) taken at 171.1 ppm (^{13}C-dimension) from ^{13}C {^{1}H} HETCOR spectrum acquired with 75 ms mixing time, corresponding to the ^{1}H spectrum in Fig. 5.4(d). Experimental (···) Dotted line is the least-squares fit of the oscillation part (230 ~ 800 μs) of the FID.

5.3.3 Implications for biogenic aragonite

Nassif [12] and Jäger [13] observed similar asymmetric line shapes in $^{13}C\{^{1}H\}$ CP/MAS spectra for a biogenic nacre, for which ^{1}H spectra associated with carbonate taken from HETCOR contain two narrow components at 14.4 and 5.2 ppm. In these studies, the asymmetric ^{13}C signals were treated as a single resonance arising from the amorphous calcium carbonate phase. However, this assignment is inconsistent with our previous observation for an additive-free synthetic ACC sample, for which the $^{13}C\{^{1}H\}$ CP/MAS spectra contain a broad, symmetric resonance and the ^{1}H spectra taken from HETCOR indicates the existence of rigid structural H_2O, mobile H_2O and a small fraction of OH groups. Despite the possibility that the biogenic ACC has a different structure, it is still surprising that such a large amount of H_2O (CO_3^{2-}: $H_2O \approx 1:1$) undergoes restricted motion while keeping the structure stable. Considering the similarity of the line shape of signals in $^{13}C\{^{1}H\}$ CP/MAS spectra between the biogenic nacre and the synthetic aragonite here, we suggest that the ^{13}C signal of nacre arises from the same source as those we discovered for the synthetic aragonite, i.e. partially from the intrinsic defects in aragonite and partially from the residual ACC formed during the growth of aragonite crystal. The difference in ^{1}H spectra from HETCOR between the nacre and the synthetic aragonite could be due to the line broadening caused by the strong ^{1}H-^{1}H dipolar coupling of rigid H_2O, which could be hard to observe in frequency-domain spectra with poor sensitivity caused by low ^{13}C natural abundance. However, our findings for synthetic aragonite also indicate that the asymmetric ^{13}C line shape is partially from ACC, as is consistent with the TEM observation for biogenic [12] and synthetic aragonite [48],

although the NMR data cannot distinguish whether these ACC residues are located on the surface or in the bulk.

5.4 Conclusion

NMR spectroscopic study on a synthetic, additive-free aragonite sample shows that the intrinsic hydrated defects contained in the bulk and the residual amorphous phase can give rise to detectable NMR signals in $^{13}C\{^{1}H\}$ CP/MAS spectra. CSA analysis, CP kinetics data and HETCOR spectra suggest the defect carbonates are primarily non-protonated groups. $^{13}C\{^{1}H\}$ HETCOR spectra indicate that most H species associated with the defects are present as rigid and mobile structural H_2O, with small portions being OH groups and H with strong H-bond, which could be assigned to bicarbonates. The overall line shape of the signals in $^{13}C\{^{1}H\}$ CP/MAS NMR spectra for this synthetic aragonite sample resembles that observed for a biogenic nacre [12,13], and relative intensity of CP to SP is comparable to that estimated for the nacre. Consequently, the ^{13}C signals arising from intrinsic defects and remaining ACC in aragonite must be taken into account when analyzing NMR data obtained for naturally biogenic samples.

5.5 References

1. Lowenstam HA, Weiner S. *On biomineralization*. Oxford University Press: New York, 1989, ix, 324 p.
2. Simkiss K, Wilbur KM. *Biomineralization : cell biology and mineral deposition*. Academic Press: San Diego, 1989, xiv, 337 p.
3. Backstrom HLJ, *J. Am. Chem. Soc.*, 1925, **47**: 2432-2442.
4. Brooks R, Clark LM, Thurston EF, *Philos. Trans. R. Soc. London, Ser. A*, 1950, **243**: 145-167.
5. Addadi L, Weiner S, *Angew. Chem. Int. Ed. Engl.*, 1992, **31**: 153-169.
6. Mann S. *Biomineralization: principles and concepts in bioinorganic materials chemistry*. Oxford University Press: New York, 2001, xii, 198 p.
7. Weiner S, Traub W, *Philos. Trans. R. Soc. London, Ser. B*, 1984, **304**: 425-&.
8. Fritz M, Belcher AM, Radmacher M, Walters DA, Hansma PK, Stucky GD, Morse DE, Mann S, *Nature*, 1994, **371**: 49-51.
9. Zaremba CM, Belcher AM, Fritz M, Li YL, Mann S, Hansma PK, Morse DE, Speck JS, Stucky GD, *Chem. Mater.*, 1996, **8**: 679-690.
10. Levi-Kalisman Y, Falini G, Addadi L, Weiner S, *J. Struct. Biol.*, 2001, **135**: 8-17.
11. Takahashi K, Yamamoto H, Onoda A, Doi M, Inaba T, Chiba M, Kobayashi A, Taguchi T, Okamura T, Ueyama N, *Chem. Commun.*, 2004: 996-997.
12. Nassif N, Pinna N, Gehrke N, Antonietti M, Jäger C, Cölfen H, *Proc. Natl. Acad. Sci. U.S.A.*, 2005, **102**: 12653-12655.
13. Jäger C, Cölfen H, *Crystengcomm*, 2007, **9**: 1237-1244.
14. Gregoire C, *J. Biophys. Biochem. Cytology*, 1957, **3**: 797-&.

15. Cölfen H, Mann S, *Angew. Chem. Int. Ed.*, 2003, **42**: 2350-2365.

16. Weiner S, Addadi L, *J. Mater. Chem.*, 1997, **7**: 689-702.

17. Pines A, Gibby MG, Waugh JS, *J. Chem. Phys.*, 1973, **59**: 569-590.

18. Stejskal EO, Schaefer J, Waugh JS, *J. Magn. Reson.*, 1977, **28**: 105-112.

19. Mehring M. *Principles of high-resolution NMR in solids*. Springer-Verlag: Berlin, New York, 1983.

20. Kolodziejski W, Klinowski J, *Chem. Rev.*, 2002, **102**: 613-628.

21. Schmidtrohr K, Clauss J, Spiess HW, *Macromolecules*, 1992, **25**: 3273-3277.

22. Vega AJ, *J. Am. Chem. Soc.*, 1988, **110**: 1049-1054.

23. Gullion T, Schaefer J, *J Magn Reson*, 1989, **81**: 196-200.

24. Grey CP, Veeman WS, Vega AJ, *J. Chem. Phys.*, 1993, **98**: 7711-7724.

25. Grey CP, Vega AJ, *J. Am. Chem. Soc.*, 1995, **117**: 8232-8242.

26. Gullion T, *Chem. Phys. Lett.*, 1995, **246**: 325-330.

27. Berner RA, *Geochimica Et Cosmochimica Acta*, 1975, **39**: 489-&.

28. Morse JW, Arvidson RS, Luttge A, *Chem. Rev.*, 2007, **107**: 342-381.

29. Zhong SJ, Mucci A, *Geochimica Et Cosmochimica Acta*, 1993, **57**: 1409-1417.

30. Tesoriero AJ, Pankow JF, *Geochim. Cosmochim. Acta*, 1996, **60**: 1053-1063.

31. Tang YZ, Elzinga EJ, Lee YJ, Reeder RJ, *Geochim. Cosmochim. Acta*, 2007, **71**: 1480-1493.

32. Mason HE, Frisia S, Tang Y, Reeder RJ, Phillips BL, *Earth. Planet. Sci. Lett.*, 2007, **254**: 313-322.

33. Hall PO, Aller RC, *Limnology and Oceanography*, 1992, **37**: 1113-1119.

34. Parkhurst DL, Appelo CAJ. *User's guide to PHREEQC (Version 2) - A computer program for speciation, batch-reaction, one-dimensional transport, and inverse geochemical calculations.* U. S. Geol. Surv. Water Res. Inv. Rept., 1999, 99-4259.

35. Eichele K, Wasylishen RE. *HBA*, Version: 1.5. Dalhousie University and Universität Tübingen, 2006.

36. Dalnegro A, Ungarett.L, *Am. Mineral.*, 1971, **56**: 768-&.

37. Devillie.Jp, *Am. Mineral.*, 1971, **56**: 758-&.

38. Dickens B, Bowen JS, *J. Res. Natl. Bureau Stand. Sect. A, Phys. Chem.*, 1971, **A 75**: 27-&.

39. Phillips BL, Lee YJ, Reeder RJ, *Environ. Sci. Technol.*, 2005, **39**: 4533-4539.

40. Michel FM, MacDonald J, Feng J, Phillips BL, Ehm L, Tarabrella C, Parise JB, Reeder RJ, *Chemistry of Materials*, 2008, **20**: 4720-4728.

41. Nebel H, Neumann M, Mayer C, Epple M, *Inorganic Chemistry*, 2008, **47**: 7874-7879.

42. Feng J, Lee YJ, Reeder RJ, Phillips BL, *American Mineralogist*, 2006, **91**: 957-960.

43. Gu ZT, Mcdermott A, *J. Am. Chem. Soc.*, 1993, **115**: 4282-4285.

44. Gu ZT, Zambrano R, Mcdermott A, *J. Am. Chem. Soc.*, 1994, **116**: 6368-6372.

45. Feng J, Lee YJ, Kubicki JD, Reeder RJ, Phillips BL, *Magnetic Resonance in Chemistry*, 2008, **46**: 408-417.

46. Yesinowski JP, Eckert H, Rossman GR, *J. Am. Chem. Soc.*, 1988, **110**: 1367-1375.

47. Stejskal EO, Memory JD. *High resolution NMR in the solid state : fundamentals of CP/MAS*. Oxford University Press: New York, 1994.

48. Nassif N, Gehrke N, Pinna N, Shirshova N, Tauer K, Antonietti M, Cölfen H, *Angew. Chem. Int. Ed.*, 2005, **44**: 6004-6009.

Chapter 6

Conclusions and envision for future work

In this thesis, NMR spectroscopy is applied systematically to study of the intrinsic hydrated defects in synthetic calcium carbonate mineral phases, i.e. calcite and aragonite, and of the H species in an additive-free amorphous phase. The hydrous species contained in both calcite and aragonite can give rise to easily detectable NMR signals in $^{13}C\{^{1}H\}$ CP/MAS spectra. For the calcite, the ^{13}C isotropic peak position in CP spectra is identical to that in SP spectra, and the H-bearing species is bicarbonate groups. The $^{13}C\{^{1}H\}$ CP/MAS spectra for the synthetic aragonite contain three resonances arising from hydrated defects as well as residual amorphous phase in the sample. The three components largely overlap, showing an overall asymmetric line shape, which resembles that observed for a biogenic nacre. Therefore, the $^{13}C\{^{1}H\}$ CP/MAS NMR signals arising from the intrinsic defects should be considered when studying biogenic and biomimetic materials with calcite or aragonite as the mineral components. Most of the H species in ACC are contained as structural H_2O, about half of which undergo restricted motion, as is supported by CP kinetics data and HETCOR spectra obtained at both room temperature and low temperature. The presence of large amounts of mobile H_2O in the ACC explains the intrinsic instability of the structure. The ^{13}C NMR spectra are also proven to be an

effective probe for distinguishing various calcium carbonate phases according to the isotropic ^{13}C peak positions and the line shapes.

In addition, a correlation between T_{IS} and M_2^{IS} is established based on Mg(II)-cit and Sr(II)-cit, according to which more quantitative geometrical information can be obtained from CP kinetics data. The application of this correlation curve to a calcite/citrate composite indicates the proximity between carbonates and citrate methylene groups, and provides a quantitative constraint for future computational work on the citrate intracrystalline defect structure.

In summary, our results demonstrate that the NMR spectroscopy is potentially a useful and effective tool for characterization of the biogenic calcium carbonate mineral/organic composites. The NMR data included in this thesis provide a baseline for further NMR spectroscopic study of biomineralized $CaCO_3$ materials with more complicated composition and construct.

The primary challenge for the *in situ* study of biogenic $CaCO_3$ minerals is the poor sensitivity arising from the low ^{13}C natural abundance (~ 1%), which largely excludes the efficient application of 2-D or double resonance NMR techniques. As a consequence, isotope-enriched biomimetic materials can play an important role in investigating the mineral/organic interface interactions using solid state NMR spectroscopy. Occurrence of biomineralization processes in isotope-enriched environment is the ideal way for obtaining samples facilitating NMR spectroscopic study, and an attempt has been made

on the preparation of calcite from unicellular alga [1]. So, developing strategies for *in vivo* preparation of selectively isotope-enriched sample will be promising for providing more direct and unambiguous information for elucidating the $CaCO_3$/organic interface structure.

Reference

1. Gertman R, Shir IB, Kababya S, Schmidt A, *J. Am. Chem. Soc.*, 2008, **130**: 13425-13432.

References

Chapter 1

1. Zeebe RE, Zachos JC, Caldeira K, Tyrrell T, *Science*, 2008, **321**: 51-52.
2. DeYoreo JJ, Vekilov PG, *Rev. Mineral. Geochem.*, Dove PM, DeYoreo JJ, Weiner S (Eds.), 2003, **54**: 57-93. Mineralogical Society of America: Washington, DC.
3. Niederberger M, Cölfen H, *Phys. Chem. Chem. Phys.*, 2006, **8**: 3271-3287.
4. Mann S. *Biomineralization: principles and concepts in bioinorganic materials chemistry*. Oxford University Press: New York, 2001, xii, 198 p.
5. Weiner S, Traub W, *Philos. Trans. R. Soc. London, Ser. B*, 1984, **304**: 425-&.
6. Lowenstam HA, Weiner S. *On biomineralization*. Oxford University Press: New York, 1989, ix, 324 p.
7. Takahashi K, Yamamoto H, Onoda A, Doi M, Inaba T, Chiba M, Kobayashi A, Taguchi T, Okamura T, Ueyama N, *Chem. Commun.*, 2004: 996-997.
8. Nassif N, Pinna N, Gehrke N, Antonietti M, Jäger C, Cölfen H, *Proc. Natl. Acad. Sci. U.S.A.*, 2005, **102**: 12653-12655.
9. Jäger C, Cölfen H, *Crystengcomm*, 2007, **9**: 1237-1244.
10. Cölfen H, Mann S, *Angew. Chem. Int. Ed.*, 2003, **42**: 2350-2365.
11. Brooks R, Clark LM, Thurston EF, *Philos. Trans. R. Soc. London, Ser. A*, 1950, **243**: 145-167.

12. Hasse B, Ehrenberg H, Marxen JC, Becker W, Epple M, *Chemistry-a European Journal*, 2000, **6**: 3679-3685.

13. Politi Y, Levi-Kalisman Y, Raz S, Wilt F, Addadi L, Weiner S, Sagi I, *Adv. Funct. Mater.*, 2006, **16**: 1289-1298.

14. Lam RSK, Charnock JM, Lennie A, Meldrum FC, *Crystengcomm*, 2007, **9**: 1226-1236.

15. Slichter CP. *Principles of magnetic resonance*. Springer-Verlag: Berlin, New York, 1989.

16. Bak M, Rasmussen JT, Nielsen NC, *J. Magn. Reson.*, 2000, **147**: 296-330.

17. Haeberlen U, *Adv. Magn. Reson.*, Waugh JS (Ed.), 1976, **Suppl. 1**. Academic Press: New York.

18. Mehring M. *Principles of high-resolution NMR in solids*. Springer-Verlag: Berlin, New York, 1983.

19. Andrew ER, Bradbury A, Eades RG, *Nature*, 1958, **182**: 1659.

20. Lowe IJ, *Phys. Rev. Lett.*, 1959, **2**: 285.

21. Hartmann S, Hahn EL, *Phys. Rev.*, 1962, **128**: 2042-&.

22. Demco DE, Tegenfeldt J, Waugh JS, *Phys. Rev. B*, 1975, **11**: 4133-4151.

23. Muller L, Kumar A, Baumann T, Ernst RR, *Phys. Rev. Lett.*, 1974, **32**: 1402-1406.

24. Hediger S. *Improvement of heteronuclear polarization transfer in solid-state NMR*, Ph.D. dissertation, 1997. Eidgenössische Technische Hochschule, Zürich.

25. Alemany LB, Grant DM, Alger TD, Pugmire RJ, *J. Am. Chem. Soc.*, 1983, **105**: 6697-6704.

26. Wu XL, Zhang SM, Wu XW, *Phys. Rev. B*, 1988, **37**: 9827-9829.

27. Wu XL, Zilm KW, *J. Magn. Reson.*, 1991, **93**: 265-278.

28. Kolodziejski W, Klinowski J, *Chem. Rev.*, 2002, **102**: 613-628.

29. Fyfe CA, Lewis AR, Chezeau JM, *Can. J. Chem.*, 1999, 77: 1984-1993.

30. Vega AJ, J. Am. Chem. Soc., 1988, 110: 1049-1054.

31. Schmidt-Rohr K, Clauss J, Spiess HW, Macromolecules, 1992, 25: 3273-3277.

Chapter 2

1. Berman A, Addadi L, Kvick A, Leiserowitz L, Nelson M, Weiner S, *Science*, 1990, **250**: 664-667.

2. Neuweiler F, Rutsch M, Geipel G, Reimer A, Heise KH, *Geology*, 2000, **28**: 851-854.

3. Ramseyer K, Miano TM, D'Orazio V, Wildberger A, Wagner T, Geister J, *Org. Geochem.*, 1997, **26**: 361-378.

4. Sykes GA, Collins, M. J., Walton, D. I., *Org. Geochem.*, 1995, **23**: 1059-1065.

5. Walton D, *Org. Geochem.*, 1998, **28**: 389-410.

6. Dauphin Y, Cuif JP, Salome C, Susini J, *Am. Mineral.*, 2005, **90**: 1748-1758.

7. Takahashi K, Yamamoto H, Onoda A, Doi M, Inaba T, Chiba M, Kobayashi A, Taguchi T, Okamura T, Ueyama N, *Chem. Commun.*, 2004: 996-997.

8. Phillips BL, Lee YJ, Reeder RJ, *Environ. Sci. Technol.*, 2005, **39**: 4533-4539.

9. Takahashi K, Doi M, Kobayashi A, Taguchi T, Onoda A, Okamura TA, Yamamoto H, Ueyama N, *Chem. Lett.*, 2004, **33**: 192-193.

10. Ueyama N, Hosoi T, Yamada Y, Doi M, Okamura T, Nakamura A, *Macromolecules*, 1998, **31**: 7119-7126.

11. Eichele K, Wasylishen RE. *HBA*, Version: 1.5. Dalhousie University and Universität Tübingen, 2006.

12. Hediger S. *Improvement of heteronuclear polarization transfer in solid-state NMR*, Ph.D. dissertation, 1997. Eidgenössische Technische Hochschule, Zürich.

13. Fyfe CA, Lewis AR, Chezeau JM, *Can. J. Chem.*, 1999, **77**: 1984-1993.

14. Sharma BD, *Acta Crystallogr.*, 1965, **18**: 818-&.

15. Lauterbur PC, *Phys. Rev. Lett.*, 1958, **1**: 343-344.

16. Pines A, Rhim WK, Waugh JS, *J. Chem. Phys.*, 1971, **54**: 5438-&.

17. Zumbulyadis N, *Phys. Rev. B*, 1986, **33**: 6495-6496.

18. Schmidtrohr K, Clauss J, Spiess HW, *Macromolecules*, 1992, **25**: 3273-3277.

19. Gaffey SJ, *Am. Mineral.*, 1995, **80**: 947-959.

20. Bischoff WD, Sharma SK, Mackenzie FT, *Am. Mineral.*, 1985, **70**: 581-589.

21. Duffy DM, Travaille AM, van Kempen H, Harding JH, *J. Phys. Chem. B*, 2005, **109**: 5713-5718.

22. Brunner E, Sternberg U, *Prog. Nucl. Magn. Reson. Spectrosc.*, 1998, **32**: 21-57.

23. Yesinowski JP, Eckert H, Rossman GR, *J. Am. Chem. Soc.*, 1988, **110**: 1367-1375.

24. Choi CS, Mighell AD, *Acta Crystallogr., Sect. B-Struct. Sci.*, 1982, **38**: 2874-2876.

25. Markgraf SA, Halliyal A, Bhalla AS, Newnham RE, Prewitt CT, *Ferroelectrics*, 1985, **62**: 17-26.

26. Nassif N, Pinna N, Gehrke N, Antonietti M, Jäger C, Cölfen H, *Proc. Natl. Acad. Sci. U.S.A.*, 2005, **102**: 12653-12655.

Chapter 3

1. Amjad Z, *Langmuir*, 1987, **3**: 224-228.

2. Geffroy C, Foissy A, Persello J, Cabane B, *J. Colloid Interface Sci.*, 1999, **211**: 45-53.

3. Orme CA, Noy A, Wierzbicki A, McBride MT, Grantham M, Teng HH, Dove PM, DeYoreo JJ, *Nature*, 2001, **411**: 775-779.

4. Reddy MM, Hoch AR, *J. Colloid Interface Sci.*, 2001, **235**: 365-370.

5. Teng HH, Dove, P. M., *Am. Mineral.*, 1997, **82**: 878-887.

6. Ueyama N, Hosoi T, Yamada Y, Doi M, Okamura T, Nakamura A, *Macromolecules*, 1998, **31**: 7119-7126.

7. Berman A, Addadi L, Kvick A, Leiserowitz L, Nelson M, Weiner S, *Science*, 1990, **250**: 664-667.

8. Neuweiler F, Rutsch M, Geipel G, Reimer A, Heise KH, *Geology*, 2000, **28**: 851-854.

9. Ramseyer K, Miano TM, DOrazio V, Wildberger A, Wagner T, Geister J, *Org. Geochem.*, 1997, **26**: 361-378.

10. Sykes GA, Collins, M. J., Walton, D. I., *Org. Geochem.*, 1995, **23**: 1059-1065.

11. Walton D, *Org. Geochem.*, 1998, **28**: 389-410.

12. Phillips BL, Lee YJ, Reeder RJ, *Environ. Sci. Technol.*, 2005, **39**: 4533-4539.

13. Takahashi K, Doi, M., Kobayashi, A., Taguchi, T., Onoda, A., Okamura, T. A., Yamamoto, H., Ueyama, N., *Chem. Lett.*, 2004, **33**: 192-193.

14. Ueyama N, Kozuki H, Doi M, Yamada Y, Takahashi K, Onoda A, Okamura T, Yamamoto H, *Macromolecules*, 2001, **34**: 2607-2614.

15. Feng J, Lee YJ, Reeder RJ, Phillips BL, *Am. Mineral.*, 2006, **91**: 957-960.

16. Gullion T, Schaefer J, *J. Magn. Reson.*, 1989, **81**: 196-200.

17. Christensen AM, Schaefer J, *Biochemistry*, 1993, **32**: 2868-2873.

18. Pan Y, Shenouda NS, Wilson GE, Schaefer J, *J. Biol. Chem.*, 1993, **268**: 18692-18695.

19. Hing AW, Tjandra N, Cottam PF, Schaefer J, Ho C, *Biochemistry*, 1994, **33**: 8651-8661.

20. Hediger S. *Improvement of heteronuclear polarization transfer in solid-state NMR,* Ph.D. dissertation, 1997. Eidgenössische Technische Hochschule, Zürich.

21. Fyfe CA, Lewis AR, Chezeau JM, *Can. J. Chem.*, 1999, **77**: 1984-1993.

22. Bertmer M, Eckert H, *Solid State Nucl. Magn. Reson.*, 1999, **15**: 139-152.

23. Goetz JM, Schaefer J, *J. Magn. Reson.*, 1997, **127**: 147-154.

24. Chan JCC, Eckert H, *J. Magn. Reson.*, 2000, **147**: 170-178.

25. Johnson CK, *Acta Crystallogr.*, 1965, **18**: 1004-&.

26. Zacharias DE, Glusker JP, *Acta Crystallogr., Sect. C-Cryst. Struct. Commun.*, 1993, **49**: 1732-1735.

27. Cariati F, Erre L, Micera G, Panzanelli A, Ciani G, Sironi A, *Inorg. Chim. Acta-Bioinorg. Chem.*, 1983, **80**: 57-65.

28. Neder RB, Burghammer M, Grasl T, Schulz H, Bram A, Fiedler S, *Clays Clay Miner.*, 1999, **47**: 487-494.

29. Tesoriero AJ, Pankow JF, *Geochim. Cosmochim. Acta*, 1996, **60**: 1053-1063.

30. Zhong SJ, Mucci A, *Geochim. Cosmochim. Acta*, 1993, **57**: 1409-1417.

31. Jakobsen HJ, Skibsted J, Bildsoe H, Nielsen NC, *J. Magn. Reson.*, 1989, **85**: 173-180.

32. Frisch MJ, Trucks GW, Schlegel HB, Scuseria GE, Robb MA, Cheeseman JR, Montgomery JA, Jr. , Vreven T, Kudin KN, Burant JC, Millam JM, Iyengar SS, Tomasi J, Barone V, Mennucci B, Cossi M, Scalmani G, Rega N, Petersson GA, Nakatsuji H, M. Hada, M. Ehara, K. Toyota, Fukuda R, Hasegawa J, Ishida M, Nakajima T, Honda Y, Kitao O, Nakai H, Klene M, Li X, Knox JE, Hratchian HP, Cross JB, Adamo C, Jaramillo J, Gomperts R, Stratmann RE, Yazyev O, Austin AJ, Cammi R, Pomelli C, Ochterski JW, Ayala PY, Morokuma K, Voth GA, Salvador P, Dannenberg JJ, Zakrzewski VG, Dapprich S, Daniels AD, Strain MC, Farkas O, Malick DK, Rabuck AD, Raghavachari K, Foresman JB, Ortiz JV, Cui Q, Baboul AG, Clifford S, Cioslowski J, Stefanov BB, Liu G, Liashenko A, Piskorz P, Komaromi I, Martin RL, Fox DJ, Keith T, Al-Laham MA, Peng CY, Nanayakkara A, Challacombe M, Gill PMW, Johnson B, Chen W, Wong MW, Gonzalez C, Pople JA. *Gaussian 03,* Version: C.01. Gaussian Inc., Wallingford, CT, 2004.

33. Becke AD, *J. Chem. Phys.*, 1993, **98**: 5648-5652.

34. Gordon MS, Binkley JS, Pople JA, Pietro WJ, Hehre WJ, *J. Am. Chem. Soc.*, 1982, **104**: 2797-2803.

35. Krishnan R, Binkley JS, Seeger R, Pople JA, *J. Chem. Phys.*, 1980, **72**: 650-654.

36. Lee CT, Yang WT, Parr RG, *Phys. Rev. B*, 1988, **37**: 785-789.

37. Mclean AD, Chandler GS, *J. Chem. Phys.*, 1980, **72**: 5639-5648.

38. Wolinski K, Hinton JF, Pulay P, *J. Am. Chem. Soc.*, 1990, **112**: 8251-8260.

39. Mehring M. *Principles of high-resolution NMR in solids*. Springer-Verlag: Berlin, New York, 1983.

40. Stejskal EO, Memory JD. *High resolution NMR in the solid state : fundamentals of CP/MAS*. Oxford University Press: New York, 1994.

41. Michel D, Engelke F, *Solid-State NMR III: Organic Matter*, Blümich B (Ed.), 1994, **31**. Springer-Verlag, Berlin.

42. Demco DE, Tegenfeldt J, Waugh JS, *Phys. Rev. B*, 1975, **11**: 4133-4151.

43. Hayashi S, Ueda T, Hayamizu K, Akiba E, *J. Phys. Chem.*, 1992, **96**: 10922-10928.

44. Phillips BL, Houston JR, Feng J, Casey WH, *J. Am. Chem. Soc*., 2006, **128**: 3912-3913.

45. Fyfe CA, Diaz AC, Grondey H, Lewis AR, Forster H, *J. Am. Chem. Soc.*, 2005, **127**: 7543-7558.

46. Yesinowski JP, Eckert H, Rossman GR, *J. Am. Chem. Soc.*, 1988, **110**: 1367-1375.

47. de Leeuw NH, Cooper TG, *Cryst. Growth Des.*, 2004, **4**: 123-133.

48. Gu ZT, Ridenour CF, Bronnimann CE, Iwashita T, McDermott A, *J. Am. Chem. Soc.*, 1996, **118**: 822-829.

49. Zorin VE, Brown SP, Hodgkinson P, *Mol. Phys.*, 2006, **104**: 293-304.

50. Brunner E, Sternberg U, *Prog. Nucl. Magn. Reson. Spectrosc.*, 1998, **32**: 21-57.

51. Kolodziejski W, Klinowski J, *Chem. Rev.*, 2002, **102**: 613-628.

52. Kaflak-Hachulska A, Slosarczyk A, Kolodziejski W, *Solid State Nucl. Magn. Reson.*, 2000, **15**: 237-238.

Chapter 4

1. Mann S. *Biomineralization: principles and concepts in bioinorganic materials chemistry*. Oxford University Press: New York, 2001, xii, 198 p.

2. Lowenstam HA, Weiner S. *On biomineralization*. Oxford University Press: New York, 1989, ix, 324 p.

3. Aizenberg J, Muller DA, Grazul JL, Hamann DR, *Science*, 2003, **299**: 1205-1208.

4. Dujardin E, Mann S, *Adv. Mater.*, 2002, **14**: 775-788.

5. Addadi L, Raz S, Weiner S, *Adv. Mater.*, 2003, **15**: 959-970.

6. Koga N, Nakagoe YZ, Tanaka H, *Thermochim. Acta*, 1998, **318**: 239-244.

7. Faatz M, Grohn F, Wegner G, *Adv. Mater.*, 2004, **16**: 996-1000.

8. Schmidtrohr K, Clauss J, Spiess HW, *Macromolecules*, 1992, **25**: 3273-3277.

9. Mehring M. *Principles of high-resolution NMR in solids*. Springer-Verlag: Berlin, New York, 1983.

10. Kolodziejski W, Klinowski J, *Chem. Rev.*, 2002, **102**: 613-628.

11. Yesinowski JP, Eckert H, Rossman GR, *J. Am. Chem. Soc.*, 1988, **110**: 1367-1375.

12. Feng J, Lee YJ, Reeder RJ, Phillips BL, *Am. Mineral.*, 2006, **91**: 957-960.

13. Egami T, Billinge SJL. *Underneath the Bragg peaks : structural analysis of complex materials*. Pergamon: Kiddington, Oxford, UK ; Boston, 2003, xviii, 404 p.

14. Michel FM, MacDonald J, Feng J, Phillips BL, Ehm L, Tarabrella C, Parise JB, Reeder RJ, *Chem. Mater.*, 2008, **20**: 4720-4728.

Chapter 5

1. Lowenstam HA, Weiner S. *On biomineralization*. Oxford University Press: New York, 1989, ix, 324 p.

2. Simkiss K, Wilbur KM. *Biomineralization : cell biology and mineral deposition*. Academic Press: San Diego, 1989, xiv, 337 p.

3. Backstrom HLJ, *J. Am. Chem. Soc.*, 1925, **47**: 2432-2442.

4. Brooks R, Clark LM, Thurston EF, *Philos. Trans. R. Soc. London, Ser. A*, 1950, **243**: 145-167.

5. Addadi L, Weiner S, *Angew. Chem. Int. Ed. Engl.*, 1992, **31**: 153-169.

6. Mann S. *Biomineralization: principles and concepts in bioinorganic materials chemistry*. Oxford University Press: New York, 2001, xii, 198 p.

7. Weiner S, Traub W, *Philos. Trans. R. Soc. London, Ser. B*, 1984, **304**: 425-&.

8. Fritz M, Belcher AM, Radmacher M, Walters DA, Hansma PK, Stucky GD, Morse DE, Mann S, *Nature*, 1994, **371**: 49-51.

9. Zaremba CM, Belcher AM, Fritz M, Li YL, Mann S, Hansma PK, Morse DE, Speck JS, Stucky GD, *Chem. Mater.*, 1996, **8**: 679-690.

10. Levi-Kalisman Y, Falini G, Addadi L, Weiner S, *J. Struct. Biol.*, 2001, **135**: 8-17.

11. Takahashi K, Yamamoto H, Onoda A, Doi M, Inaba T, Chiba M, Kobayashi A, Taguchi T, Okamura T, Ueyama N, *Chem. Commun.*, 2004: 996-997.

12. Nassif N, Pinna N, Gehrke N, Antonietti M, Jäger C, Cölfen H, *Proc. Natl. Acad. Sci. U.S.A.*, 2005, **102**: 12653-12655.

13. Jäger C, Cölfen H, *Crystengcomm*, 2007, **9**: 1237-1244.

14. Gregoire C, *J. Biophys. Biochem. Cytology*, 1957, **3**: 797-&.

15. Cölfen H, Mann S, *Angew. Chem. Int. Ed.*, 2003, **42**: 2350-2365.

16. Weiner S, Addadi L, *J. Mater. Chem.*, 1997, **7**: 689-702.

17. Pines A, Gibby MG, Waugh JS, *J. Chem. Phys.*, 1973, **59**: 569-590.

18. Stejskal EO, Schaefer J, Waugh JS, *J. Magn. Reson.*, 1977, **28**: 105-112.

19. Mehring M. *Principles of high-resolution NMR in solids*. Springer-Verlag: Berlin, New York, 1983.

20. Kolodziejski W, Klinowski J, *Chem. Rev.*, 2002, **102**: 613-628.

21. Schmidtrohr K, Clauss J, Spiess HW, *Macromolecules*, 1992, **25**: 3273-3277.

22. Vega AJ, *J. Am. Chem. Soc.*, 1988, **110**: 1049-1054.

23. Gullion T, Schaefer J, *J Magn Reson*, 1989, **81**: 196-200.

24. Grey CP, Veeman WS, Vega AJ, *J. Chem. Phys.*, 1993, **98**: 7711-7724.

25. Grey CP, Vega AJ, *J. Am. Chem. Soc.*, 1995, **117**: 8232-8242.

26. Gullion T, *Chem. Phys. Lett.*, 1995, **246**: 325-330.

27. Berner RA, *Geochimica Et Cosmochimica Acta*, 1975, **39**: 489-&.

28. Morse JW, Arvidson RS, Luttge A, *Chem. Rev.*, 2007, **107**: 342-381.

29. Zhong SJ, Mucci A, *Geochimica Et Cosmochimica Acta*, 1993, **57**: 1409-1417.

30. Tesoriero AJ, Pankow JF, *Geochim. Cosmochim. Acta*, 1996, **60**: 1053-1063.

31. Tang YZ, Elzinga EJ, Lee YJ, Reeder RJ, *Geochim. Cosmochim. Acta*, 2007, **71**: 1480-1493.

32. Mason HE, Frisia S, Tang Y, Reeder RJ, Phillips BL, *Earth. Planet. Sci. Lett.*, 2007, **254**: 313-322.

33. Hall PO, Aller RC, *Limnology and Oceanography*, 1992, **37**: 1113-1119.

34. Parkhurst DL, Appelo CAJ. *User's guide to PHREEQC (Version 2) - A computer program for speciation, batch-reaction, one-dimensional transport, and inverse geochemical calculations.* U. S. Geol. Surv. Water Res. Inv. Rept., 1999, 99-4259.

35. Eichele K, Wasylishen RE. *HBA*, Version: 1.5. Dalhousie University and Universität Tübingen, 2006.

36. Dalnegro A, Ungarett.L, *Am. Mineral.*, 1971, **56**: 768-&.

37. Devillie.Jp, *Am. Mineral.*, 1971, **56**: 758-&.

38. Dickens B, Bowen JS, *J. Res. Natl. Bureau Stand. Sect. A, Phys. Chem.*, 1971, **A 75**: 27-&.

39. Phillips BL, Lee YJ, Reeder RJ, *Environ. Sci. Technol.*, 2005, **39**: 4533-4539.

40. Michel FM, MacDonald J, Feng J, Phillips BL, Ehm L, Tarabrella C, Parise JB, Reeder RJ, *Chemistry of Materials*, 2008, **20**: 4720-4728.

41. Nebel H, Neumann M, Mayer C, Epple M, *Inorganic Chemistry*, 2008, **47**: 7874-7879.

42. Feng J, Lee YJ, Reeder RJ, Phillips BL, *American Mineralogist*, 2006, **91**: 957-960.

43. Gu ZT, Mcdermott A, *J. Am. Chem. Soc.*, 1993, **115**: 4282-4285.

44. Gu ZT, Zambrano R, Mcdermott A, *J. Am. Chem. Soc.*, 1994, **116**: 6368-6372.

45. Feng J, Lee YJ, Kubicki JD, Reeder RJ, Phillips BL, *Magnetic Resonance in Chemistry*, 2008, **46**: 408-417.

46. Yesinowski JP, Eckert H, Rossman GR, *J. Am. Chem. Soc.*, 1988, **110**: 1367-1375.

47. Stejskal EO, Memory JD. *High resolution NMR in the solid state : fundamentals of CP/MAS*. Oxford University Press: New York, 1994.

48. Nassif N, Gehrke N, Pinna N, Shirshova N, Tauer K, Antonietti M, Cölfen H, *Angew. Chem. Int. Ed.*, 2005, **44**: 6004-6009.

Chapter 6

1. Gertman R, Shir IB, Kababya S, Schmidt A, *J. Am. Chem. Soc.*, 2008, **130**: 13425-13432.